STABILITY ANALYSIS OF MOBILE BOOM CRANES

A Thesis
Presented to
The Academic Faculty

by

Andreas Rauch

In Partial Fulfillment
of the Requirements for the Degree
Master of Science in Mechanical Engineering in the
George W. Woodruff School of Mechanical Engineering

Georgia Institute of Technology
December 2008

STABILITY ANALYSIS OF MOBILE BOOM CRANES

Approved by:

Professor William Singhose, Advisor
George W. Woodruff School of Mechanical Engineering
Georgia Institute of Technology

Professor Wayne J. Book
George W. Woodruff School of Mechanical Engineering
Georgia Institute of Technology

Professor Nader Sadegh
George W. Woodruff School of Mechanical Engineering
Georgia Institute of Technology

Date Approved: July 31, 2008

To my family,

who always supported me

in my endeavors.

ACKNOWLEDGEMENTS

At first, I want to thank my lab mates for their continuous support and their patience.

My special thanks go to Taft Jones for his help in building up the experimental setup and conducting the experiments.

I also want to thank Prof. Book and Prof. Sadegh for being on my committee and for all the knowledge and insights I could gain in their classes.

Last but not least, I have to say thank you to my advisor Prof. Singhose. This work would not have been possible without him pushing me into the right directions, his steady academic advice and his never-ending optimism.

TABLE OF CONTENTS

LIST OF TABLES

LIST OF FIGURES

SUMMARY

Mobile boom cranes are used throughout the world to perform important and dangerous manipulation tasks. Given their mobility, these types of cranes can quickly be moved into position. In most cases, their base is then fixed and stabilized before they start lifting heavy materials. The usefulness of these cranes can be greatly improved if they can utilize their mobile base during the lifting and transferring phases of operation. This ability greatly expands the workspace by combining base motion with the rotation, lifting, and luffing motions. Of course, mobile cranes lose some stability margin when a payload is attached. The stability is further degraded when the payload swings. This thesis presents a stability study of mobile cranes with swinging payloads.

As a first step, a static stability analysis of a boom crane is conducted in order to provide basic insights into the effects of the payload weight and crane configuration. Crane stability is characterized by the maximum payload it can carry throughout the workspace. A crane is regarded as stable as long as all wheel contact forces are positive. The influences of the boom attachment point and the boom weight are investigated. In addition, indices that help to compare the stability properties of different crane configurations are introduced.

A semi-dynamic method is then developed to account for payload swing. The approach estimates the maximum possible payload for straight-line motions of a mobile boom crane. The permissible payload is shown to be a function of the maximum acceleration and velocity.

As a next step, the results of a dynamic stability analysis obtained using a multi-body simulation of the boom crane are compared to the outcomes of the previous approaches. The simulation results are experimentally verified and also used to draw conclusions about arc maneuvers of a mobile boom crane.

Finally, a command generation technique called input shaping is used to create acceleration commands that reduce the payload deflection, eliminate residual payload swing, and thus increase the maximum possible payload. In this context, the effects of traditional input shapers on boom crane stability are investigated, deflection vector diagrams are introduced as a shaper design tool, and specified-deflection input shapers are developed.

The analysis and corresponding results in this thesis provide useful guidance for the practical application of stability analysis to mobile boom cranes.

CHAPTER I

INTRODUCTION

1.1 Mobile Boom Cranes

Fixed-base cranes are used for heavy lifting all over the world. One major drawback of these cranes is their limited workspace. By allowing cranes to move their base, their workspace, and thus their productivity can be enhanced tremendously. An example of a mobile crane transporting a heavy payload from one place to another is shown in Figure 1.

Figure 1: Example for a Mobile Boom Crane [42]

In general, mobile cranes are designed as boom cranes because of their structural

advantages [2]. Therefore, the analysis in this thesis concentrates on boom cranes. However, the stability analysis methods could easily be extended to other classes of cranes. In addition to the standard motions of luffing, slewing, and hoisting of the payload, mobile boom cranes provide the possibility to move their base. This could be accomplished with a wheel base or a track drive. Figure 2 illustrates these possible motions for an example crane with a wheel base. Figure 3 shows a mobile boom crane with a track drive base, a so-called boom crawler.

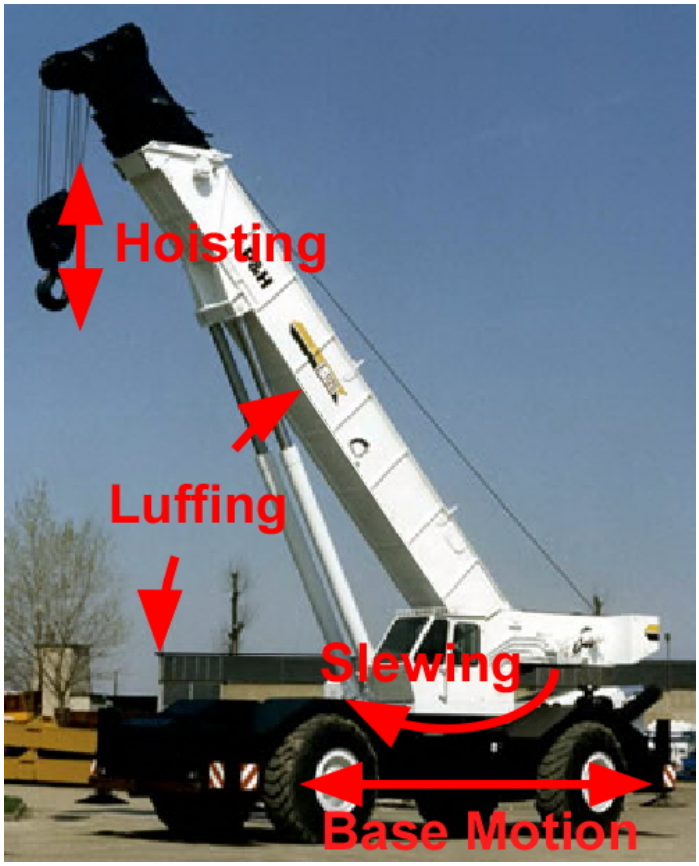

Figure 2: Possible Motions of a Mobile Boom Crane [26]

1.1.1 Stability Issues

Mobile boom cranes carrying heavy loads from one location to another pose a stability hazard, especially during certain driving maneuvers. Accelerations of the mobile base can cause the payload to swing. A centripetal force caused by the oscillation of the

Figure 3: Example for a Mobile Boom Crawler [25]

payload is added to the gravity force. Furthermore, the moment arm of the payload increases as it swings out from the base. The time-varying sum of these forces creates a de-stabilizing torque that endanger the crane by decreasing its stability. Inertia forces on the crane base and its overhanging boom caused by accelerations or decelerations of the mobile base can contribute to this decrease in stability. In the worst case, the crane will tip over, which can cause the total destruction of the crane, enormous damage to the surrounding environment, and even cost lives of humans operating the crane or working nearby. Numerous recent crane accidents have received widespread media attention that has illuminated the dangerous nature of crane operations. Figure 4 shows a mobile boom crawler after a tip-over accident.

Figure 4: Tip-Over Accident of a Mobile Boom Crane [10]

Besides a complete tip-over, there are less harmful forms of mobile crane instability. As a precursor to a complete tip-over, the base of a mobile crane can temporarily lose contact with the ground. During such bucking motions, some of the wheels or tracks of the crane are lifted off the ground. However, because the torques are not

strong enough to tip the crane completely over, the base comes back to the ground and the crane recovers its stable state. Figure 5 shows an overlaid image sequence of a simulated bucking motion. The crane base rises up to a certain pitch angle, but then returns back to the stable position again.

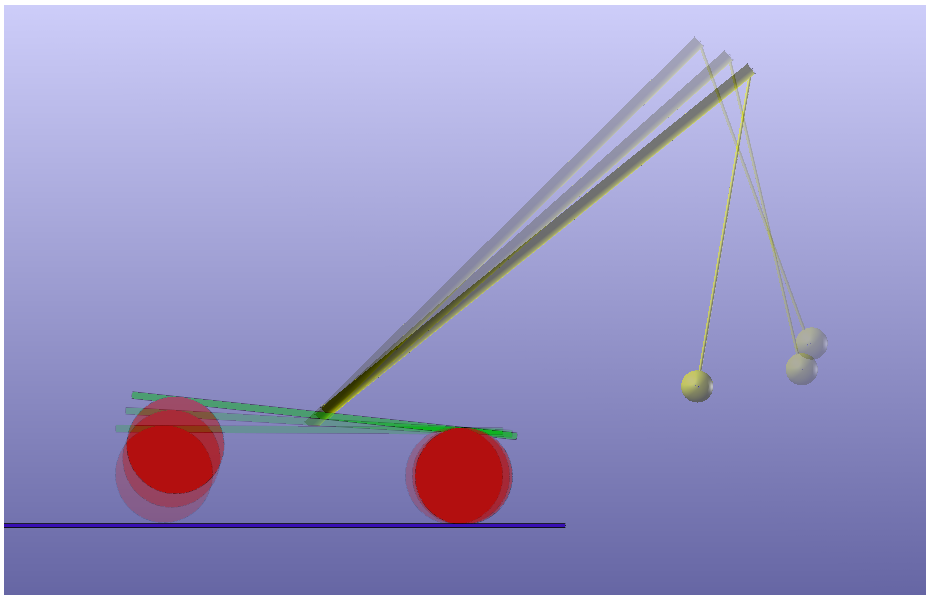

Figure 5: Bucking Motion of a Mobile Boom Crane

When a crane is bucking, it has significantly reduced resistance to rotation about the vertical axis. Therefore, disturbance forces, such as those from a swinging payload, can more easily rotate the crane base when its wheels or tracks are lifted off the ground. This means that a small bucking motion can lead to an uncontrolled change in the crane configuration and a significant loss in stability margin. For this reason, attention is focused on the bucking motion that occurs before the complete tip-over. More precisely, a crane is considered unstable when two or more wheels lift off from the ground at the same time.

1.1.2 Related Fields and Past Research

Similar stability problems as the ones described in the last section occur with aerial platforms, cherry pickers, and lifting trucks. Previous investigations in this area suggest algorithms to limit the lifting truck's maximum speed [8]. The longitudinal speed at which roll-over begins was determined as a function of the cornering maneuver and loading situations. An anti-roll control was then developed to limit the speed command entered by the driver in order to avoid roll-overs. In [20], the tip-over stability of an hydraulic excavator that is used to lift payloads is analyzed.

Another field where roll-over prevention is important is the development of All Terrain Vehicles (ATVs). Complex dynamic models including tire stiffness models and wheel slip, as well as lateral load transfer have been developed in order to predict potential roll-over situations [9]. Similar problems occur also with Sport Utility Vehicles (SUVs) [18].

In [4], a roll-over prevention system for heavy trucks is introduced. A sliding mode controller is used to stabilize the truck in the presence of slosh dynamics of a liquid cargo. Malcher, Eskandarian and Delaigue present more general dynamic models for roll motions that can be applied to a variety of vehicle types [24].

There have also been investigations of the tip-over stability of cranes. However, most previous work in this area has been limited to investigations of the crane's stability in a fixed location during its operation. Kiliçaslan, Balkan and Ider determined the maximum possible payload for a mobile crane that is kept in a fixed position by stabilizing arms while moving the payload [14]. Towarek investigated the dynamic stability of a boom crane on a flexible soil foundation [41]. Kogan studied the stability of cranes under different loading conditions, including wind loads [16]. In [3], a complex dynamic simulation of a hydraulic crane with a fixed base is developed in order to analyze its tip-over responses in the presence of load lifting, load swivel, ground failure and other conditions.

Payload oscillations have a significant influence on the stability of cranes. In [1], payload swing caused by base excitation was investigated and a technique to limit the oscillations by using the reeling and unreeling of the hoisting cable was presented. In [5], the anti-sway problem was formulated as a nonlinear constrained optimal control problem, whereas Lewis, Parker, Driessen and Robinett presented a method to reduce payload oscillation with adaptive command filters [19].

In this thesis, the stability of mobile cranes which are using their mobile base to transport heavy loads from one place to another is investigated in detail. As already mentioned above, mobile cranes are generally designed as boom cranes because of their structural advantages [2]. However, the approaches and results can also be adapted to other types of cranes.

1.2 Input Shaping

1.2.1 General Approach

Previous research on the control of cranes has primarily focused on elimination of payload swing. Because it is hard to get accurate information about the payload position, conventional feedback control techniques are usually not feasible. Furthermore, they may require a large modeling effort and expensive sensors. This is the reason why command shaping control techniques, like input shaping [32], have recently been dominating this area of research [13, 33, 40]. One goal of this thesis is to investigate the effects of input shaping on mobile boom crane stability during driving maneuvers.

An input shaper is a series of impulses with different amplitudes. The time spacings between the impulses, as well as the impulse amplitudes are determined by the desired shaper properties, as well as the system dynamics. If the original command is convolved with this series of impulses and the shaped command is issued to the system, then the system response will not exhibit any residual vibration. To ensure near-zero residual swing on a real system, the input shaper must be designed correctly

and the system properties must be fairly well-known.

Figure 6 illustrates the input-shaping process for an undamped system. The original baseline command on the left side of Figure 6 is a pulse in acceleration in this case. After the convolution with a Zero-Vibration (ZV) Shaper [39], the new shaped command consists of two smaller pulses, the second one delayed in time.

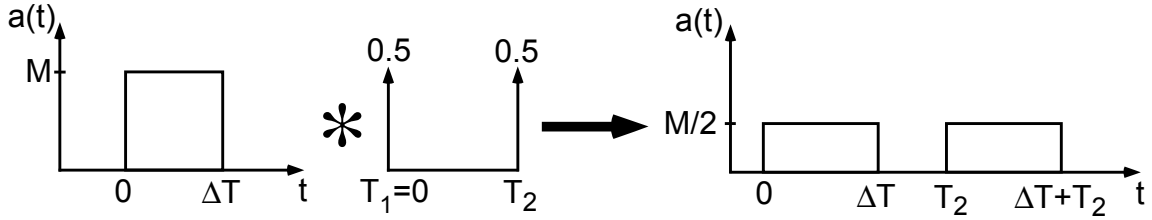

Figure 6: Illustration of the Input-Shaping Process

Figure 7 illustrates the general idea behind input shaping. The blue solid curve shows the vibration caused by the first impulse at $t = 0$. The impulse might be thought of as an impulse in acceleration of the suspension point of an undamped pendulum. The response then represents the motion-induced oscillation of the pendulum. As can be seen in Figure 7, a second impulse at time $t = 0.5$ *periods* causes vibration shown by the dashed line, which is exactly the mirror image of the vibration caused by A_1. If these two commands are issued to the same system, then the oscillations will cancel each other out, as shown by the red curve with circular markers in Figure 7. Thus, the system will not exhibit any residual vibration. The only information needed to design such an input shaper is the natural frequency of the system and its damping ratio. A short overview of past research and applications of input shaping will be given in section 1.2.3.

1.2.2 Vector Diagrams

Although Figure 7 only shows one special case of an impulse sequence that cancels vibration, there are an infinite number of zero-vibration input shapers. A useful tool for the design of input shapers is vector diagrams. On vector diagrams, the impulses

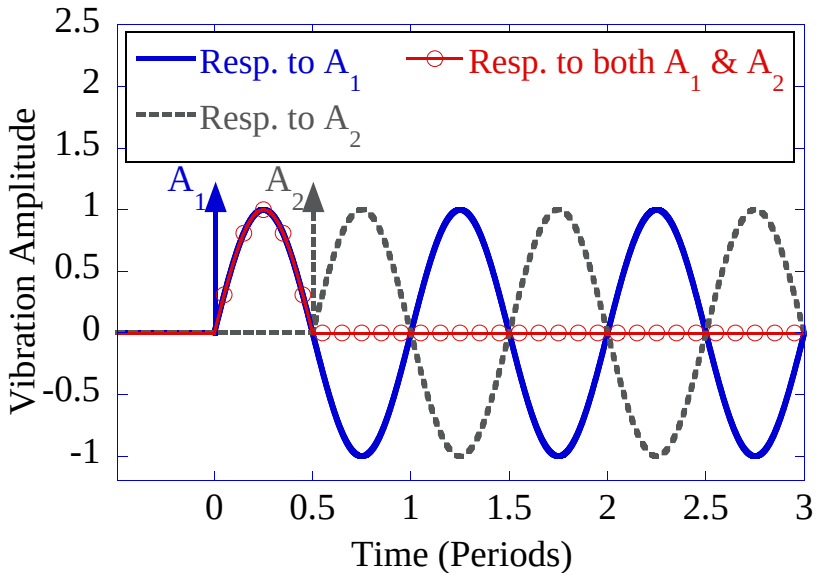

Figure 7: Cancelling Vibration with Two Impulses

of an input shaper are displayed in the phase plane. While the length of the arrows on a vector diagram represents their magnitude, the angle describes the time when an impulse occurs. On a vector diagram, 360° are equal to one oscillation period of the system vibration. Figure 8 shows the vector diagram for the input shaper used in Figure 7.

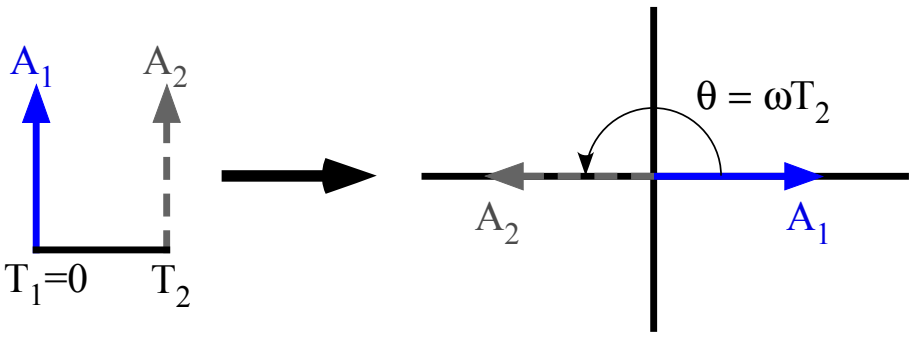

Figure 8: Vector Diagram for a Zero-Vibration Input Shaper

In order to get zero residual vibration after issuing the shaped command to the system, the impulses of the shaper must sum to zero in the phase plane [34]. This is obviously the case in Figure 8, as long as the two impulses have the same magnitude.

To design an input shaper with the vector diagram approach, an arbitrary sequence

of impulses can be drawn in the phase plane. After determining the resultant vector of this sequence, only one impulse that cancels out the resultant vector has to be added in order to get zero residual vibration. After this canceling impulse has been added, the whole impulse sequence has to be rescaled so that the impulse magnitudes sum to one. This last step is necessary for the shaped command to reach the desired setpoint. References [36] and [34] describe the vector diagram approach in more detail.

1.2.3 Past Research

Input shaping has been successfully implemented on a variety of flexible systems.

Several research groups have used input shaping on long reach manipulators [32, 22, 23, 21, 7]. Their goals were to eliminate multiple modes of vibration, improve a tracking control system, or improve PD-control by augmenting it with an input shaper.

Another field of research where the positive effects of input shaping have been investigated is the control of satellites [35, 43, 6, 17, 31]. In this context, input shaping was mainly used to eliminate residual vibration of flexible appendages, and to limit transient deflection during motions of these structures.

An abundant amount of research has been performed to develop input shapers for cranes. Because cranes exhibit almost zero damping in their payload oscillation and this unwanted motion is clearly visible, the detrimental effects of oscillation are quite obvious. Input shaping has been implemented on many types of cranes, like gantry or bridge cranes [12, 13, 40, 33]. There were also experiments with input shaping on a mobile tower crane [44]. However, all these investigation were focused on the elimination of residual vibration. In this thesis, the positive effects of input shaping on mobile crane stability are studied in detail. Past efforts to create specified-deflection input shapers for step inputs in position [27, 31, 28, 29, 30] are extended so that it is possible to develop deflection-limiting shapers in the acceleration domain that

improve stability in a known manner.

1.3 Thesis Contributions

This thesis contributes to the knowledge of boom crane stability in four major areas:

- Development of a mobile boom crane simulation that predicts tip-over motions
- Development of a practical approach to analyze the stability of mobile boom cranes
- Investigation of the influence of input shaping on boom crane stability
- Design of specified-deflection shapers in the acceleration domain

1.4 Thesis Overview

In Chapter 2, a static stability analysis with a simple crane model is performed to gain initial insights into the influences of the crane configuration on the maximum possible payload. Indices that compare the stability of different crane configurations are also presented. Chapter 3 extends the stability analysis to a semi-dynamic model that considers swing angles of the payload. This approach is used to draw conclusions about the crane's behavior during simple driving maneuvers. In Chapter 4, a dynamic multi-body simulation of the crane is developed in order to perform the above-mentioned driving maneuvers and to compare the results with those obtained in the previous approaches. Experiments verify the results of the simulations. In Chapter 5, the deflection-limiting properties of traditional shapers and their impact on mobile boom crane stability are investigated. This builds the basis for the development of specified-deflection input shapers in Chapter 6. A graphical tool for the design of such input shapers, called a deflection vector diagram is introduced in this context. Chapter 7 summarizes the conclusions drawn in this thesis and describes possible future work in the area of mobile boom crane stability.

CHAPTER II

STATIC STABILITY ANALYSIS

To develop a basic understanding of boom crane stability, a static stability analysis is conducted as a first step. A model of a boom crane is shown in Figure 9. The cart has its center of gravity located at distances l_{com} and b_{com} from its the geometric center, and it has a total mass of m_c. The boom is mounted on a rotation platform and has a mass of m_b. Its center of mass is located at a distance l_{bcom} along the boom from its attachment point. The platform has its rotation center at a distance l_a forward of the cart's geometric center. Its rotation is measured by angle β. The boom is attached to the platform at a distance l_{a2} in front of its rotation center and has a length of l_b.

The luffing motion that raises and lowers the tip of the boom is measured by the angle, α. The wheel separation in the longitudinal direction is l_c. The wheel separation in the lateral direction is b_c. The payload, with a point mass of m_p, is attached to the end of the boom by a massless cable of length l. For the subsequent semi-dynamic stability analysis, the model also provides for swing angles of the payload. φ describes the payload swing in the forward direction of the cart and θ is used to describe the lateral oscillation.

This model is used to perform a static stability analysis by calculating the maximum payload that can be attached to the boom so that the crane remains stable, *i.e.* it does not tip over. This analysis was conducted for every possible boom angle configuration. Therefore, the tip-over condition is split into distinct cases: The crane will tip over either to the front (roll-over axis indicated as A-A in Figure 9), to the back (roll-over axis indicated as D-D in Figure 9), or to the side (roll-over axes indicated as B-B and C-C in Figure 9).

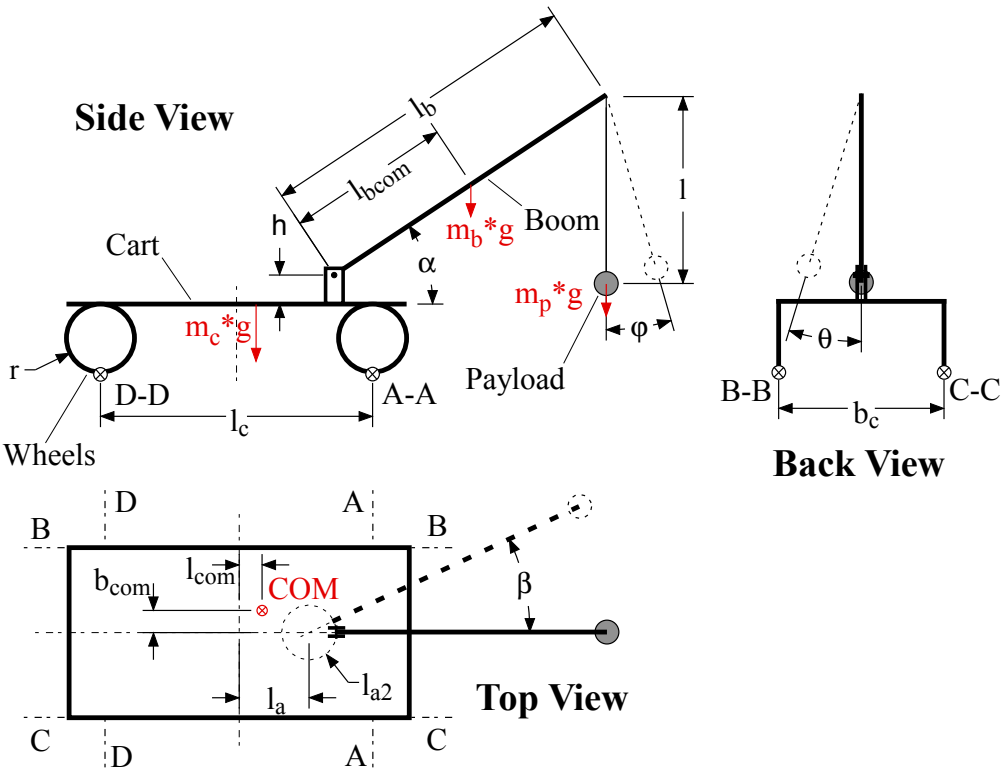

Figure 9: Schematic Diagram of a Mobile Boom Crane

Equilibrium conditions for the torques about the roll-over axes were formulated. These torque equilibriums consist of contributions from the cart and the boom weight, from the payload weight, and from the contact forces exerted on the wheels, which are limited to be compressive forces. If these contact forces vanish, then the crane is starting to tip over. For every boom position, the payload that first causes the wheel contact forces to become zero is computed and stated as the maximum possible payload for the configuration.

Figure 10 shows the maximum payload for the configuration of the crane listed in Table 1 when the luffing angle is 0°, *i.e.* the boom is extended straight out horizontally. In the polar plot of Figure 10, the maximum possible payload is plotted against the slew angle, β. The crane has considerably less lifting capacity when the boom is extended to the front of the crane, instead of to the back. It has even less stability when the boom is pointing to the side. Figure 11 shows similar stability trends when

the boom is luffed up to a 30° angle. The dimensions of the crane are taken from an experimental setup that is used to verify the results. Figure 12 shows a picture of the setup. The solid lines in Figures 10 and 11 show the predicted values, while the diamonds indicate the experimental results. In both graphs, the maximum payload line gives the same shape for the stability boundary, but on a different scale.

Table 1: Test Configuration for the Mobile Boom Crane

m_c	$24.9kg$	l_b	$1.70m$
m_b	$8.0kg$	l_{bcom}	$0.80m$
l_c	$1.10m$	l_{com}	$0.12m$
b_c	$0.70m$	b_{com}	$0.0m$
l_a	$0.30m$	r	$0.14m$
l_{a2}	$0.28m$	h	$0.14m$

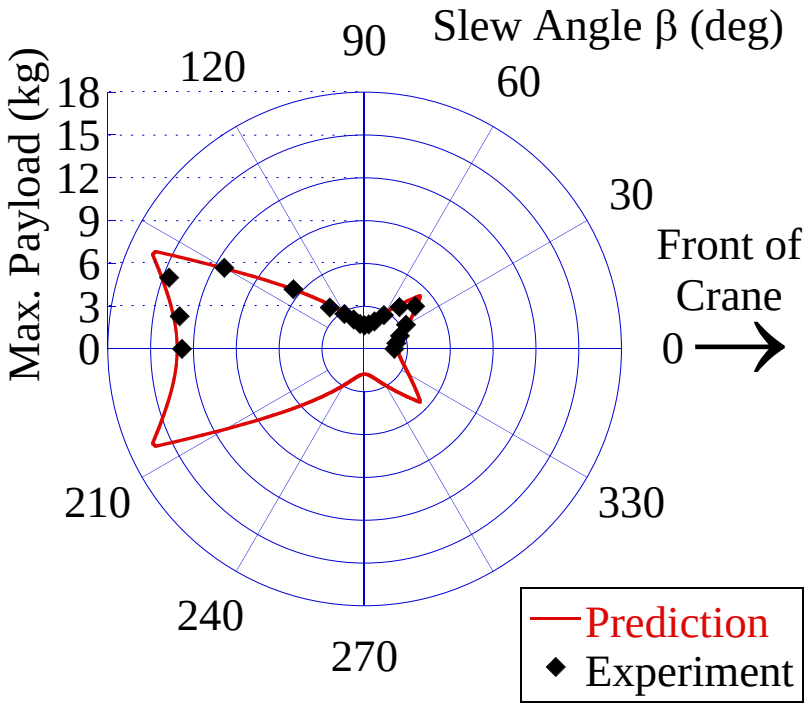

Figure 10: Maximum Payload for a Luff Angle of 0° (Static Case)

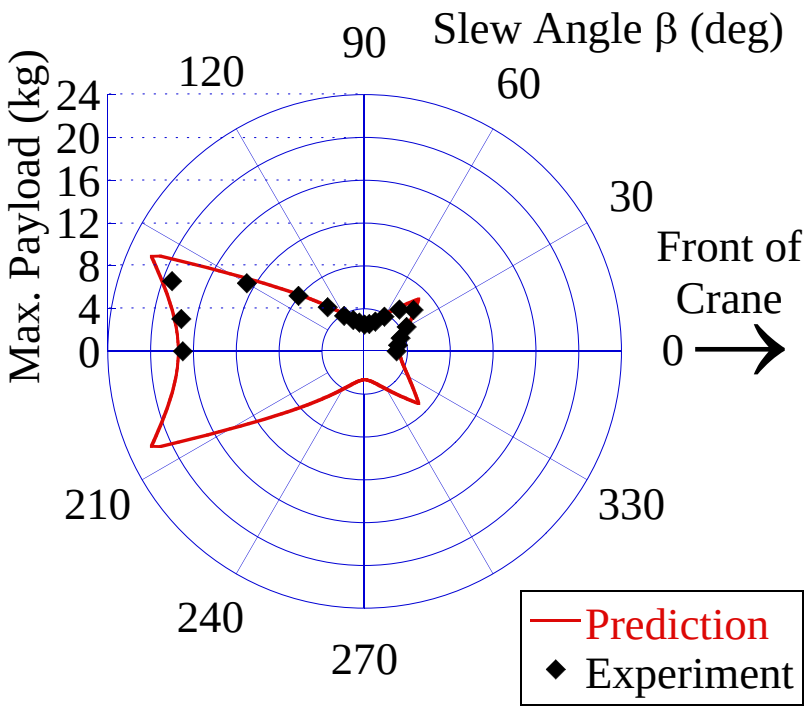

Figure 11: Maximum Payload for a Luff Angle of 30° (Static Case)

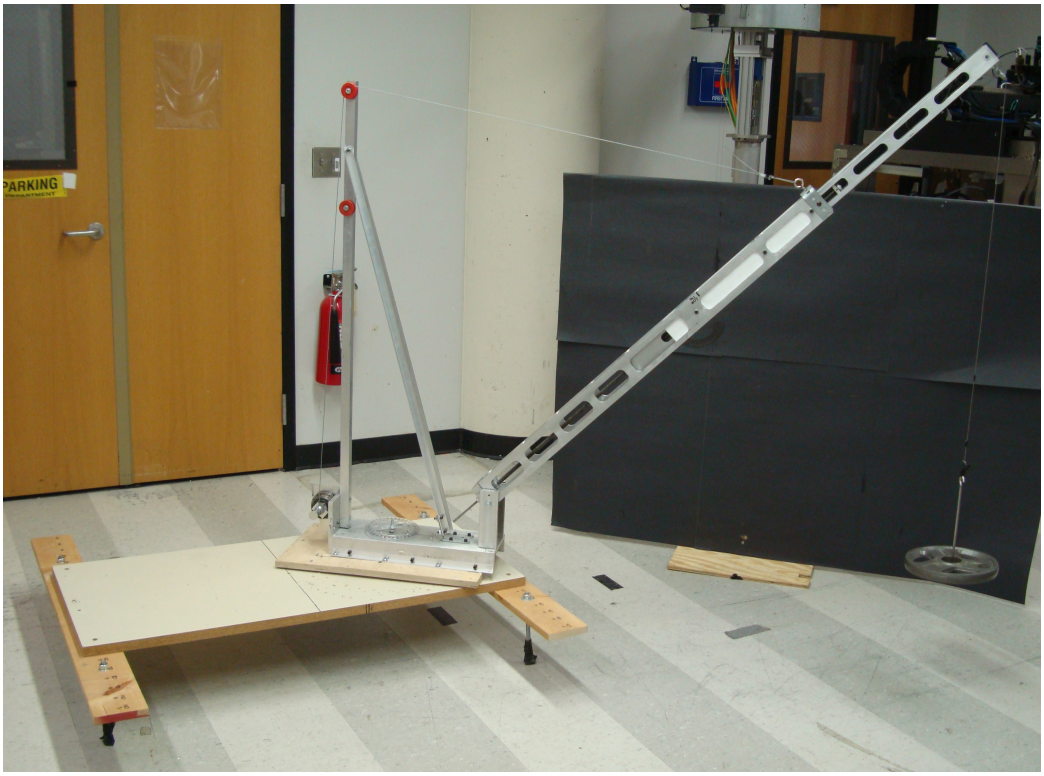

Figure 12: Experimental Setup

In order to get the experimental results, the boom was placed in the desired position and then fixed. For each individual position of the boom, the weight of the attached payload was increased incrementally until the setup started to tip over. The last stable payload value was recorded as the maximum possible payload for the respective boom position. Because of the symmetry of the setup, the experiments were performed only for values of the slew angle β between $0°$ and $180°$.

As can be seen in Figures 10 and 11, the experimental results align well with the prediction. The payload value reaches local minimums at $\beta = 0°$, $90°$, $180°$, and $270°$. The global minimum occurs at $\beta = 90°$ (and $\beta = 270°$) and a luff angle $\alpha = 0°$. This means that the boom points exactly to the side and reaches out as far as possible, which is obviously the most unstable position of the setup in the static case. By limiting the payload to the value at $\beta = 90°$, a stable static behavior can be guaranteed over the whole workspace.

2.1 Influence of the Boom Attachment on Stability

By changing the center of the rotation platform, the static stability behavior of the crane also changes. Figure 13 shows the maximum possible payload for the same crane configuration as before, but for three different values of l_a. Larger values of l_a indicate that the rotation center of the platform is shifted farther forward.

As can be seen in Figure 13, a change in the longitudinal position of the boom does not influence the maximum payload for the lateral stability ($\beta = 90°, 270°$) of the crane. That is the reason why the three curves in Figure 13 representing the maximum payload values for three different boom attachments reach the same value for the boom reaching directly out to the side of the crane. The payload values for the boom sticking out to the front and to the back of the crane are changed significantly. For example, for $l_a = 0.6m$, the setup becomes very stable to the back. A practical drawback of this configuration is that the boom is mounted very far to the front of

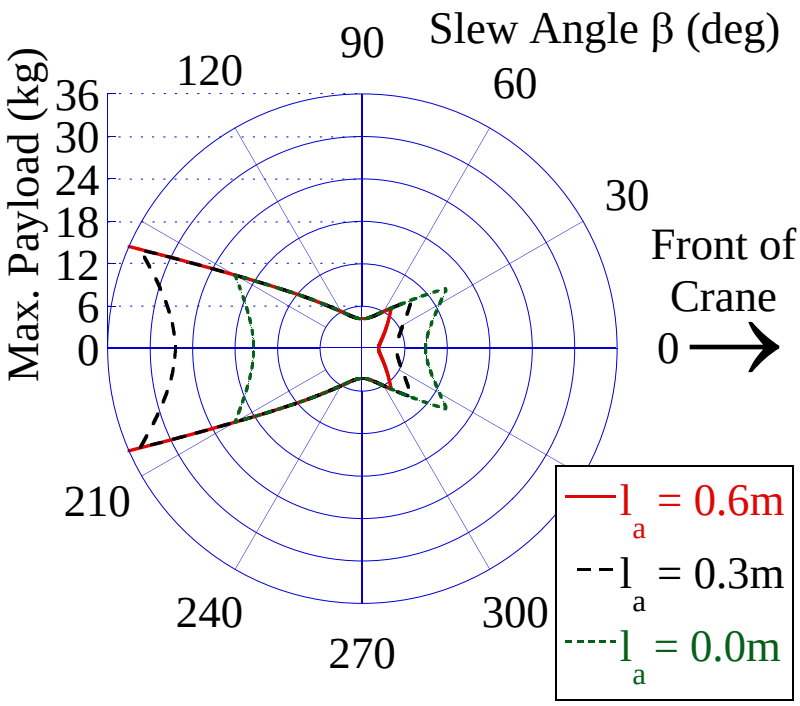

Figure 13: Maximum Payload for Different Boom Attachment Points

the crane and it has less stability to the front. This limits the workspace of the boom to the back because the base of the crane is blocking most of it. However, a payload could be lifted at the front of the crane and could then be brought over the back of the base by a rotation of the boom. Keeping the payload at this very stable position while moving the crane base could help to avoid stability problems during the base motion.

2.2 Influence of the Boom Mass on Stability

Because booms on real cranes are often massive structures, another important parameter to investigate is the mass of the boom. In order to examine its influence, the crane setup listed in Table 1 is used, but with an increased boom mass of $m_b = 12.0kg$. Figure 14 shows the maximum possible payload for this new configuration, as well as for the original configuration listed in Table 1, at a luff angle α of 45°.

The graph reveals that the mass of the boom can have a negligible, as well as a

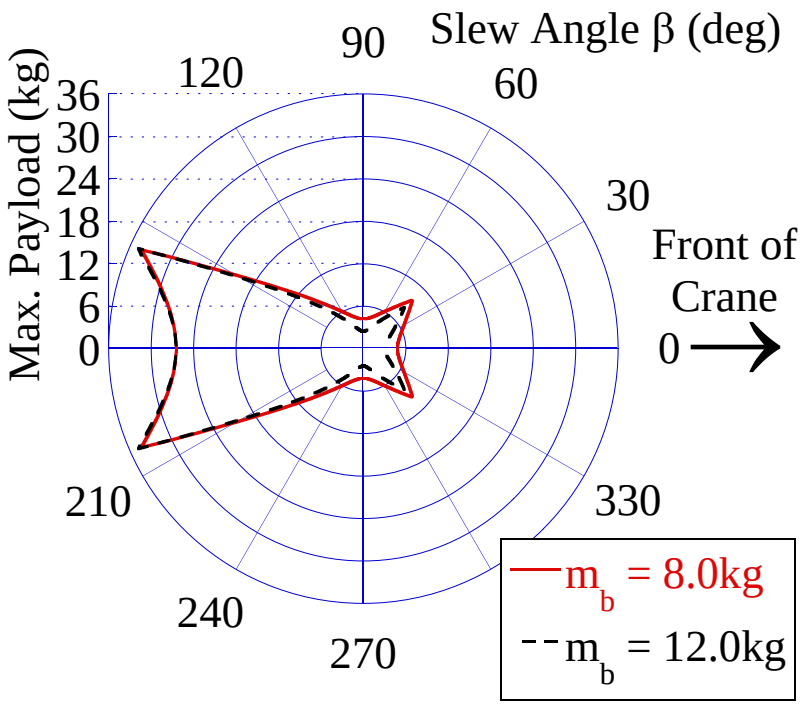

Figure 14: Effect of the Boom Mass on the Maximum Payload

negative, impact on boom crane stability. While the increased boom mass decreases the maximum possible payload over almost the whole range of luff angles, there is an area to the back of the crane where this effect vanishes. This occurs because in this special configuration, the center of mass of the boom is located above the roll-over axis D-D shown in Figure 9. Thus, the boom mass does not have an influence on the torque equilibrium about the roll-over axis. The effect of the boom mass can even be reversed if the position of the boom center of mass is moved towards the boom attachment point. Figure 15 shows the comparison between two different values for the boom mass for a distance between boom attachment and center of mass l_{bcom} of $0.4m$ instead of $0.8m$, again for $\alpha = 45°$. In this case, an increased boom mass has a stabilizing effect for values of β around 180°. In this configuration, the boom center of mass is located above the cart and within the rectangle described by the roll-over axes shown in Figure 9. Thus, the boom mass increases the stabilizing moment about the roll-over axes.

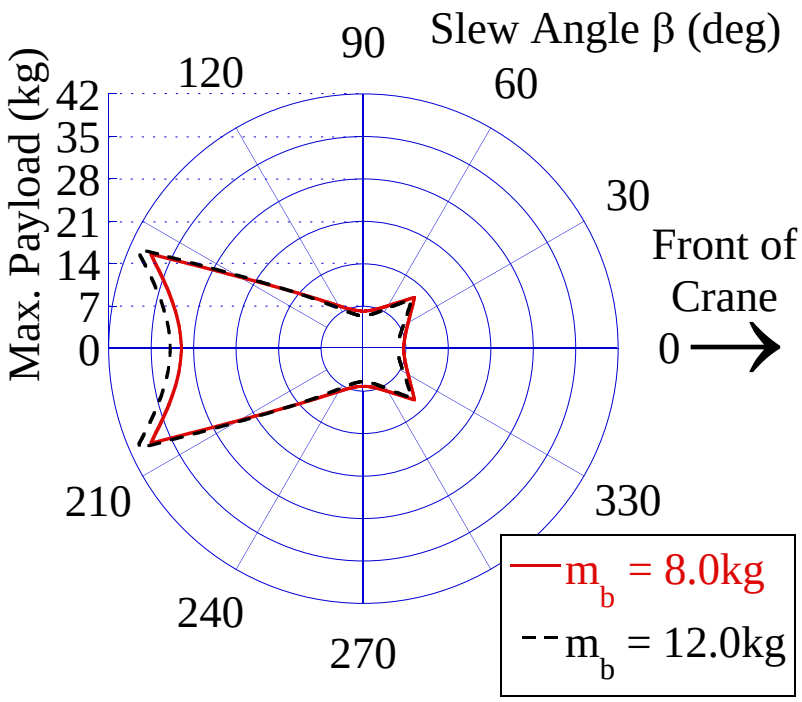

Figure 15: Effect of the Boom Mass on the Maximum Payload for a Changed Boom Center of Mass

The results shown in Figures 14 and 15 suggest that the negative influence of the boom mass on crane stability can be compensated for or even reversed if the boom center of mass is located close enough to its attachment point, *i.e.* it remains within the rectangle described by the roll-over axes. Boom cranes could be designed to exploit this effect.

2.3 Stability Indices for a Comparison of Mobile Boom Crane Configurations

The different crane configurations discussed in the previous sections all have advantages and disadvantages. In order to compare their stability properties, stability indices are introduced. The most obvious indices are the largest overall maximum and the smallest maximum payload for a setup. Because the theoretical maximum payload value would be infinity if the payload was located above the crane base, the classification must be dependent on the values of the luff angle α. For this overview,

the discussion is limited to the general worst case luffing condition when $\alpha = 0°$. Given a fixed luff angle, the average payload over the whole range of slew angles can also be determined. Table 2 shows these three indices for crane configurations with different boom rotation centers.

Table 2: Stability Indices for Example Crane Configurations

l_a	$0.0m$	$0.3m$	$0.6m$
$m_{p,max}$	$11.4kg$	$16.3kg$	$25.0kg$
$m_{p,min}$	$1.8kg$	$1.8kg$	$0.8kg$
$m_{p,ave}$	$5.0kg$	$5.1kg$	$5.7kg$

As can be seen in Table 2, the stability indices change for different positions of the rotation center. The configuration with $l_a = 0.6m$ is very stable when the boom points to the back of the crane and thus it has a very high maximum payload and a large average payload compared to the two other configurations. However, its minimum value for the maximum payload value is considerably lower. The configurations with $l_a = 0.0m$ and $0.3m$ exhibit the same minimum payload value and almost the same average value. However, the configuration with $l_a = 0.3m$ is more stable at slew angles around 180°; therefore, it has a much higher maximum payload.

The conditions under which the crane will be used have to be taken into account to get a full understanding of its stability properties. If the crane is mainly used in places where the payload is easily reachable and the crane can always be put in the desired position, then a high maximum payload might be desirable. In this case, the crane can always be placed so that the payload is picked up and kept at the most stable boom configuration. However, the operator might bring the boom into a less stable position after hoisting the payload at the most stable configuration. This can cause the crane to tip over. To avoid such risks, a well balanced stability behavior of the crane is recommended. Therefore, the minimum and maximum payload values should not deviate too much from the average payload value for any given angle.

2.4 Summary

At the beginning of this chapter, the maximum payload values for an example boom crane setup over the whole range of slew angles and at discrete values of the luff angle were calculated by torque equilibriums about the tip-over axes. The crane was regarded as stable when the wheel contact forces in the torque equilibriums were compressive for a given payload. These calculations described the static case and were verified by experiments. As a next step, the influences of the boom attachment point and the boom mass were investigated. The final section of this chapter introduced stability indices like the maximum, minimum and average maximum payload in order to provide means for the comparison of different boom crane configurations and designs.

CHAPTER III

SEMI-DYNAMIC STABILITY ANALYSIS

3.1 Description of the Approach

Because one of the major contributions of this thesis is the development of a practical stability analysis of mobile boom cranes, the next step is to extend the static model of a boom crane from Chapter 2 by including payload swing angles. The swing angles, indicated as φ and θ in Figure 16, are still regarded as static in this analysis, *i.e.* the payload is deflected, but remains statically in the deflected position, as if the cable was rigid and fixed in this position. This maximum deflection is then used to conduct a static stability analysis again, but this time with different payload moment arms, *i.e.* the moment arms of the payload in the torque equilibrium about the roll-over axes are increased by the lengths d_1 and d_2, as shown in Figure 16. Therefore, the maximum possible payload will decrease with an increasing payload deflection.

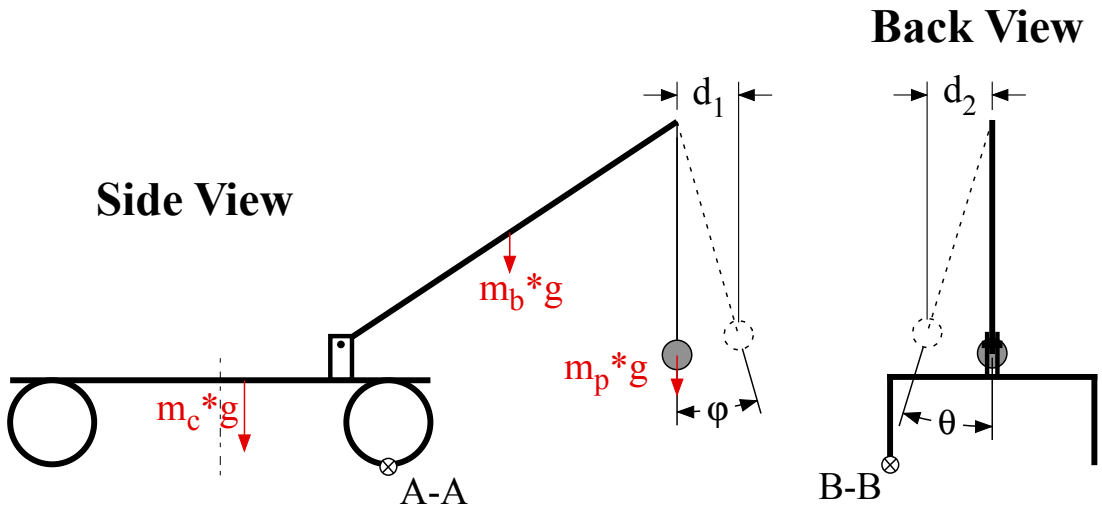

Figure 16: Payload Deflection in Semi-Dynamic Approach

A worst-case position for the payload is assumed for the calculation of the torque

equilibriums. This semi-dynamic approach is used to estimate the influence of payload swing on the stability of a mobile boom crane by simplifying the time-dependent sum of the centripetal and gravity force caused by the swinging payload to a simple static force.

3.2 Comparison to Fully Dynamic Payload Swing

In order to show the usefulness and the limitations of the semi-dynamic approach, a simulation of a payload-cable-boom system will be used to calculate the error between a fully dynamic payload swing including centripetal forces and the simplified estimation.

Figure 17 shows the model of the boom-cable-payload system used for the comparison for payload swing in the boom direction.

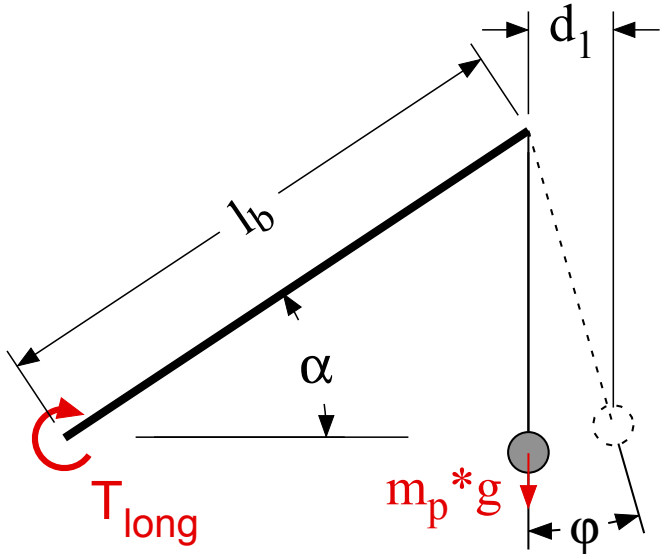

Figure 17: Boom-Cable-Payload System for Longitudinal Payload Swing

The boom has a length of l_b, and the cable length is l. The boom, as well as the cable are regarded as massless for this comparison. For the fully dynamic payload swing, the torque T_{long} about the boom attachment point caused by the mass of the payload and its swinging motion is time dependent:

$$T_{long,dyn} = (m_p g \cos\varphi(t) + m_p l \dot{\varphi}^2(t)) l_b \cos(\alpha - \varphi) \tag{3.1}$$

while the semi-dynamic estimation leads to a constant value for T_{long}:

$$T_{long,semi} = m_p g (l_b \cos\alpha + l \sin\varphi_{max}) \tag{3.2}$$

The relative error is defined as:

$$\frac{T_{long,semi} - T_{long,dyn}}{T_{long,dyn}} \tag{3.3}$$

Figure 18 shows the relative error of the semi-dynamic approach for the case when $l_b = 1.7m$ and $l = 1.0m$. The error is shown as a function of the luff angle α and the maximum swing angle φ_{max}.

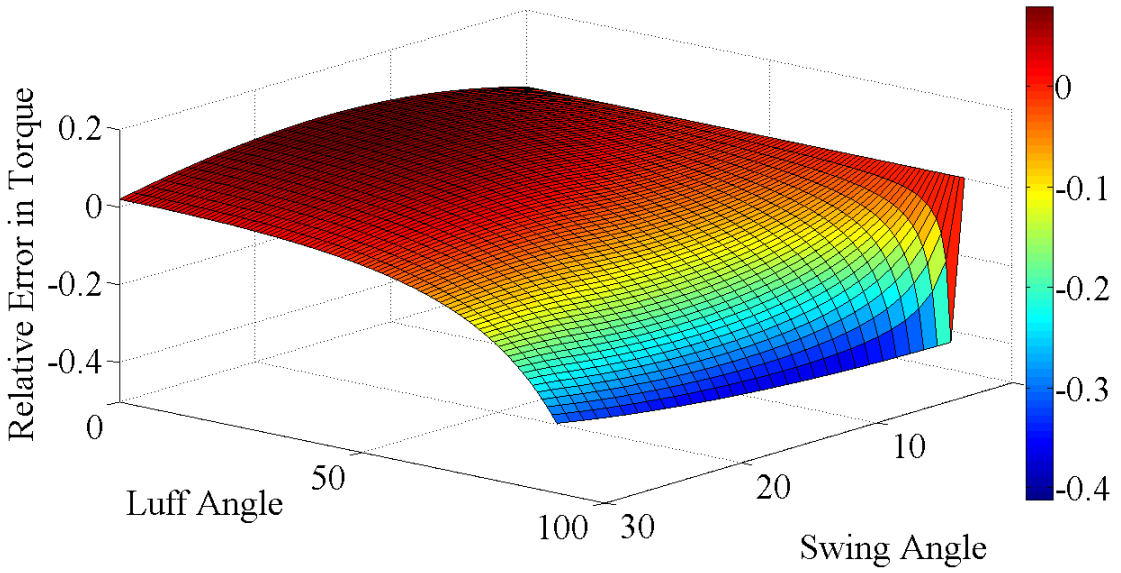

Figure 18: Relative Error of Semi-Dynamic Estimation for Longitudinal Swing

As can be seen in Figure 18, the relative error for small values of the luff angle is positive. This means that the torque T_{long} is overestimated by the semi-dynamic approach. This overestimation makes the semi-dynamic approach more conservative

for stability analysis. For higher values of the luff angle, the torque about the attachment point is underestimated. This means that the estimation predicts permissible payload values that are too large. The maximum swing angle has a much smaller effect in this case.

The comparison between the semi-dynamic estimation and a fully dynamic payload swing was also conducted for payload swing perpendicular to the boom direction. In Figure 19, the boom-cable-payload system and the respective angles and torques for this case are shown. In this case, torques about two axes, $T_{lat,1}$ and $T_{lat,2}$, are compared.

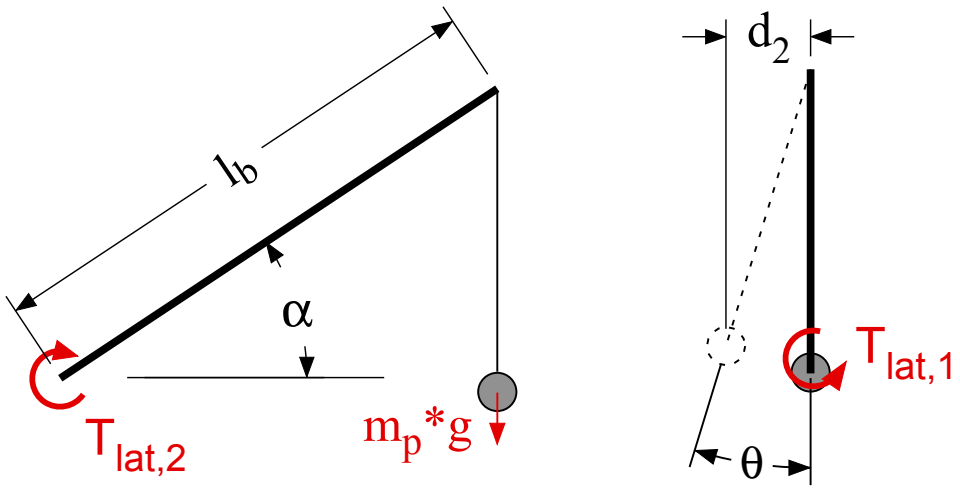

Figure 19: Boom-Cable-Payload System for Lateral Payload Swing

The fully dynamic payload swing leads to the following equations for those torques:

$$T_{lat,1,dyn} = (m_p g \cos\theta(t) + m_p l\dot{\theta}^2(t))l_b \sin\alpha \sin\theta(t) \tag{3.4}$$

$$T_{lat,2,dyn} = (m_p g \cos\theta(t) + m_p l\dot{\theta}^2(t))l_b \cos\alpha \cos\theta(t) \tag{3.5}$$

Instead of these time-dependent equations, the semi-dynamic approach uses the

following two expressions:

$$T_{lat,1,semi} = m_p g l \sin\theta_{max} \tag{3.6}$$

$$T_{lat,2,semi} = m_p g l_b \cos\alpha \tag{3.7}$$

Because m_p can be factored out in all the equations, the relative error between the two approaches does not depend on the payload weight. Figure 20 shows the relative error for $T_{lat,1}$ for the same boom and cable length as above. While the error is close to zero for almost the whole range of luff and swing angles, it approaches infinity for a luff angle of 0°. This is because the torque caused by the fully dynamic payload swing approaches zero in this configuration, which causes the denominator of the relative error to go to zero. However, the semi-dynamic approach predicts a nonzero torque in this case. For low values of the maximum swing angle and hence for small moment arms of the payload, this overestimation is unimportant, but it does make the estimation more conservative.

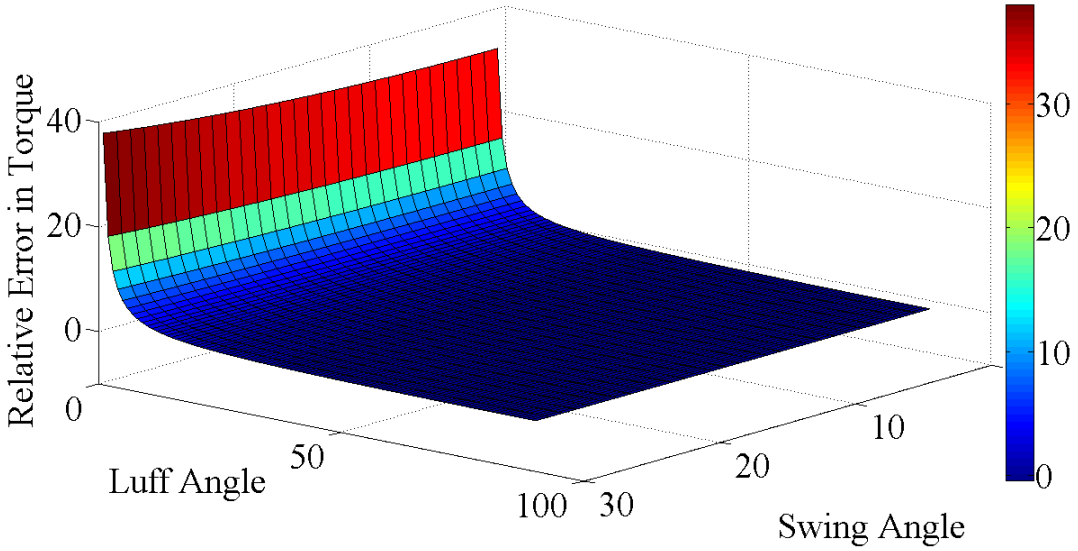

Figure 20: Relative Error of Semi-Dynamic Estimation for Lateral Swing I

Figure 21 displays the relative error for $T_{lat,2}$. This error increases with higher

payload swing angles because the semi-dynamic approach does not take this torque into account at all. It only adds the payload deflection in the lateral direction, but does not compensate for the torque cause by the centripetal force pulling on the boom tip. This deficiency will be compensated for by using a conservative approach of adding the lateral swing angles as a deflection in both the lateral and longitudinal direction of the boom.

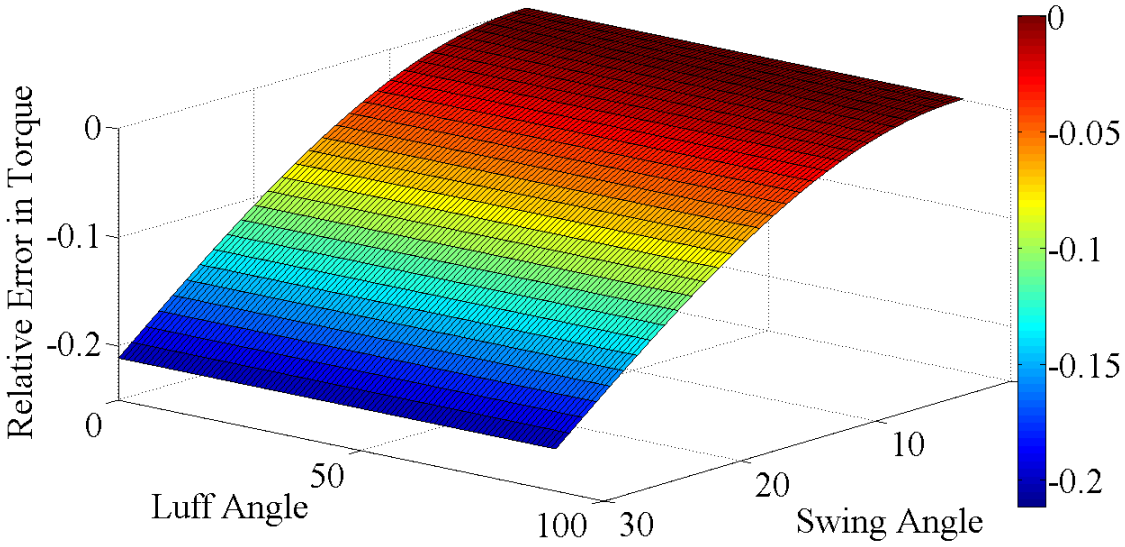

Figure 21: Relative Error of Semi-Dynamic Estimation for Lateral Swing II

The relative errors were also computed for a cable length l of $1.5m$. Figures 22, 23 and 24 show the same plots as above, but for the increased cable length. The only surface that significantly changed is the one for the longitudinal payload swing. In this plot, the torque around the boom attachment point is now overestimated for a larger range of luff angles. This makes the estimation more conservative.

Simulation trials with varying boom and cable length up to dimensions of large boom cranes all showed the same trends. This gives confidence that the semi-dynamic estimation will lead to reasonable results under the restriction of small luff and swing angles.

The difference between the reaction forces at the boom attachment point caused

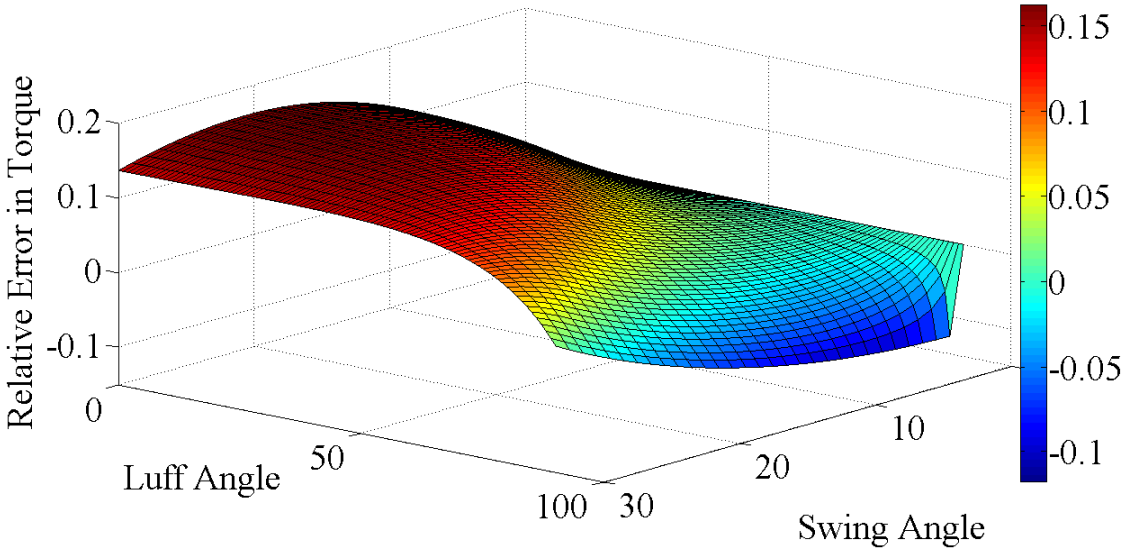

Figure 22: Relative Error of Semi-Dynamic Estimation for Longitudinal Swing for a Suspension Length of $1.5m$

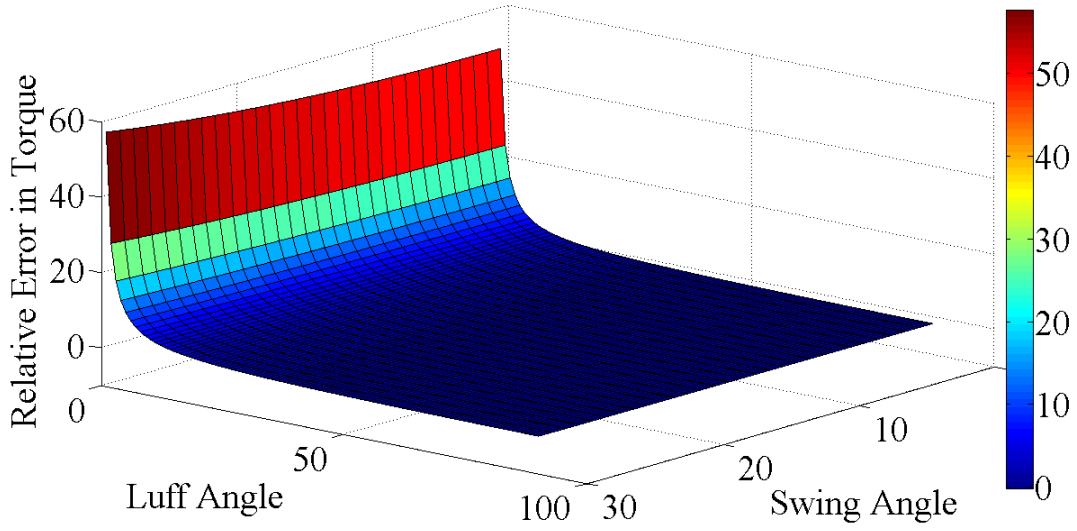

Figure 23: Relative Error of Semi-Dynamic Estimation for Lateral Swing I for a Suspension Length of $1.5m$

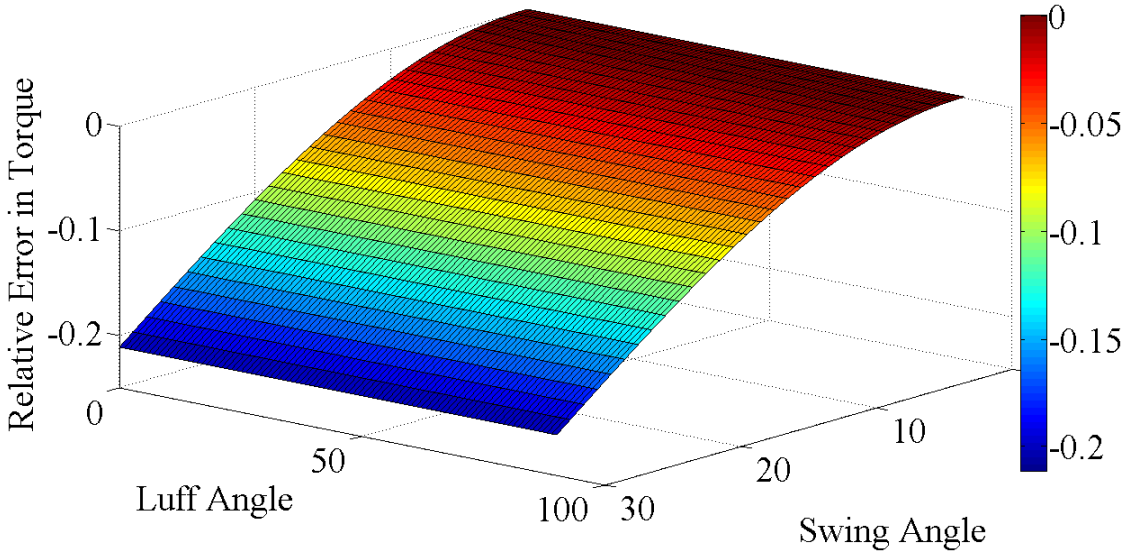

Figure 24: Relative Error of Semi-Dynamic Estimation for Lateral Swing II for a Suspension Length of $1.5m$

by the two different methods are not taken into specific consideration here. Without knowing the boom attachment location for a specific crane setup, their influence on the tip-over torque cannot be calculated. The comparison between the semi-dynamic estimation and a fully dynamic simulation of an example boom crane setup will be conducted in the following chapter. This will provide better insight on the validity of this semi-dynamic approach.

3.3 Swing Angle Calculation

The maximum expected swing angle is needed to estimate the maximum possible payload by the semi-dynamic approach. For the calculation of the maximum swing angle, a closed-form solution depending on the base acceleration command is derived. The equation of motion for an undamped pendulum with an accelerating suspension point is governed by:

$$\ddot{\varphi}(t) + \omega^2 \sin\varphi(t) = -\frac{d^2x(t)/l}{dt^2}\cos\varphi(t) \tag{3.8}$$

where φ is the swing angle, ω is the natural frequency of the pendulum, and x is the position of the suspension point. Using the small angle approximation for φ ($\varphi \ll 1 \Rightarrow \sin\varphi \approx \varphi, \cos\varphi \approx 1$), this equation can be linearized:

$$\ddot{\varphi}(t) + \omega^2\varphi(t) = -\frac{d^2x(t)/l}{dt^2} \tag{3.9}$$

Defining $\frac{d^2x(t)}{dt^2} = a(t)$, (3.9) can be written in the following way:

$$\ddot{\varphi}(t) + \omega^2\varphi(t) = -\frac{a(t)}{l} \tag{3.10}$$

The Laplace transform is:

$$s^2\Phi(s) + \omega^2\Phi(s) = -\frac{A(s)}{l} \tag{3.11}$$

This leads to the following transfer function of the system:

$$G(s) = \frac{\Phi(s)}{A(s)} = -\frac{1}{l(s^2+\omega^2)} \tag{3.12}$$

In this investigation, the acceleration command is limited to bang-coast-bang commands, as shown in Figure 25. This leads to trapezoidal velocity profiles. In the

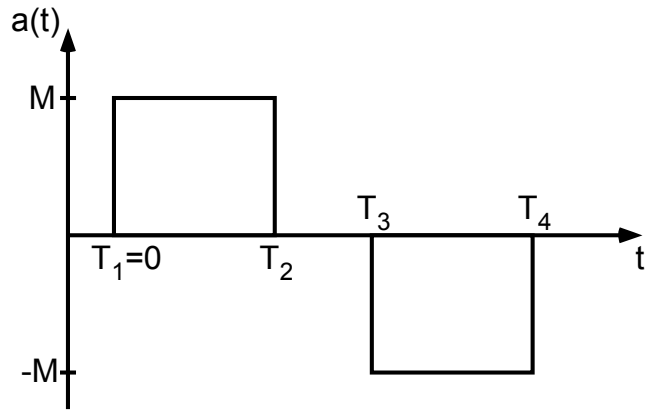

Figure 25: Bang-Coast-Bang Command in Acceleration

Laplace domain, such a command can be described as:

$$A(s) = \frac{M}{s}(1 - e^{-T_2 s} - e^{-T_3 s} + e^{-T_4 s}) \tag{3.13}$$

where M is the magnitude of the acceleration and the $T_i s$ are the respective switch times in the command. Most significant for the investigations of the stability of the crane are the worst cases for the switch times in the command, *i.e.* the switch times that cause the highest amplitude of payload swing. In order to obtain this worst-case swing angle, the resulting expression for $\Phi(s)$ is transformed into the time domain:

$$\begin{aligned}\varphi(t) = -\frac{M}{l\omega^2}\Big(&\Big(1 - \cos\big(\omega t\big)\Big) - \Big(1 - \cos\big(\omega(t - T_2)\big)\Big)\sigma(t - T_2) - \\ &- \Big(1 - \cos\big(\omega(t - T_3)\big)\Big)\sigma(t - T_3) + \\ &+ \Big(1 - \cos\big(\omega(t - T_4)\big)\Big)\sigma(t - T_4)\Big)\end{aligned} \tag{3.14}$$

As can be deduced from (3.14), the largest swing angles occur when the cosine terms are all in phase and the multiplying step functions σ are all 1, which means that $t \geq T_4$. This results in the following expression for the absolute value of the maximum possible swing angle:

$$|\varphi_{max}(t)| = \frac{4M}{g} \tag{3.15}$$

The result from (3.15) can be illustrated by a vector diagram. Therefore, the bang-coast-bang command is described as a step in acceleration of magnitude M convolved with an input shaper. This input shaper consists of four impulses, two positive and two negative ones. The structure of this shaper is shown in Figure 26. The worst case for the switch times of the command is when the impulses of the shaper all line up constructively, as shown in the vector diagram on the right side of Figure 26. The negative impulses are displayed as dotted arrows and pointing towards the origin of

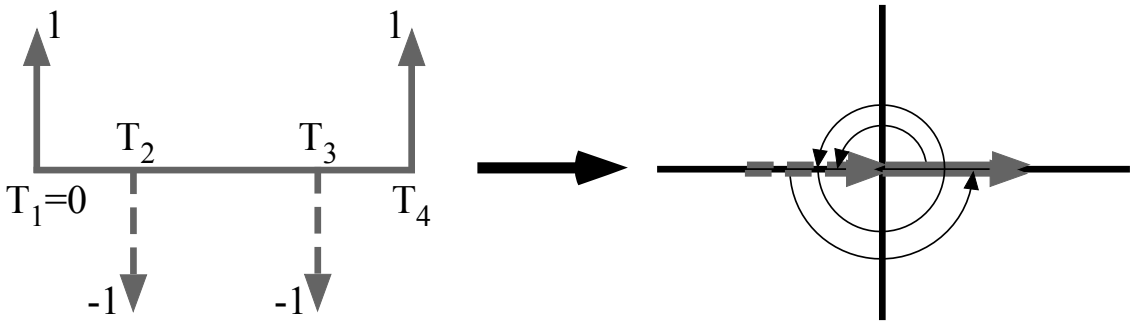

Figure 26: Bang-Coast-Bang Command in Shaper Form

the diagram in this case. Thus, the residual vibration gets four times as large as the residual vibration caused by a single step input.

In order to establish the accuracy of this result, a simulation of a nonlinear pendulum was used to obtain the maximum swing under a variety of conditions. Consider the case when the crane is accelerated at a constant rate of $1.0m/s^2$ up to a maximum speed. The deceleration occurs at the same rate as the acceleration, but is negative in value.

The maximum payload swing angles for this maneuver were computed for move distances between three and ten meters. Because the swing angles φ and θ are measured relative to the cart, the boom position does not matter in this case. By using a payload suspension length l of $1m$, the pendulum has a natural frequency of $\omega = sqrt(\frac{g}{l}) \approx 3.132rad/s$. This means that the first and the second, as well as the third and the fourth cosine term in (3.14) combine constructively if the crane is accelerated at a constant rate of $1.0m/s^2$ to a maximum velocity of $1m/s$ ($T_2\omega = (T_4 - T_3)\omega = 1s \times 3.132rad/s \approx \pi$). Simulating a range of move distances, the worst-case maneuvers with the largest possible swing angles for these acceleration and velocity limits can be obtained.

Figure 27 shows the maximum swing angles for a suspension length of $1m$ for different maximum speeds and an acceleration of $1m/s^2$. The humps in the curve occur when the first and the second pair of cosine terms in (3.14) are in phase.

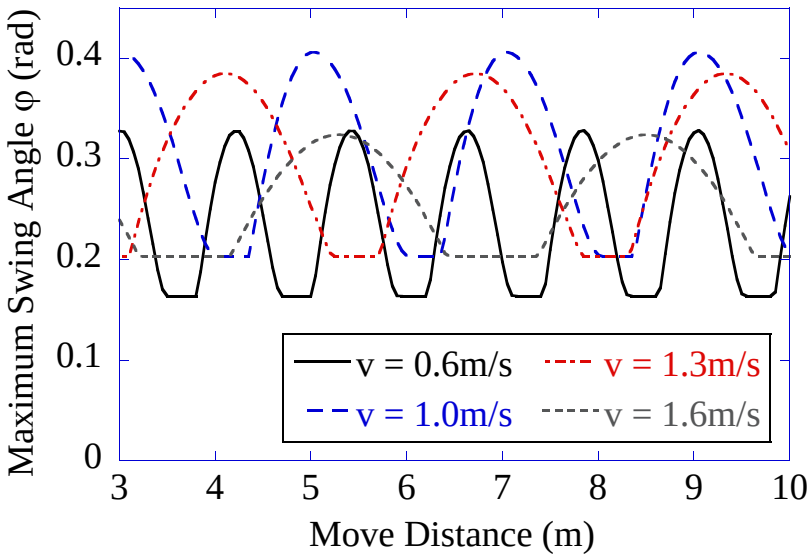

Figure 27: Maximum Swing Angles as a Function of Move Distance

According to (3.15), the maximum swing angle for this maneuver is $0.4077 rad$, which agrees with Figure 27. Figure 27 also shows, as predicted, that this maximum swing angle occurs for an acceleration of $1 m/s^2$ and a maximum speed of $1 m/s$. Because neither the first and the second nor the third and the fourth cosine terms in (3.14) are in phase for the other values of v, the maximum possible swing angles caused by these maneuvers are lower.

Another interesting effect that can be seen in Figure 27 is that the maximum swing angle cannot be reduced below $0.2 rad$ for values of v greater than or equal to one. This limiting value is the amplitude of deflection caused by the initial acceleration. Only by keeping the pulse in acceleration very short, and thus the maximum velocity v very low, is it possible to reduce the maximum deflection below this value, as can also be seen in Figure 27 for $v = 0.6 m/s$. This effect will be used in the design of specified-deflection input shapers in Chapter 6.

A jerk limitation in acceleration, which would lead to trapezoidal acceleration pulses, would make the velocity profile and the crane motion smoother. In general, such a command smoothing leads to smaller maximum swing angles. This is the

reason why the investigations in this thesis are limited to the more aggressive bang-coast-bang commands.

3.4 Stability Results

The overall maximum swing angles were used to add a payload deflection, as described above, to the static stability analysis. In this case, the maximum swing angle was taken, because this is the worst-case scenario for the semi-dynamic estimation. For all values of the deflection angle lower than the maximum swing angle, the payload moment arm is shorter and thus, this configuration is less critical for stability. With this added influence, the maximum possible payload values for all luff and slew angles were computed again. As for the static case, the crane was considered as stable as long as the the wheel contact forces in the torque equilibriums about the roll-over axes where positive. Because the crane was only moved in the forward direction, the values for the lateral sway θ were zero. However, the semi-dynamic approach does not take the centripetal force caused by the longitudinal swing into account, which also has an influence on the torque equilibrium about roll-over axis B-B. This deficiency was already pointed out in Section 3.2. In order to compensate for this fact, and to make the semi-dynamic estimation more conservative, the maximum longitudinal payload sway φ was also added as a lateral payload deflection.

Figure 28 shows the maximum possible payload for the static case and three different values of the luff angle. Figure 29 displays the semi-dynamic predictions for a suspension length of $1m$, an acceleration/deceleration of $1m/s^2$ and a maximum swing angle of $0.4077rad$ (23.36°). These plots show the results for the crane configuration listed in Table 1.

Comparing Figures 28 and 29, it is obvious that the corresponding curves shrink toward the center of the polar plot after adding the payload deflection. Because a payload deflection was added in the lateral, as well as in the longitudinal direction, the

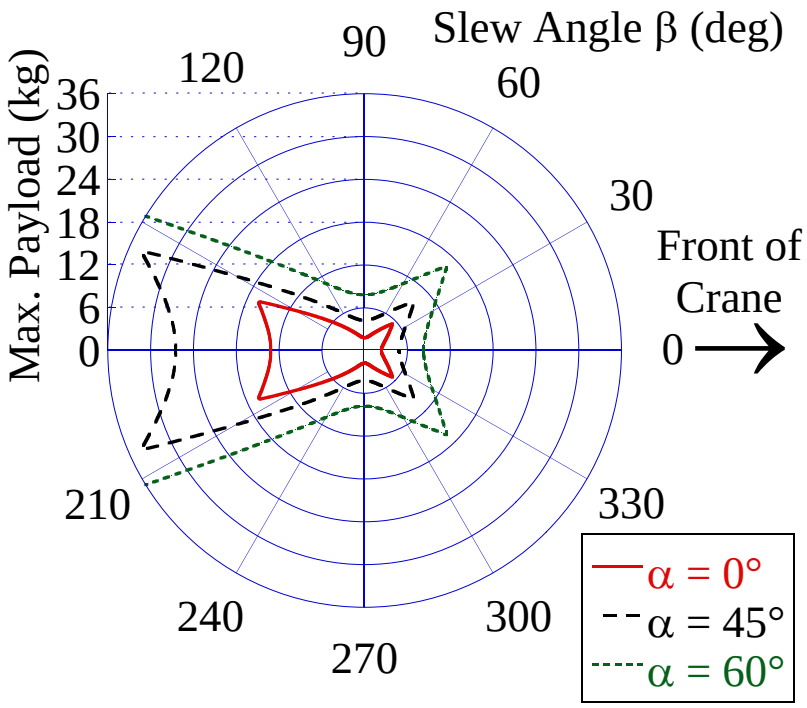

Figure 28: Maximum Payload for the Static Case

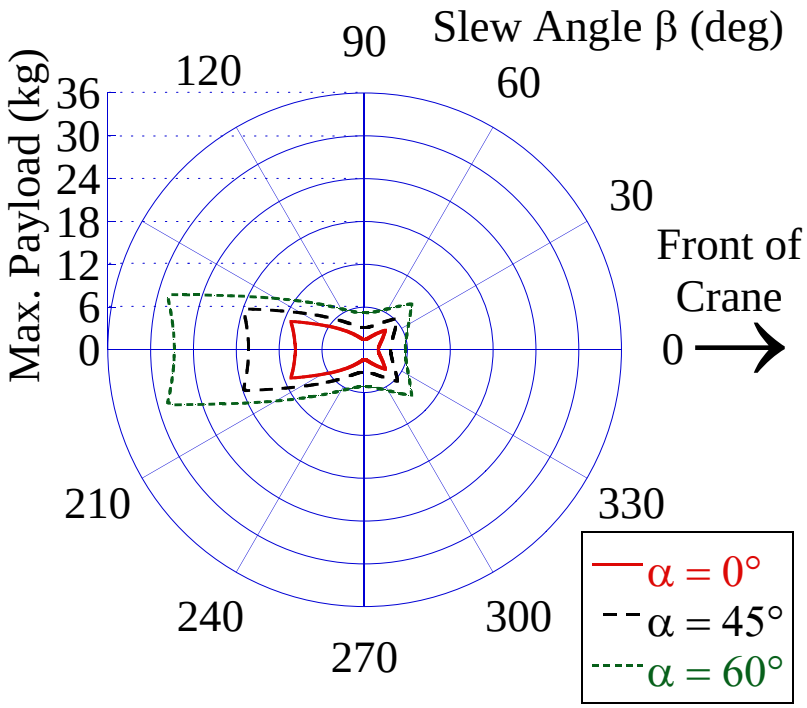

Figure 29: Semi-Dynamic Estimation for the Maximum Payload

maximum payload values decrease for all slew angles. To determine if this estimation provides reasonable approximations of the stability of a mobile boom crane during straight-line driving maneuvers, a dynamic simulation of a crane will be used to assess the outcomes of this semi-dynamic prediction in Chapter 4.

3.5 Effect of Inertia

For high accelerations and decelerations of a mobile boom crane, the inertia forces acting on the cart and boom mass can have a significant effect on the tip-over stability of the crane. This is especially true if the center of mass of the cart is located high above the ground or the crane has a massive boom with its center of mass located very high. These effects have to be taken into consideration to get a reasonable estimation of the maximum possible payload the crane can actually carry.

A simple way to take theses influences into account is to use D'Alembert's Principle to estimate the tip-over torque during the deceleration of the crane. D'Alembert's Principle says that if the dynamic behavior of a mass is analyzed in an accelerated, body-fixed reference frame, then the inertia forces, which are fictitious forces in general, have to be regarded as real forces acting on the mass. In this case, we get the free body diagram shown in Figure 30 for the horizontal forces acting on the cart-boom system during deceleration.

The center of mass of the combined cart-boom system lies somewhere on the connecting line between the individual centers of mass of the cart and the boom. Although the inertia force acting on it and the braking force F_b acting on the wheels cancel each other out in the horizontal direction, they cause a torque that aids in tip-over. This torque can be determined by multiplying the inertia force by the height of the center of mass above the ground, h_{COM}. Because the deceleration is assumed to be of a constant magnitude M, the tip-over torque is also constant. This torque is then added to the torque equilibrium about roll-over axis A-A shown in Figure 9.

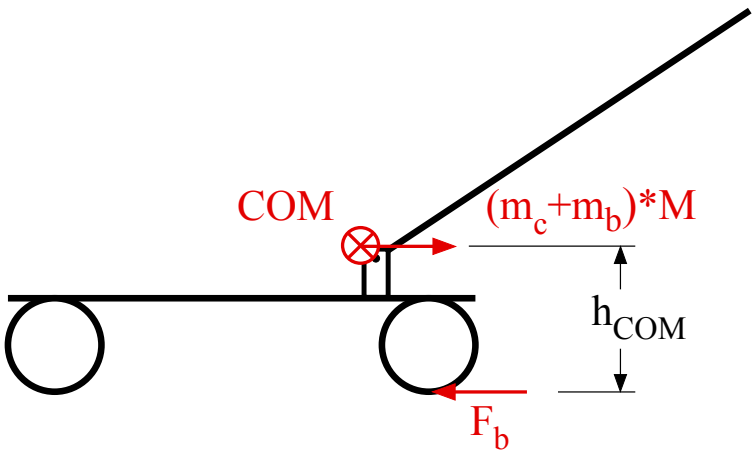

Figure 30: Horizontal Free Body Diagram for the Cart-Boom System

Figure 31 illustrates the effect of the inertia for a luff angle of 30°. The maximum payload is reduced only for slew angles between ±45°. For the rest of the range of slew angles, the crane is either tipping over to the side or to the back.

The influence of the inertia forces during the acceleration of the crane is not taken into account because the payload swing angle is considerably lower during that phase than in the deceleration phase. Therefore, the crane is more likely to tip over to the back after it has come to a stop again because of the large amount of payload swing than to be pulled over during the acceleration.

The accuracy of this inertia force estimation will also be investigated in Chapter 4, with the help of the full dynamic simulation.

3.6 Summary

In this chapter, a semi-dynamic stability analysis was introduced to determine the stability of a mobile boom crane during simple straight-line driving maneuvers. The steps in this analysis are:

- Calculate the maximum possible swing angle for the desired maximum acceleration of the crane using (3.15).

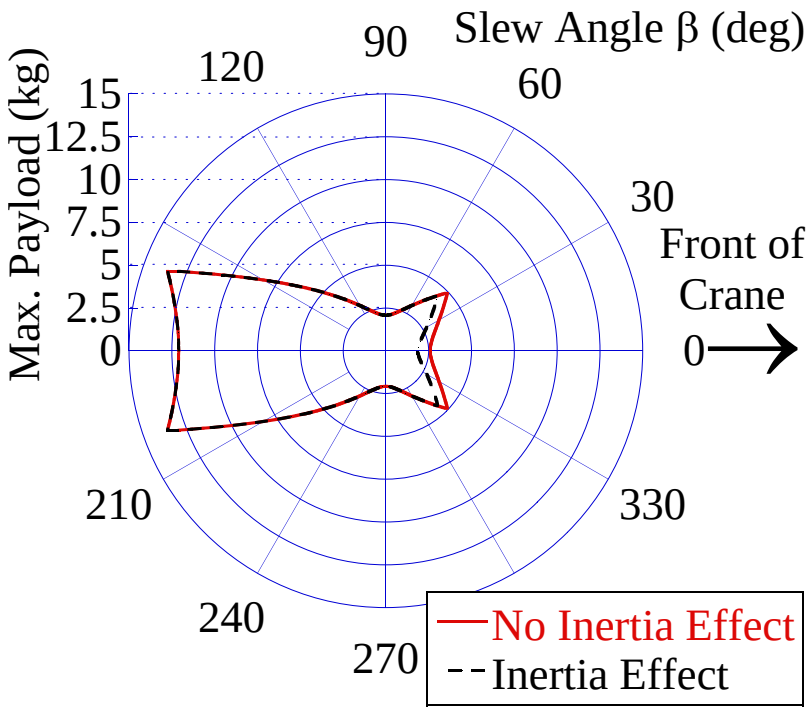

Figure 31: Effect of the Inertia Compensation

- Calculate the tip-over torque caused by the inertia forces acting on the cart and the boom mass during the deceleration of the crane.

- Determine the torque equilibriums about the tip-over axes including the contributions from the cart and the boom mass, from the deflected payload, from the inertia forces, and from the wheel contact forces.

- Compute the maximum possible payload by setting the wheel contact forces in the torque equilibriums to zero and determining the torque equilibrium with the lowest payload value for every boom position.

The limitations of this approach were illustrated through comparisons to a simulated, fully dynamic payload swing of a simple boom model. The accuracy of the semi-dynamic approach will be investigated in the following chapter by comparing its predictions to the results of a full dynamic simulation of a mobile boom crane.

CHAPTER IV

DYNAMIC STABILITY ANALYSIS

The preceding chapters presented stability analysis methods that are fairly easy to conduct. However, the results are subject to the various simplifying assumptions. This chapter presents a detailed stability analysis that is more difficult to implement, but it provides support for the results obtained with the simpler methods.

4.1 Multi-Body Simulation of a Mobile Boom Crane

This section presents a multi-body simulation of the mobile boom crane that can predict tip-over dynamics. Figure 32 shows the top view of a schematic model of this multi-body simulation.

The origin of the coordinate system **A** is located on the ground. The cart's position in the Newtonian coordinate system **N** is defined by a vector $[xy]$ that describes the location of the origin of **A** and a rotation about a vertical axis (angle ψ). The boom rotates relative to the cart (angle β). The coordinate system **D**, shown at the end of the boom, is aligned with **A** for zero swing angles. Thus, it is possible to describe the payload swing angles relative to the cart.

Figure 33 shows a side view of the model. The cart can pitch about its lateral axis, described by angle q_1. It can also move up and down. Therefore, the vector from point AO to point CC (indicated as a dotted line in Figure 33) has a variable length, but is always aligned with the C_3 direction of coordinate system **C**. The cart motion is constrained by wheel-ground contacts, modeled by spring-damper subsystems. To better match the behavior of a real system, these forces are limited to be compressive forces so that the springs do not pull the wheels back to the ground. The payload swing angles are measured relative to the coordinate system **C**. The basic dimensions

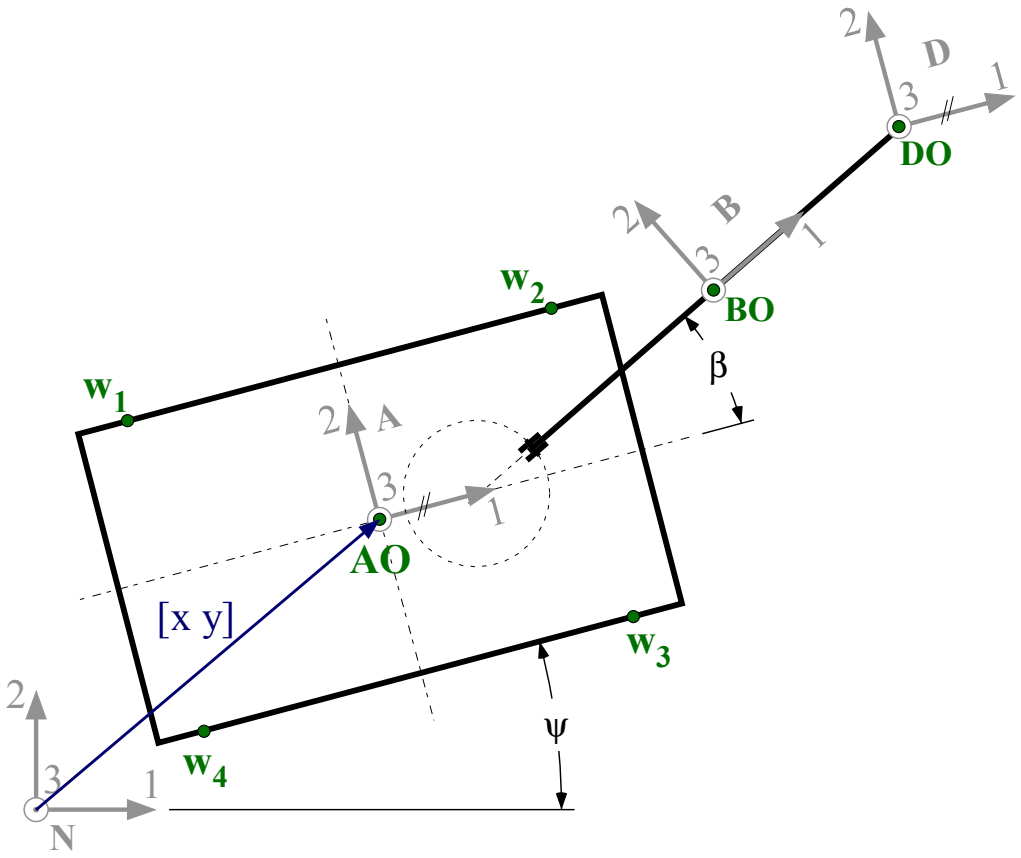

Figure 32: Model of the Multi-Body Simulation (Top View)

and weights of the crane used in the subsequent simulations are taken from the static example setup that was given in Table 1.

Figure 34 shows the model from the back. As can be seen, the cart rolls relative to the **A** frame about the longitudinal axis of the cart, described by angle q_2.

The equations of motion were found with the aid of the software package AUTOLEV. The AUTOLEV source code is found in the appendix. The simulations were run in MATLAB.

4.2 Payload Swing

The multi-body simulation presented in the previous section was used to detect the maximum payload that does not cause a bucking motion when the maximum longitudinal swing angle φ is $0.4077 rad$. This maximum swing angle was determined as the

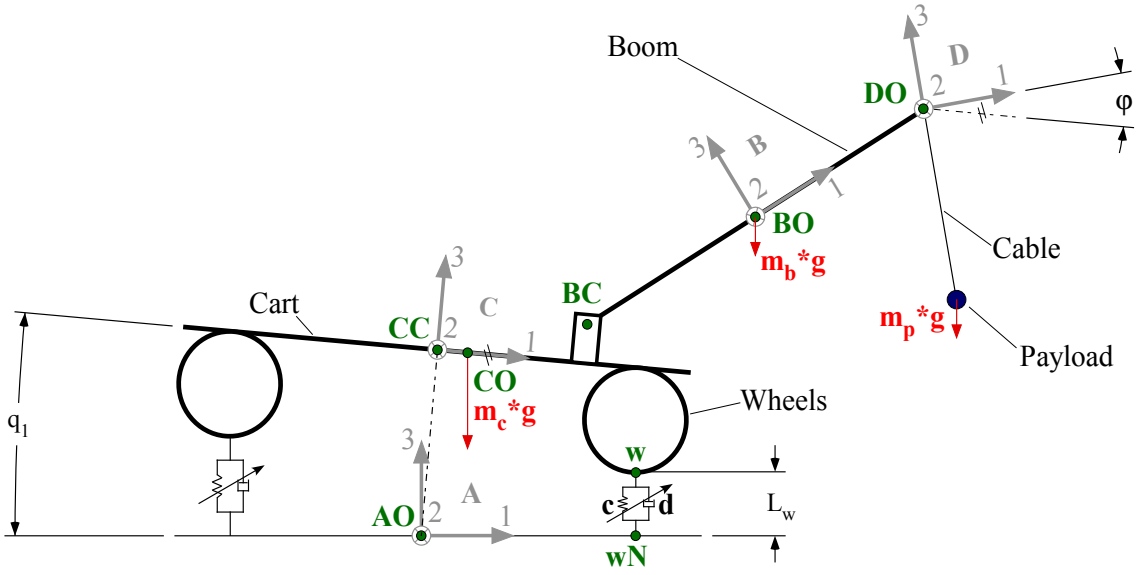

Figure 33: Model of the Multi-Body Simulation (Side View)

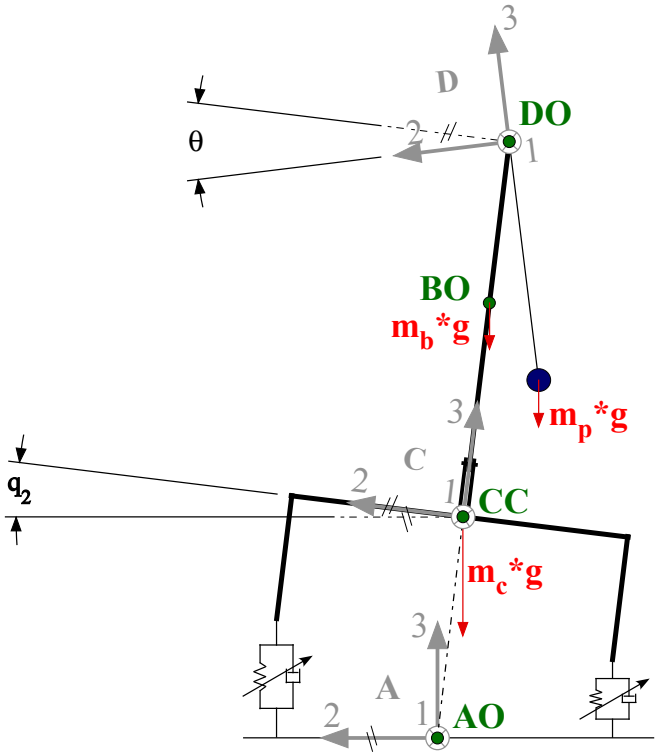

Figure 34: Model of the Multi-Body Simulation (Back View)

worst case caused by a maximum crane acceleration of $1m/s^2$ and a bang-coast-bang command in acceleration. For the simulations, a bucking motion was detected if two wheels of the crane lost their contact with the ground at the same time. This test did not involve any movement of the cart and thus, no influence of the cart or boom inertia caused by acceleration or deceleration occurred.

Figures 35 and 36 show the results of the simulations and the predictions from the semi-dynamic estimation, as well as the experimental outcomes for two different values of the luff angle α.

For the experiments, the setup shown in Figure 12 was used again. This time, the boom was fixed in the desired positions and the payload was deflected to approximately $0.41rad$ ($23°$) in the longitudinal direction. The payload was increased incrementally until the cart exhibited a bucking motion after releasing the payload from this position and letting it swing. The largest payload value that produced a stable behavior of the setup without any bucking was recorded as the maximum possible payload.

As can be seen in Figures 35 and 36, the results from the simulation closely align with those from the experiments. Additionally, the semi-dynamic estimation produces the same general shape obtained by the simulations and experiments. For $\alpha = 30°$ it slightly underestimates the maximum possible payload over the whole range of slew angles β, as desired. For $\alpha = 45°$, the predicted maximum payload is slightly higher than the payload obtained from the simulations and experiments around $\beta = 0°$ and $\beta = 180°$. The comparison of the semi-dynamic estimation with a simulation of a fully dynamic payload swing in Section 3.2 already indicated such a trend for increasing values of α. Because the maximum payload values for lower values of α are lower, they would be used to determine the critical payload for stability. Therefore, this effect does not compromise the significance of this stability analysis. For slew angles around $90°$ and $270°$, the semi-dynamic analysis still underestimates

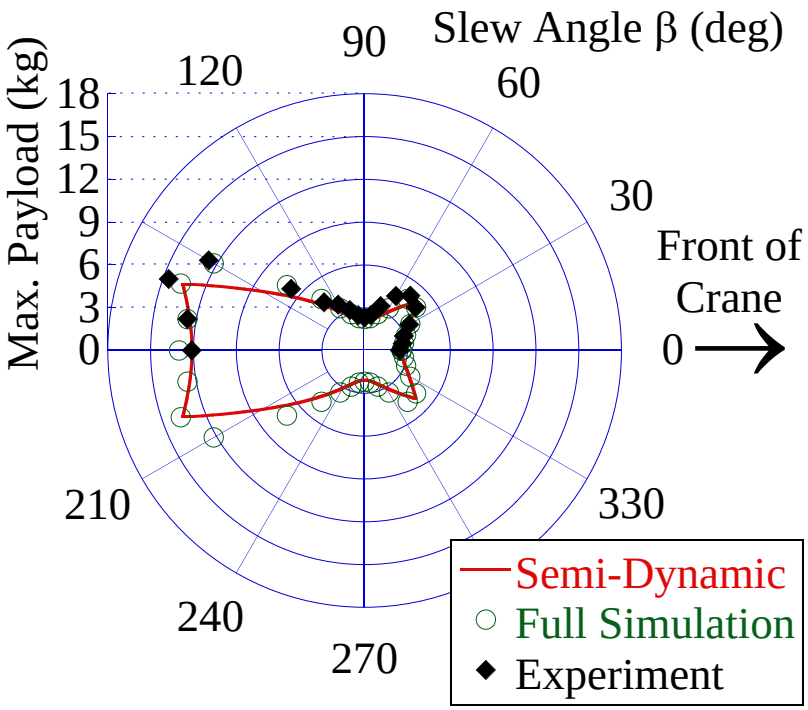

Figure 35: Maximum Payload for a Luff Angle of 30°

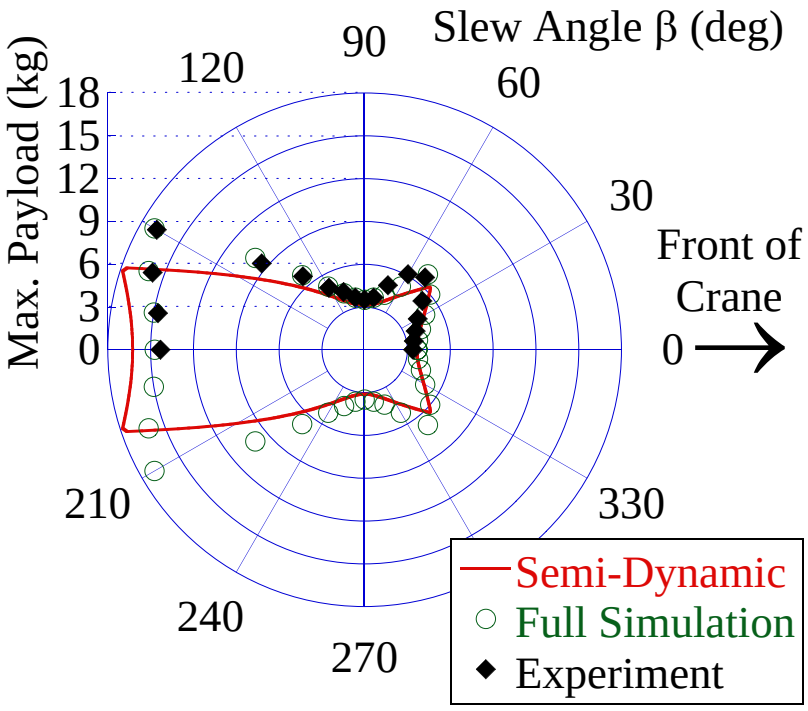

Figure 36: Maximum Payload for a Luff Angle of 45°

the maximum payload because the longitudinal payload deflection was also added, as a lateral deflection, to account for the neglected centripetal force. This makes the estimation fairly conservative for this range of slew angles.

As already indicated in Section 3.2, the payload suspension length has an influence on the semi-dynamic estimation. A longer suspension length, as seen in Section 3.2, makes the estimation more conservative and also more reliable for higher values of the luff angle α. For this reason, the simulations and experiments were also conducted for a luff angle of 45° and the longest possible suspension length, which was $1.45m$ for the experimental setup. Figure 37 presents the results of these tests.

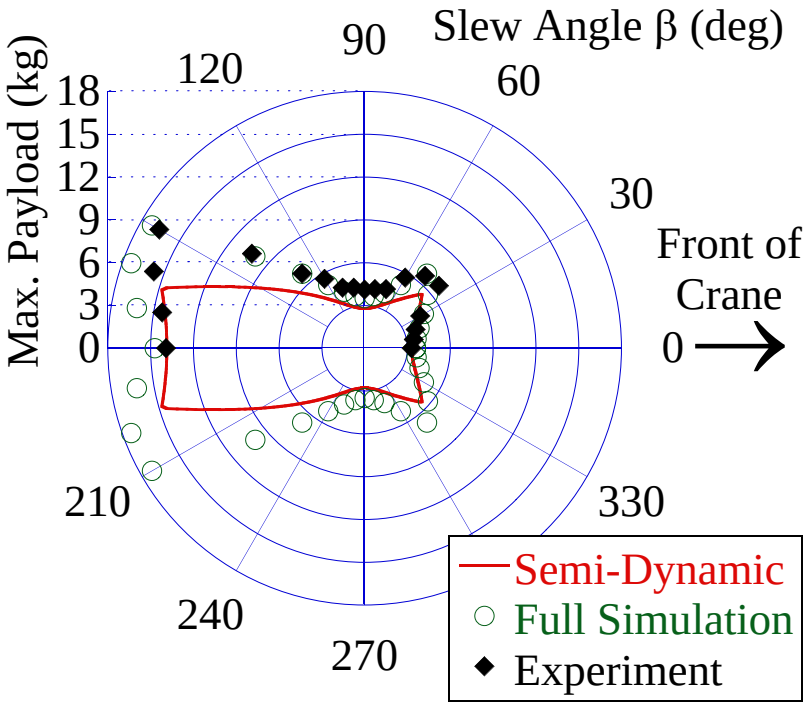

Figure 37: Maximum Payload for a Luff Angle of 45° and a Suspension Length of $1.45m$

For this longer suspension length, the semi-dynamic prediction underestimates the maximum payload over the whole range of slew angles. For high values of the luff angle α, the suspension length l used for the stability analysis of the crane should also be longer for practical reasons: If the boom is luffed at an higher angle, the suspension

length has to be increased to reach the ground. Thus, the crane is more likely to be operated with longer suspension lengths in these configurations. The experimental results for this case also closely match the simulation results.

Another way to determine the maximum possible payload for a given position of the boom is to determine the swing angle at which the bucking motion starts for each payload weight. The results of this approach illustrate the relationship between the maximum amplitude of the payload swing and the stability of the crane. The weight that causes the setup to buck exactly at the desired maximum swing angle is then the maximum possible payload for this configuration. For this purpose, a payload of appropriate mass was attached to the cable of the experimental setup and brought to a swing angle that caused a bucking motion. This bucking motion and the respective payload swing was recorded on video until the payload swing damped out and the setup stopped bucking. An image processing algorithm implemented in MATLAB was used to extract the payload swing and the bucking motion of the setup. To achieve these measurements, white styrofoam balls were attached to the cable and a white cardboard bar was mounted at the boom tip. These white markers were used to detect the payload and cart motions. Figure 38 shows part of the boom and the cable with theses markers attached.

In Figure 39, the results from the video processing during a typical test are displayed. The upper curve shows the payload swing angle over time and the lower graph shows the corresponding bucking angle. As can be seen in the lower graph, the setup is bucking at the beginning, indicated by the high frequency vibration in the signal. This high frequency oscillation is coming from the structural vibration of the setup and boom caused by the feet hitting the ground during the bucking motion. As the payload vibration amplitude gets lower over time, the setup stops bucking. The disappearance of the high frequency vibration occurs at about 16 seconds, the corresponding swing angle was detected to be 13.2° for this example, indicated by

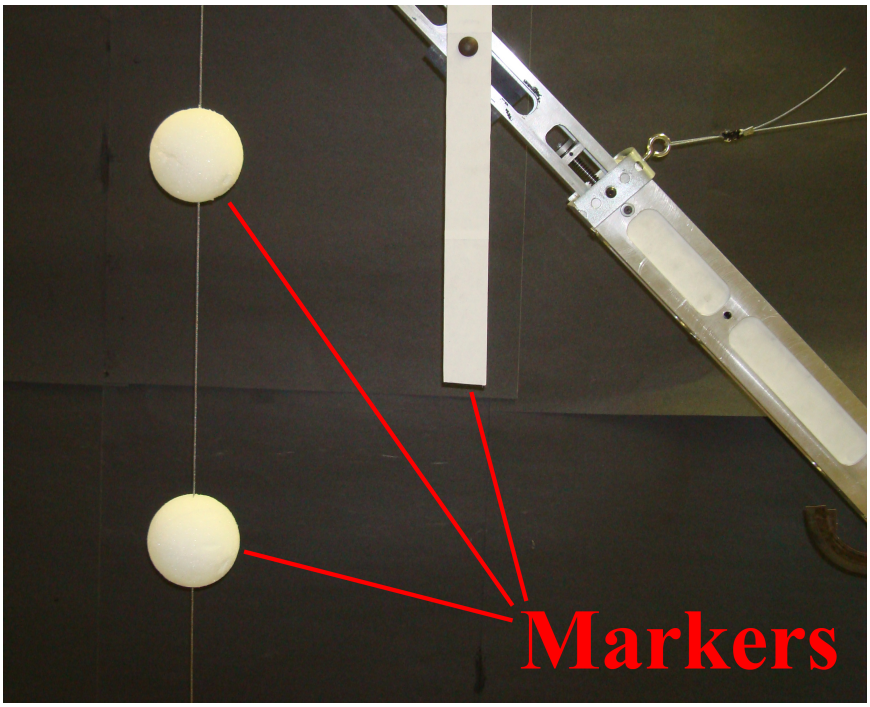

Figure 38: Markers to Detect Payload Swing and Bucking

blue dotted lines in the upper graph of Figure 39.

4.3 Straight-Line Base Motions

The simulation was also used to determine the values for the maximum possible payload when a maximum payload deflection in the longitudinal direction of $0.4077rad$ is caused by a bang-coast-bang acceleration/deceleration of the cart, as described in Section 3.3. As for the simulations in the previous section, a bucking motion was detected if two wheels lifted off from the ground simultaneously at any time during the maneuver. Figures 40 and 41 show these relationships for the same values of α as in the previous section. In this case, the estimation the inertia forces during the deceleration part of the command, as described in Section 3.5, is used in the semi-dynamic estimation. Thus, the maximum possible payload for $\alpha = 30°$ is still underestimated over the whole range of slew angles. For $\alpha = 45°$, the prediction meets the requirements for positions of the boom around $\beta = 90°$ and $\beta = 270°$, but

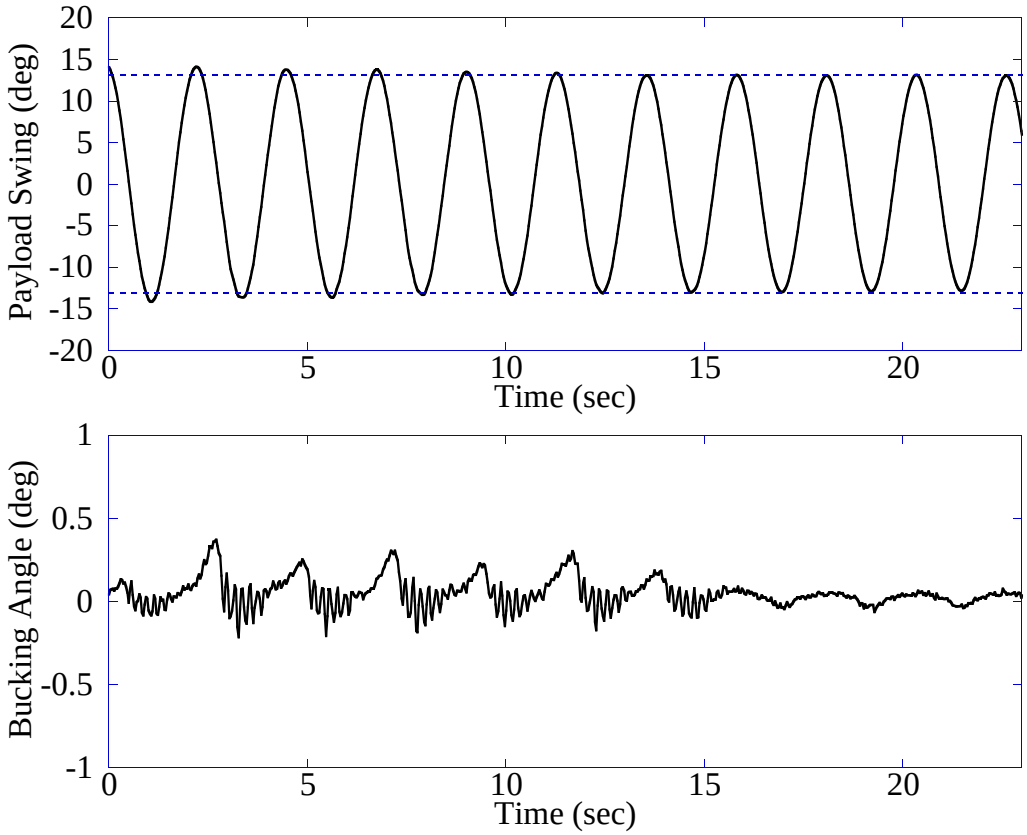

Figure 39: Payload Swing and Bucking Motion

still overestimates the maximum payload for slew angles around 0° and 180°.

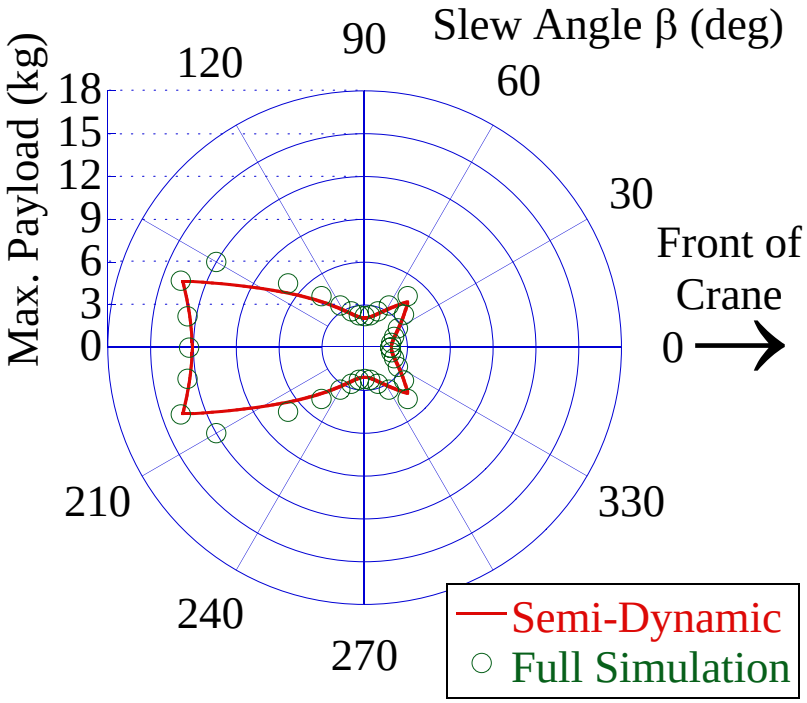

Figure 40: Maximum Payload for a Luff Angle of 30° (Straight-Line Motion)

The straight-line driving maneuver was also simulated for a suspension length of $1.45m$. Figure 42 presents the results for this increased suspension length. Like in the previous section, the semi-dynamic estimation for the straight-line maneuver also underestimates the maximum payload over the whole range of slew angles now. The estimation is very conservative for slew angles around 150° and 210°. This is due to the fact that the longitudinal payload deflection was also added in the lateral direction to compensate for the neglected centripetal force.

4.4 Cornering Base Maneuvers

In addition to straight-line motions of the cart, the boom crane simulation was also used to gain insights into the influences of cornering maneuvers on the payload swing angles. To accomplish this, the simulation was extended with a steering model for the base motion of the crane. The state-space representation for this steering model

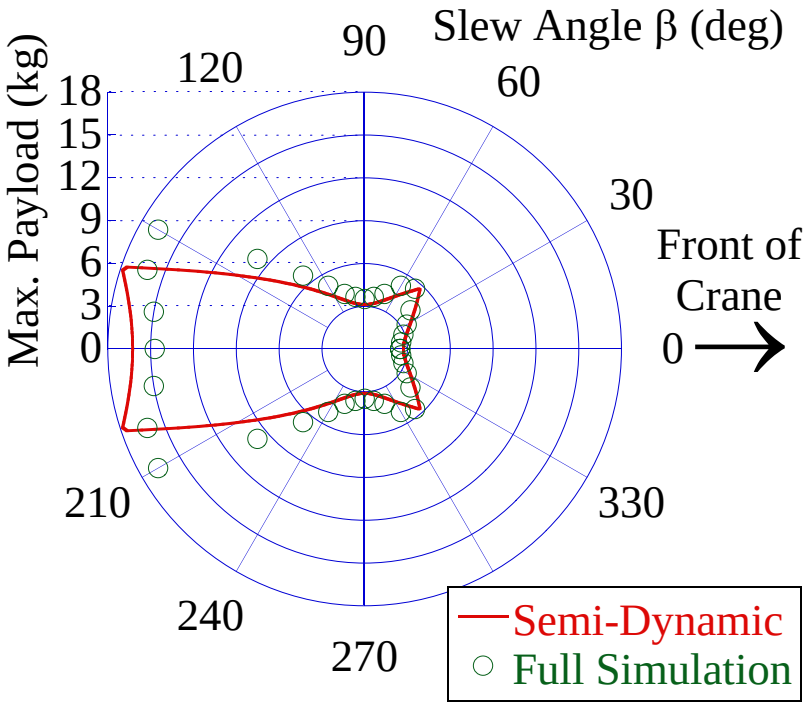

Figure 41: Maximum Payload for a Luff Angle of 45° (Straight-Line Motion)

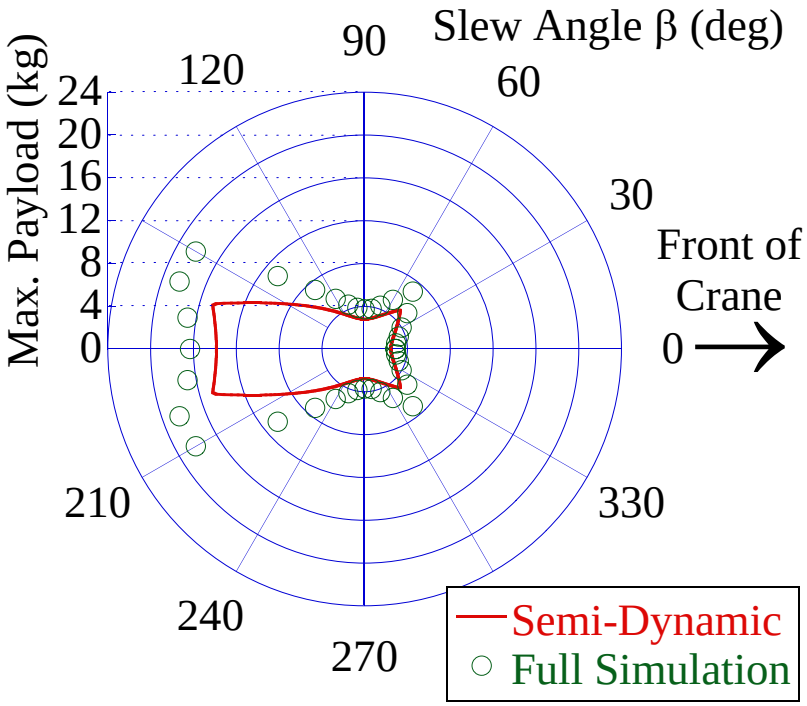

Figure 42: Maximum Payload for a Luff Angle of 45° and an Increased Suspension Length (Straight-Line Motion)

is:

$$\frac{d}{dt}\begin{pmatrix} x \\ y \\ \psi \\ \gamma \end{pmatrix} = \begin{pmatrix} \cos(\psi+\gamma) \\ \sin(\psi+\gamma) \\ \frac{1}{l_c}\sin\gamma \\ 0 \end{pmatrix} v + \begin{pmatrix} 0 \\ 0 \\ 0 \\ 1 \end{pmatrix} \dot{\gamma} \tag{4.1}$$

where v is the linear speed of the front axle in the forward direction, γ is the steering angle of the front axle, x and y describe the position of the front axle center point in the x-y-plane, ψ is the base orientation, and l_c measures the wheel separation in the longitudinal direction.

This steering model was included in the AUTOLEV and MATLAB code for the boom crane simulation. Thus, it is possible to simulate cornering maneuvers of the mobile crane base by specifying the linear speed of the base and the steering rate of the front axle.

First, the influence of the boom position during a cornering maneuver on the payload swing was investigated. The simulation was performed so that the crane base drove a quarter circle. The steering rate was chosen to be $0.35 rad/s$, the maximum steering angle was $0.35 rad$. For the dimensions of the crane listed in Table 1, this amounted to a radius of curvature of approximately $3m$ for the base center. Figure 43 illustrates the motion of the base center in the x-y-plane. The crane was started at a velocity of $1m/s$ without payload swing at the beginning of the cornering maneuver.

This maneuver was simulated with different positions of the boom. Figure 44 shows the maximum longitudinal swing angles as a function of the slew and luff angle caused by this cornering maneuver. Figure 45 shows the corresponding lateral swing angles. As can be seen, there is a strong dependence on the boom position. While the longitudinal swing has its maxima at slew angles of about $300° - 330°$, it reaches minimums at around $200°$. The lateral swing angles show peaks at slew angles around

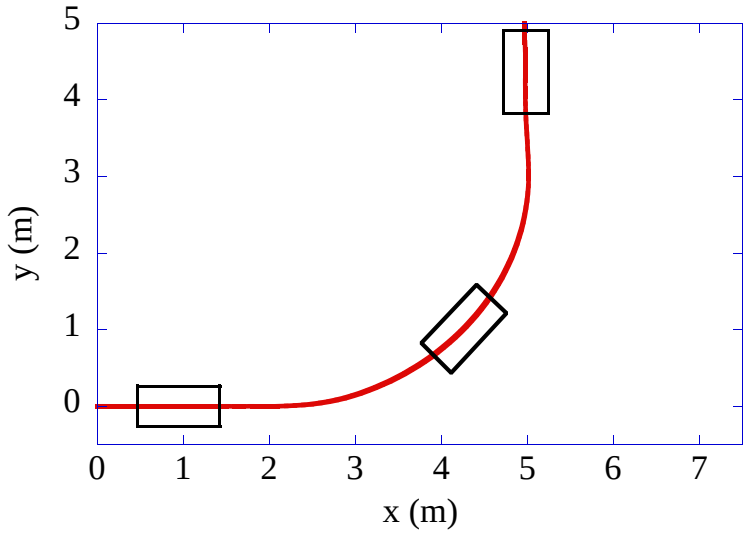

Figure 43: Base Center Position During a Cornering Maneuver

45° and minima at around 170°. The payload swing in both directions increases as the luff angle α decreases.

Figures 46 and 47 show the maximum longitudinal and lateral swing angles as a function of the cornering angle for three different values of the luff angle α and a slew angle β of 0°. In this case, a cornering angle of 0° describes a straight-line motion, a cornering angle of 360° means that the crane drives a full circle.

The longitudinal swing increases with the cornering angle up until a 100° turn. The value then stays fairly constant. The maximum lateral payload swing exhibits a significant dependence on the cornering angle over the whole range of cornering angles. Both swing directions have a similar dependence on the luff angle as described above for the quarter-circle maneuver. Both swing angles are zero for a cornering angle of 0°, which is a straight-line motion.

Another interesting effect observable in the simulations is that when the payload has an elliptical swing after the corner is finished, then the major axis of the ellipse rotates. If, for example, the longitudinal swing has a low value and the lateral swing has a high amplitude after the cornering maneuver, then this changes after several oscillation periods. Figure 48 shows the payload position relative to the boom tip in

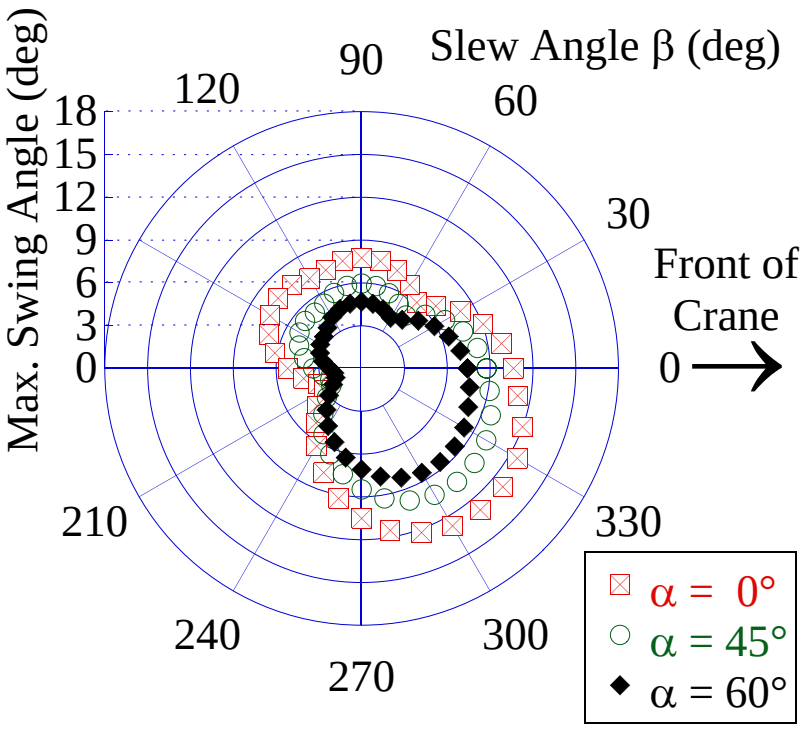

Figure 44: Maximum Longitudinal Swing Angle Caused by a Quarter-Circle Maneuver

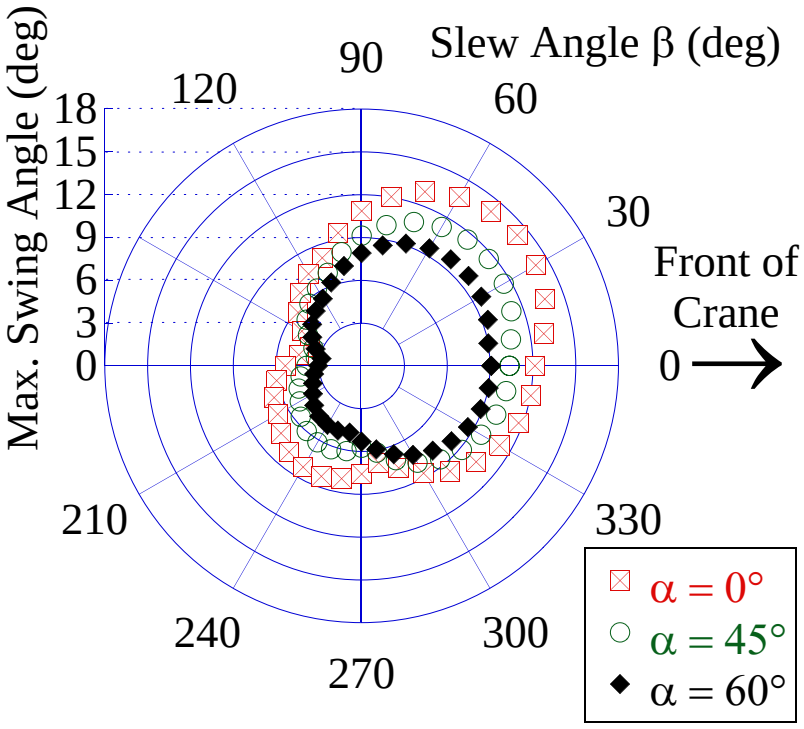

Figure 45: Maximum Lateral Swing Angle Caused by a Quarter-Circle Maneuver

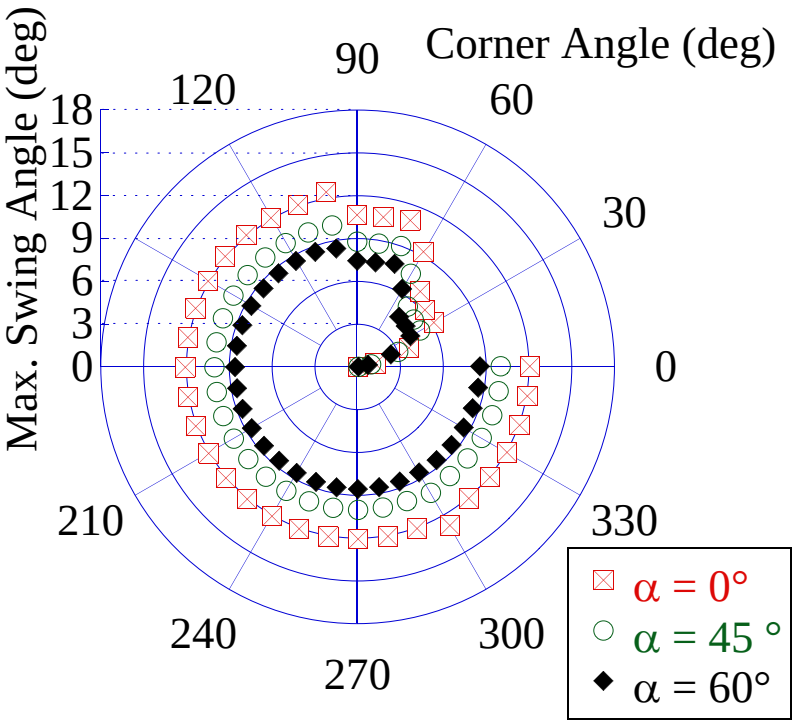

Figure 46: Maximum Longitudinal Swing Angle Caused by a Cornering Maneuver, $\beta = 0°$

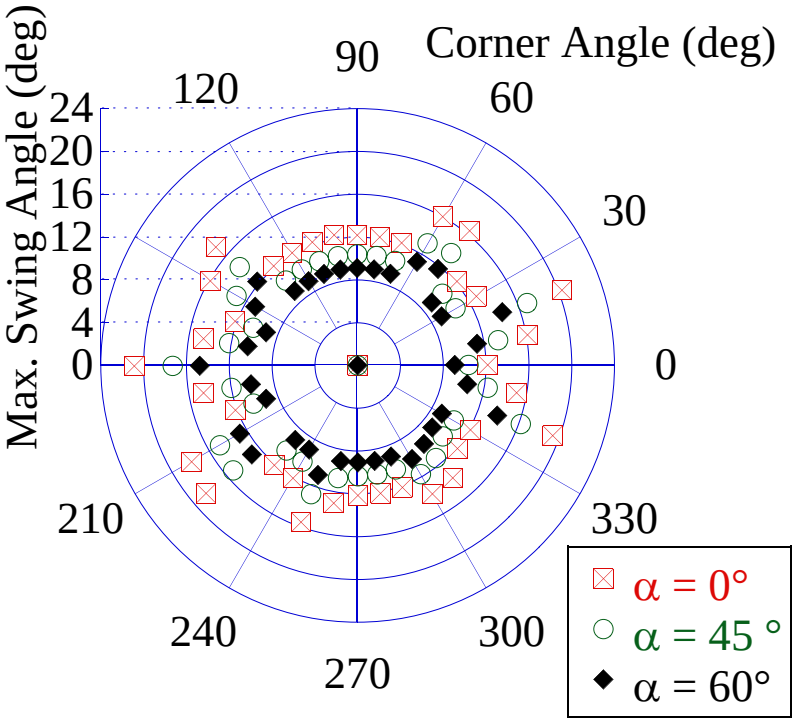

Figure 47: Maximum Lateral Swing Angle Caused by a Cornering Maneuver, $\beta = 0°$

the x and y direction for such a case.

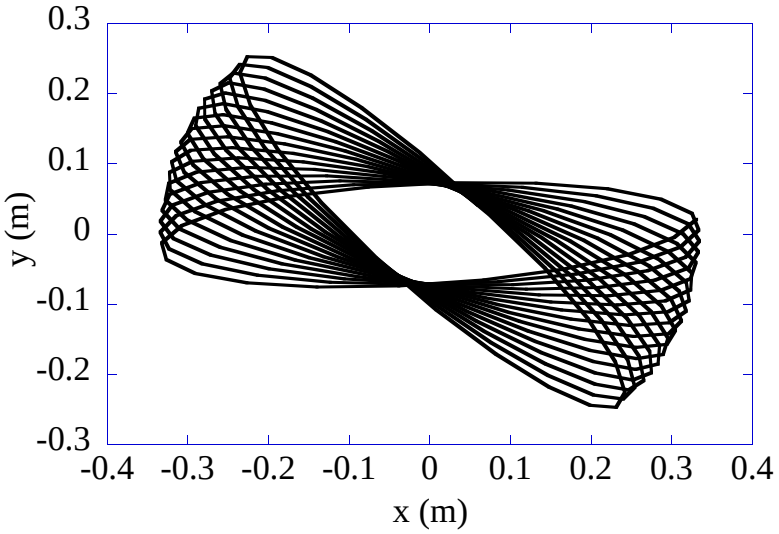

Figure 48: Wandering Elliptical Payload Swing After Cornering Maneuver

This wandering of the payload swing is due to the nonlinearity of the simulated pendulum and is also observed in real pendulums. To generate Figures 44 and 45, the swing angle recording was stopped after two oscillation periods after the cornering maneuver. In terms of a stability analysis, this wandering can have an impact on the results. A mainly longitudinal swing that does not cause the crane to tip over can become a lateral payload swing after a while and cause the crane to tip over to the side. In the simulations, this effect turned out to be of minor importance for the maximum payload. However, for the semi-dynamic stability estimation of the maximum payload, the payload swing along the major axis of the ellipse should be used as the maximum swing angle in both directions to get a conservative prediction of the maximum possible payload.

Given the high dependence of the maximum swing angles on parameters like slew, luff, and cornering angle and the lack of an estimation law for this maximum sway, no semi-dynamic prediction and subsequent comparison to the results of the dynamic simulation was conducted. Furthermore, the above described relationships for the maximum swing also depend on the steering rate, the steering angle and the radius of

curvature of the simulated maneuver. These dependencies could be subject to further investigations in the future.

4.5 Summary

At the beginning of this chapter, a schematic overview of a multi-body simulation of a mobile boom crane developed to simulate tip-over and bucking motions was given. This simulation was then used to determine the maximum possible payload for payload swing with a stationary crane base, as well as for straight-line driving maneuvers that induce payload swing. A bucking motion was detected if two wheels lifted off from the ground at the same time. The results were compared to the estimations of the semi-dynamic approach that was introduced in Chapter 3. It was shown that the semi-dynamic estimation delivers accurate results for small values of the luff angle α. For higher values of α, the semi-dynamic approach tends to overestimate the maximum payload. By increasing the suspension length to values that are necessary to reach the ground for the respective luff angle, the results of the estimation improved considerably. The approximation of the inertia forces introduced in Section 3.5 was proven to be a reasonable estimation for the influence of the cart and boom inertia on the stability of a mobile boom crane. In the last section of this chapter, the simulation was used to draw first conclusions about the effects of cornering maneuvers on payload swing.

CHAPTER V

EFFECT OF INPUT SHAPING ON STABILITY

It was shown in the previous chapters that payload swing has a significant influence on stability. This chapter investigates the stabilizing effects of input shaping. Given that input shaping greatly reduces payload swing, it will obviously improve stability, but the degree of improvement is an open question. In this chapter, traditional shapers like the ZV, the ZVD, and the UMZV shaper will be examined for their deflection-limiting properties and their impact on the maximum possible payload during straight-line driving maneuvers.

5.1 Zero-Vibration (ZV) Shapers

The simplest input shaper is the Zero-Vibration (ZV) shaper [39, 32]. Recall from the introduction that this shaper consists of two impulses, as shown in Figure 49.

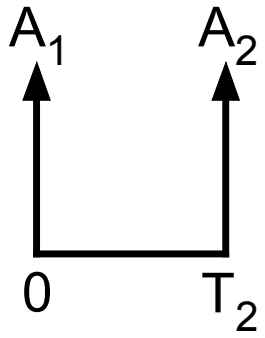

Figure 49: Zero-Vibration Shaper

The impulse amplitudes A_1 and A_2, as well as the impulse time T_2 depends on the natural frequency and the damping ratio of the system. Table 3 lists the formulas for these parameters, where ω is the natural frequency and ζ the damping ratio of the

system, and $k = e^{-\frac{\zeta\pi}{\sqrt{1-\zeta^2}}}$.

Table 3: Impulse Times and Amplitudes for a ZV Shaper

i	1	2
T_i	0	$\frac{\pi}{\omega\sqrt{1-\zeta^2}}$
A_i	$\frac{1}{1+k}$	$\frac{k}{1+k}$

In this thesis, only undamped systems are investigated. Most cranes exhibit a very low damping ratio, so this is a reasonable assumption. Thus, the $A_i s$ are both $\frac{1}{2}$ and T_2 equals $\frac{1}{2}T$, where T is the undamped oscillation period.

To investigate the deflection-limiting properties of the ZV shaper, a step in acceleration is assumed as the baseline command. The acceleration in this case is assumed to be $1m/s^2$ and the suspension length of the crane is $1m$. Figure 50 shows the acceleration command as a solid line and the payload response as a dashed line.

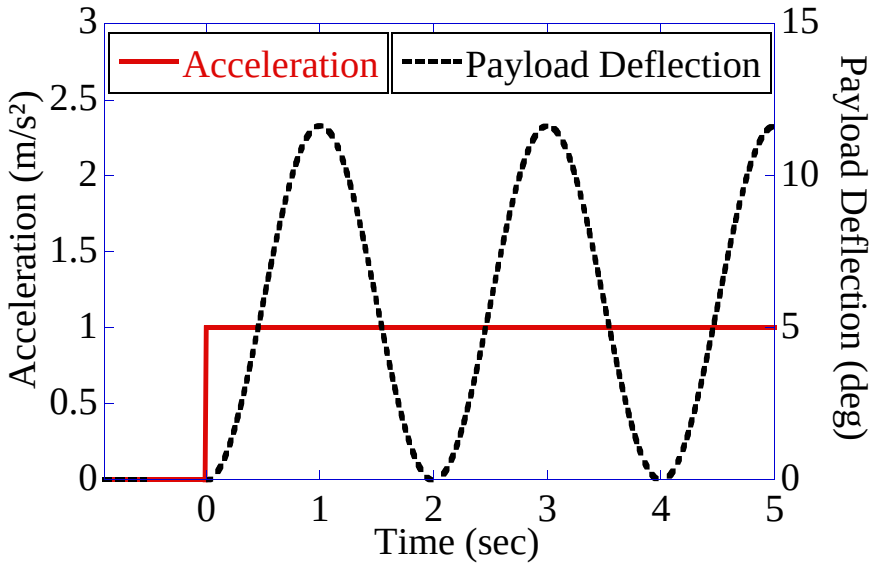

Figure 50: System Response for an Unshaped Step in Acceleration

The maximum payload deflection in this case is slightly below 12°, and because the crane is accelerating all the time, the payload swing angle does not become negative at any time. This result could have also been deduced from (3.14) in Section 3.3. A single step in acceleration shows up as $(1 - \cos(\omega t))$ and is the only time-dependent

term in this equation. Thus, the payload deflection never changes its sign.

The corresponding plot for the ZV-shaped step in acceleration is shown in Figure 51. This time, the payload response does not exhibit any residual oscillation after the acceleration command is issued and the maximum payload deflection is cut in half. This reduced payload swing obviously improves crane stability.

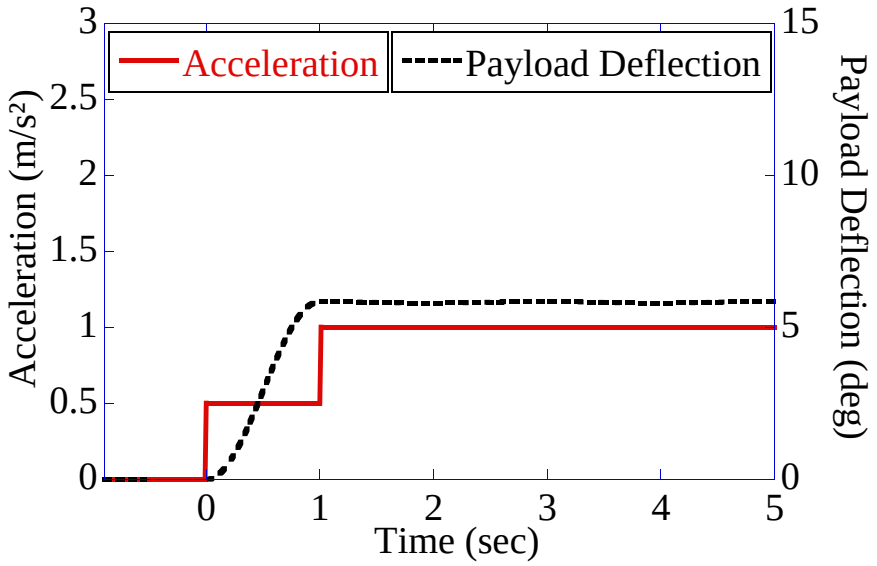

Figure 51: System Response for a ZV-Shaped Step in Acceleration

5.2 Zero-Vibration-Derivative (ZVD) Shapers

In this section, the robust Zero-Vibration-Derivative (ZVD) shaper is examined. This shaper consists of three impulses and is more robust to modeling errors than the ZV shaper. A thorough discussion of shaper robustness properties is given in [45]. Figure 52 illustrates the structure of this shaper. Table 4 gives the corresponding impulse amplitudes and times, where ω is again the natural frequency, ζ is the damping ratio of the system, and $k = e^{-\frac{\zeta\pi}{\sqrt{1-\zeta^2}}}$.

The shaped acceleration command and the corresponding payload response is displayed in Figure 53. The crane is brought to full acceleration in three steps, which causes a longer rise time of the system. The maximum payload deflection is still

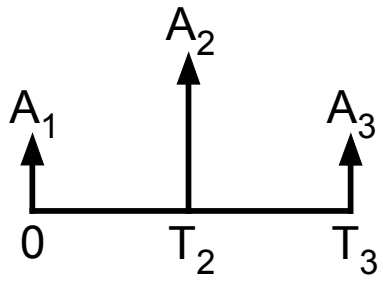

Figure 52: Zero-Vibration-Derivative Shaper

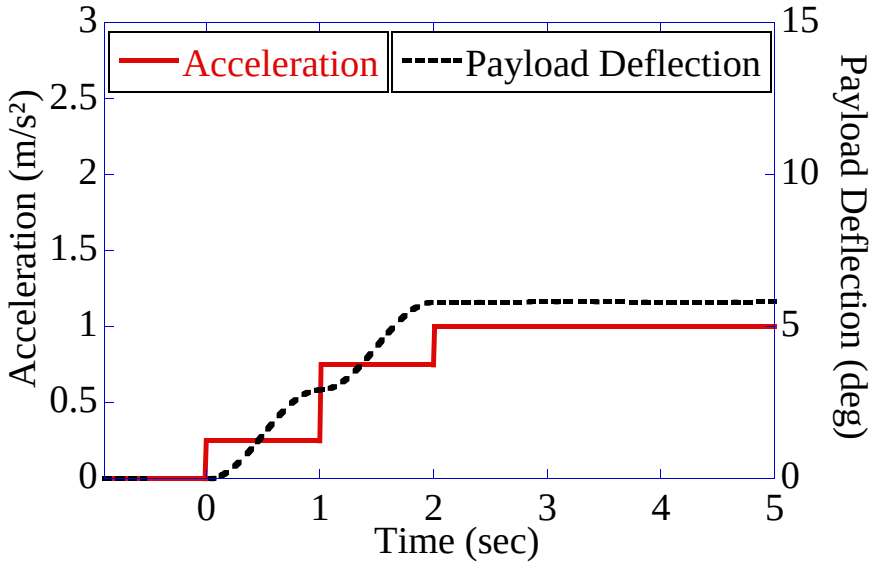

Figure 53: System Response for a ZVD-Shaped Step in Acceleration

Table 4: Impulse Times and Amplitudes for a ZVD Shaper

i	1	2	3
T_i	0	$\frac{\pi}{\omega\sqrt{1-\zeta^2}}$	$\frac{2\pi}{\omega\sqrt{1-\zeta^2}}$
A_i	$\frac{1}{(1+k)^2}$	$\frac{2k}{(1+k)^2}$	$\frac{k^2}{(1+k)^2}$

slightly below 6°, as in the ZV-shaped case. This value represents a lower bound for the payload deflection for an acceleration of $1m/s^2$. Figure 54 illustrates this fact graphically. Using D'Alembert's Principle, the deflection angle for a given acceleration can be determined by the triangle formed by the gravity force, the inertia force from the acceleration, and the cable force. Thus, the deflection is $\varphi = \arctan(\frac{a}{g})$, where a is the acceleration of the pendulum and g is gravity. It is not dependent of the payload mass m. For an acceleration of $1m/s^2$, this angle is 5.82°. A further reduction of the deflection is only possible if the maximum steady-state acceleration is reduced.

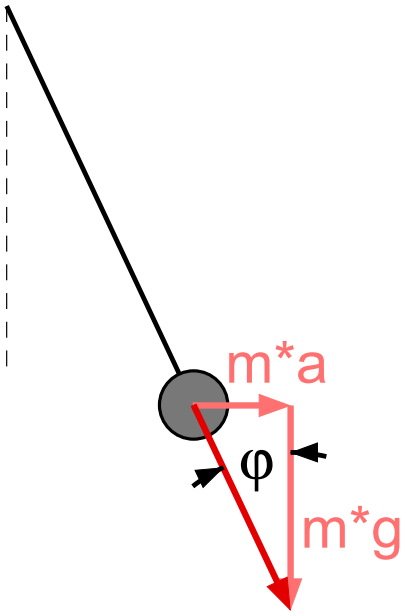

Figure 54: Payload Deflection Caused by a Horizontal Acceleration

5.3 Unity-Magnitude-Zero-Vibration (UMZV) Shapers

The ZVD shaper increased the rise time of the system by a factor of two compared to the ZV shaper, but it was not able to reduce the maximum payload deflection because the lower bound for the deflection was already reached with the ZV shaper. The advantage of the ZVD shaper is its higher robustness to modeling errors [32, 45]. Rather than designing input shapers for robustness, another goal is to minimize the system rise time, while still limiting the deflection to its lower bound.

The fastest known conventional shaper is the Unity-Magnitude-Zero-Vibration (UMZV) shaper. An extensive discussion of this type of negative shaper is provided in [37]. Its structure for undamped systems is shown in Figure 55. Table 5 lists the corresponding impulse amplitudes and times.

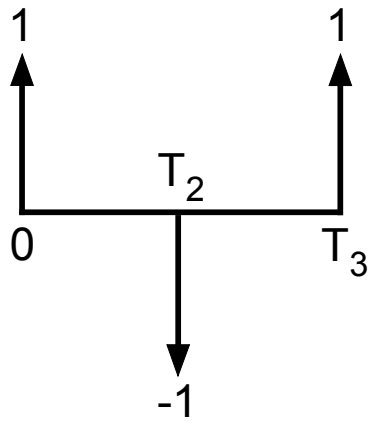

Figure 55: Unity-Magnitude-Zero-Vibration Shaper

Table 5: Impulse Times and Amplitudes for a UMZV Shaper

i	1	2	3
T_i	0	$\frac{\pi}{3\omega}$	$\frac{2\pi}{3\omega}$
A_i	1	-1	1

The impulses of this shaper alternate between 1 and -1. This is especially suitable for the control of on-off actuators. By allowing negative amplitude values, the duration of the shaper can be decreased significantly compared to positive amplitude

shapers. For the undamped case, this shaper has a duration that is 33% shorter than the ZV shaper. The cost is a lower robustness against modeling errors and increased high mode excitation [37]. Figure 56 presents the shaped acceleration command and the payload response to the UMZV-shaped step command.

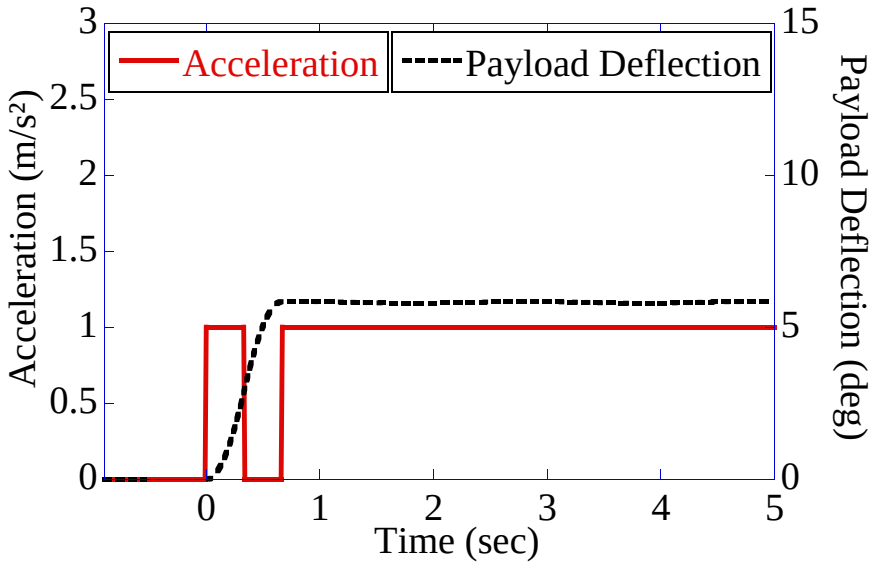

Figure 56: System Response for a UMZV-Shaped Step in Acceleration

As shown in Figure 56, the UMZV shaper is the only shaper in this comparison that does not exhibit a monotonously increasing shaped acceleration command. Nevertheless, the UMZV shaper has the shortest rise time in this comparison and still limits the maximum payload deflection to half the amount of the unshaped case.

5.4 Effects on Mobile Boom Crane Stability

The previous chapters showed that payload swing has a negative impact on boom crane stability. The shapers described in the previous subsections all decrease payload deflection compared to the unshaped case and should thus increase the stability of a boom crane. To prove this, the crane simulation introduced in Chapter 4 was used to perform straight-line driving maneuvers. As a baseline command, a bang-coast-bang command with a maximum acceleration of $1m/s^2$ and a maximum velocity of $1m/s$

which caused the crane to move $3m$ in the forward direction was utilized. This is the worst-case scenario for the resulting maximum payload swing in the unshaped case, which is $0.4077rad$ (23.36°). The same moves were simulated with ZV-, ZVD- and UMZV-shaped acceleration commands. Figure 57 shows the resulting maximum payload values as a function of the slew angle for a luff angle α of 45°. Figure 58 shows a zoomed in view of the data.

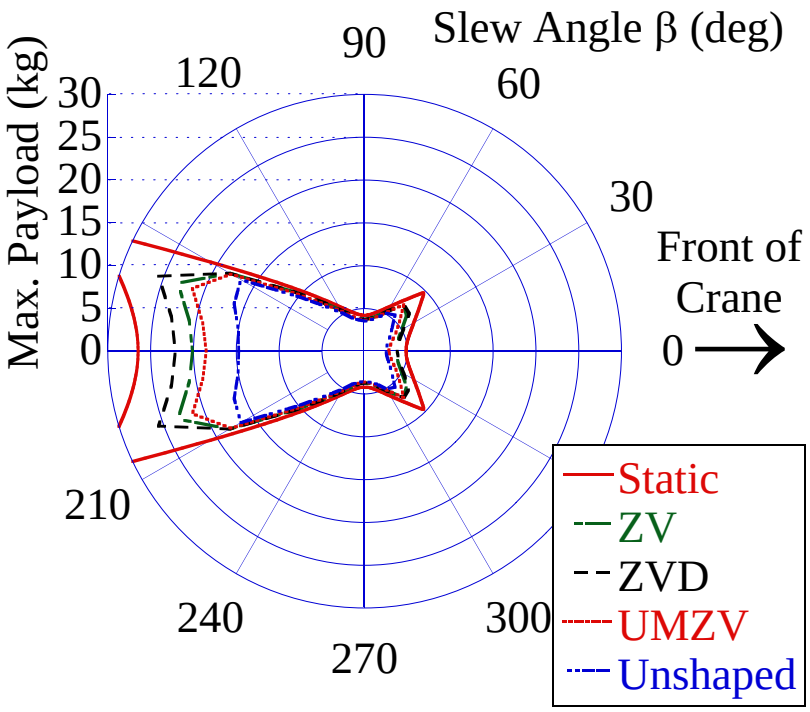

Figure 57: Effects of Different Shapers on Maximum Payload for a Straight-Line Maneuver

Although the previous section showed that the ZV, the ZVD and the UMZV shaper all reduced the deflection of a step in acceleration by half, the stability results in Figure 57 deviate considerably from each other. This is because the baseline command in this case consists not of a single step, but of two pulses in acceleration. If these pulses are shorter than the duration of the shaper, then the shaped command will not reach the maximum acceleration. This can decrease the maximum payload deflection below the lower bound for a step command, as discussed above.

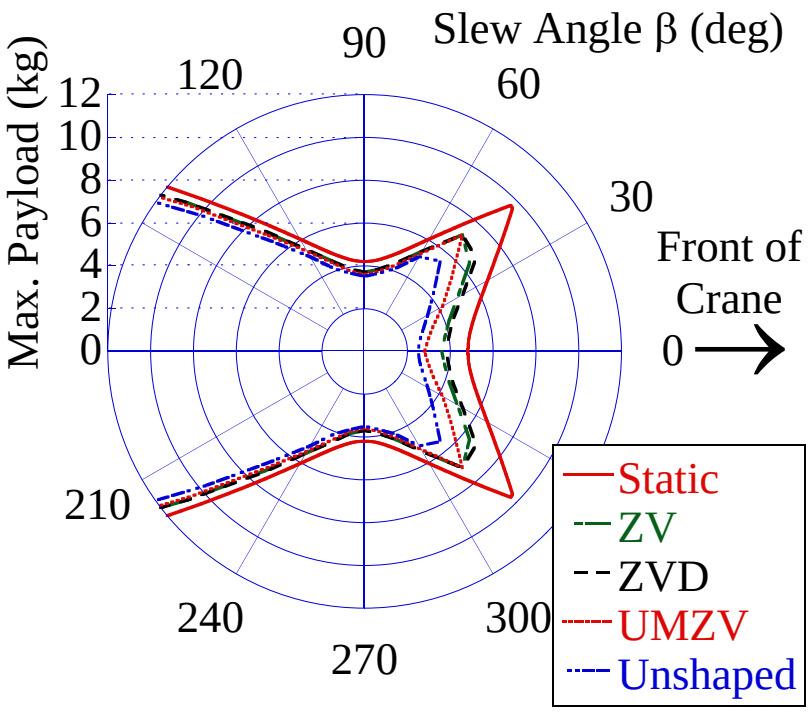

Figure 58: Effects of Different Shapers on Maximum Payload for a Straight-Line Maneuver, Zoomed View

Figure 59 shows the unshaped acceleration command, as well as the corresponding payload response. Because this command is a combination of four step commands timed so that the vibrations induced by each step add up constructively, the peak-to-peak payload swing angle is now four times as large as the maximum payload swing caused by a single step in acceleration. The maximum swing angle for this bang-coast-bang command was already determined analytically in Section 3.3. As could be seen in the previous section, a ZVD shaper for a step in acceleration of $1m/s^2$ should induce a maximum payload deflection of slightly less than 6°. Because a ZVD-shaped bang-coast-bang command exhibits zero residual vibration after each step in acceleration, the deflections do not add up with input-shaped commands.

However, Figure 60 shows a maximum deflection of less than 3° (not 6°) in both directions. This is due to the fact, that the shaper duration is about twice as long as one of the acceleration pulses of the bang-coast-bang command. Thus, the shaped

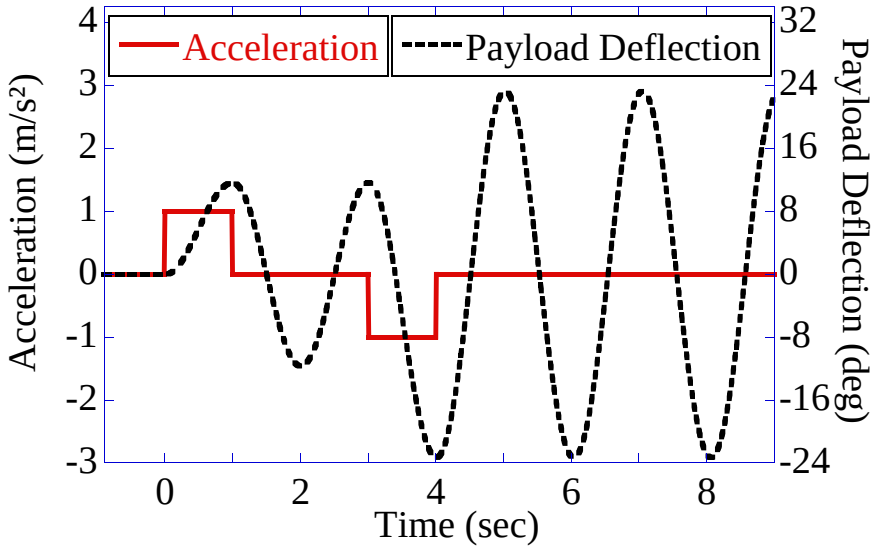

Figure 59: System Response for an Unshaped Bang-Coast-Bang Command in Acceleration

command does not reach the maximum acceleration of $1m/s^2$ and limits the transient deflection even further. A UMZV-shaped command always reaches the maximum acceleration immediately because the first impulse of the shaper is equal to one. Thus, a UMZV shaper does not exhibit this deflection reduction for short-duration baseline commands.

Considering these facts, the differences in the maximum payload for the different shapers shown in Figure 57 can be explained. The ZVD shaper delivers the highest gain in maximum payload because it reduces the maximum acceleration to below the level of the step input. The ZV shaper also reduces the maximum acceleration in this case, but because the shaper duration is about as long as one of the acceleration pulses, this is exactly the borderline case. As a result, the maximum deflection still stays on the same level as for the step baseline command. Nevertheless, the reduced acceleration has a reducing effect on the inertia forces acting on the base and the boom. The UMZV shaper performs worse than the other shapers in this comparison because it provides full acceleration of the crane base and limits the maximum deflection to the same level as for the step baseline command. However, it

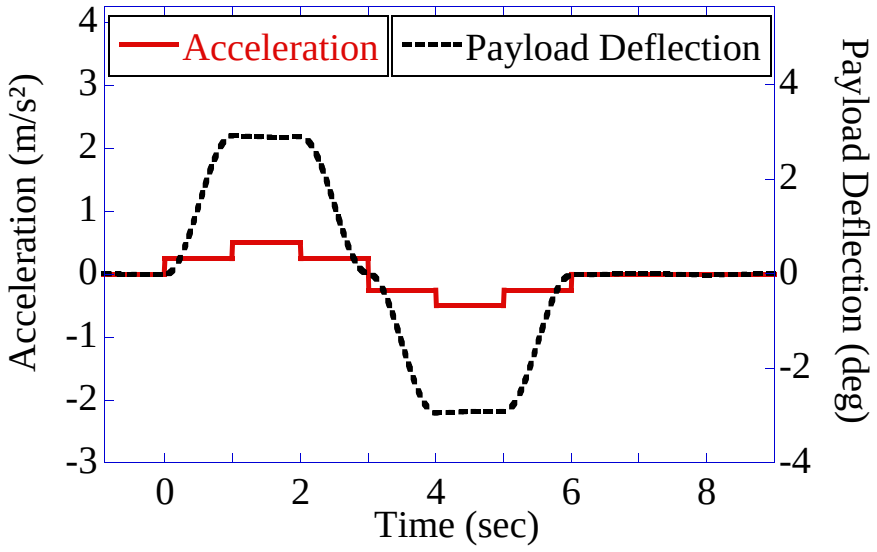

Figure 60: System Response for a ZVD-Shaped Bang-Coast-Bang Command in Acceleration

is also the fastest of the three shapers. The red solid line in Figure 57 displays the result of the static stability analysis which acts as an upper bound in this case. No acceleration command will ever be able to increase the maximum possible payload beyond this limit.

5.5 Robustness to Modeling Errors

This section investigates the impact of modeling errors on the effects of input shaping on mobile boom crane stability. The shapers in the previous section were all designed assuming that the properties of the controlled system are perfectly known. In reality, every system model is subject to modeling errors. These modeling errors can degrade the performance of the controller.

For a crane, the most important system parameters are the damping ratio and the oscillation frequency of the payload swing. As already mentioned in Section 5.1, most cranes have a very low damping ratio. Thus, an error in the assumed damping ratio does not have a significant influence on the control performance. In most cases, the effect of the damping ratio can be completely neglected.

The oscillation frequency, which is largely determined by the suspension length of the payload, is more critical for the design of a controller. Simulations were performed to determine the effects of a modeling error in the suspension length on the stability of a mobile boom crane during straight-line driving maneuvers. The crane configuration from the previous section was used. However, the input shapers were designed with a 10% error in the assumed suspension length. Instead of for $l = 1.0m$, the shapers were designed for $l = 1.1m$. Figure 61 shows the shaped acceleration command and the payload response when the ZV shaper was used.

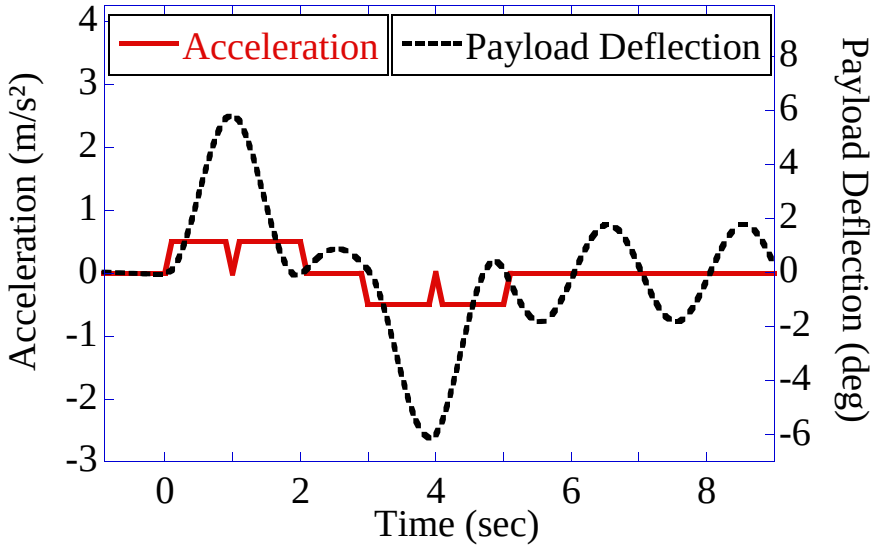

Figure 61: System Response for a ZV-Shaped Bang-Coast-Bang Command in Acceleration for a Modeling Error in the Suspension Length

The ZV shaper that was designed for a suspension length of $1.1m$ increases the maximum deflection to slightly more than 6°. In addition, the maximum amplitude of the residual vibration after the driving maneuver is now about 2°.

Figure 62 shows the maximum possible payload for the shapers designed for the wrong suspension length, as well as the unshaped and the static case. In Figure 63, a zoomed in view of this plot is shown. By comparing this data with Figures 57 and 58, it is obvious that the maximum possible payload has hardly changed. Therefore,

shapers based on the wrong suspension length still provide a good stability benefit. The reason for this is that the maximum payload deflection was only slightly increased. The residual vibration, which increased significantly for the modeling error, is still much smaller than the maximum payload deflection during the driving maneuver. Thus, it does not have a negative influence on stability.

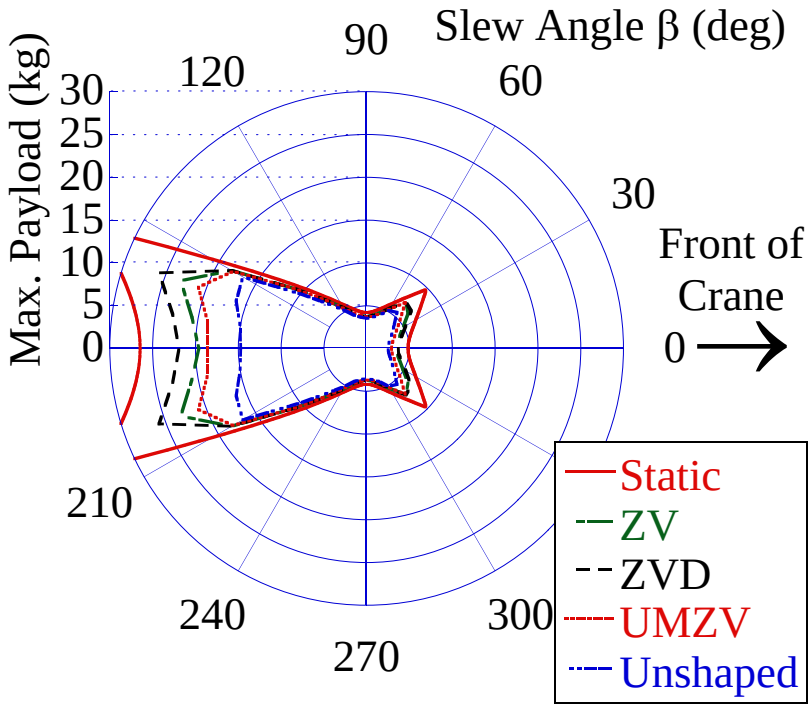

Figure 62: Effects of Different Shapers on Maximum Payload for a Straight-Line Maneuver and a Modeling Error in the Suspension Length

5.6 Summary

In this chapter, the deflection-limiting properties of traditional shapers like the ZV, the ZVD, and the UMZV shaper were investigated. For a step in acceleration as a baseline command, the shapers all limit the maximum deflection to 50% of the unshaped case. However, they provide different performance in rise time and other properties like robustness and high-mode excitation.

If the baseline command is a bang-coast-bang command with acceleration pulses

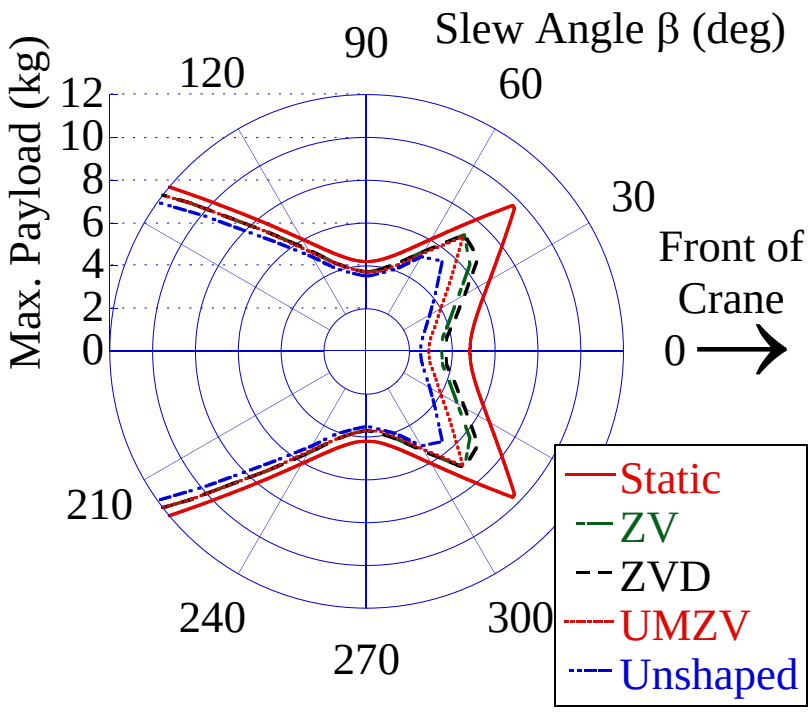

Figure 63: Effects of Different Shapers on Maximum Payload for a Straight-Line Maneuver and a Modeling Error in the Suspension Length, Zoomed View

that are shorter than the shaper duration, then the ZV and the ZVD shapers can reduce the transient deflection even further because the shaped command does not reach the maximum acceleration. The UMZV shaper does not share this behavior. Therefore, it does not improve stability as much as the other shapers. For all shapers, the maximum possible payload for the static case acts as an upper bound that cannot be exceeded.

The last section of this chapter investigated the robustness of the stability properties of input shapers to modeling errors. For a 10% error in the suspension length, none of the investigated shapers showed a significant change in the maximum possible payload during straight-line driving maneuvers.

CHAPTER VI

DESIGN OF SPECIFIED-DEFLECTION SHAPERS IN THE ACCELERATION DOMAIN

The previous chapter showed that the deflection-limiting properties of shapers like the ZV and the ZVD shaper depend on the baseline command that is issued to the system. The UMZV shaper is less sensitive to changes in the baseline command. This fact will be used to design specified-deflection shapers with a minimum rise time in this chapter.

6.1 Deflection Vector Diagrams

The vector diagrams shown in the introduction are useful tools for designing input shapers. However, the standard form of vector diagrams only conveys the residual vibration, but does not indicate the transient deflection caused by the input shaper. In the past, special deflection vector diagrams were developed to compensate for this deficiency. However, these deflection vector diagrams were limited to step inputs in position as the baseline commands [31]. In this section, a new form of deflection vector diagrams for step inputs in acceleration as baseline commands is introduced.

The construction of a deflection vector diagram will be shown for the shaper in Figure 64. This shaper consists of two positive and one negative impulse and exhibits non-zero residual vibration, as can be shown with a standard vector diagram. The diagram on the left side of Figure 65 shows the first step of the construction of a deflection vector diagram for this shaper.

The first impulse is drawn in the phase plane, indicated as a light blue vector, as with a regular vector diagram. In a deflection vector diagram, this vector rotates

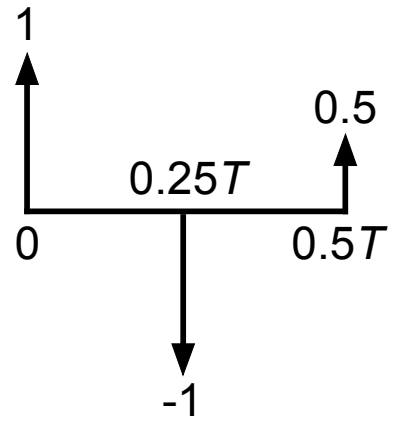

Figure 64: General Shaper

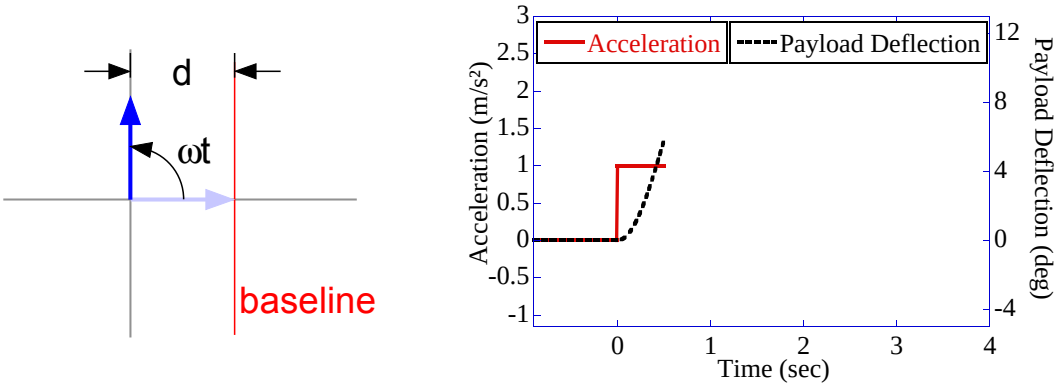

Figure 65: Deflection Vector Diagram for a General Shaper: Step 1

around the origin with an angular velocity of ω, the system natural frequency. This rotation is shown by the dark blue vector. In addition to the initial vector, a baseline is drawn. This baseline goes through the tip of the vector representing the first impulse at $t = 0$ and is perpendicular to it. The deflection caused by this impulse is proportional to the distance between the wandering deflection vector tip and the baseline, indicated as d in Figure 65. Mathematically, this distance equals $A_1(1 - \cos(\omega t))$, where A_1 is the impulse amplitude and t is time. This deflection-describing distance is derived from the payload response to a step input in acceleration, as described in (3.14) of Section 3.3. The graph on the right side of Figure 65 shows a corresponding simulation result for a pendulum with a suspension length of $1m$. As can be seen, the payload deflection increases after the first step in acceleration.

The deflection vector diagram changes when a new impulse is added. Therefore, the new impulse has to be added to the current deflection vector in the horizontal direction. The resultant vector then rotates around the origin of the diagram with an angular velocity of ω. In addition to that, the baseline has to be shifted by the length of the new impulse, to the right for positive impulses, to the left for negative impulses. Figure 66 illustrates this procedure for the second impulse of the shaper shown in Figure 64. In this case, the second impulse, indicated as a light blue dashed vector, is negative and thus has to point to the left when added to the current deflection vector. The second impulse is also drawn on the horizontal axis of the diagram to indicate the baseline shift. After the second impulse, the baseline is coincident with the vertical axis of the diagram. The resultant deflection vector is shown as a dark blue vector. In the simulation results on the left side of Figure 66, the negative impulse shows up as a negative step in acceleration. After adding the second impulse and shifting the baseline, the deflection d is still the same as right before the second impulse occurred. This is reasonable and necessary because the deflection cannot change instantaneously.

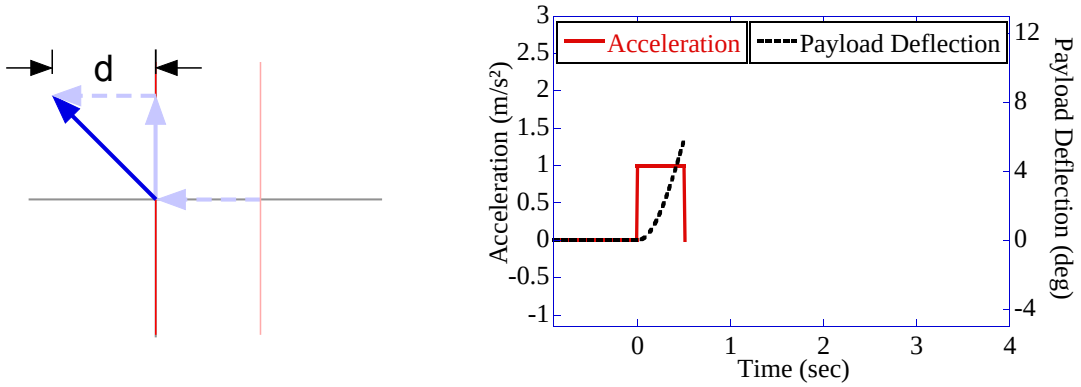

Figure 66: Deflection Vector Diagram for a General Shaper: Step 2

The new resultant vector rotates around the origin, as shown in Figure 67. After reaching a maximum, the deflection decreases until the third impulse occurs.

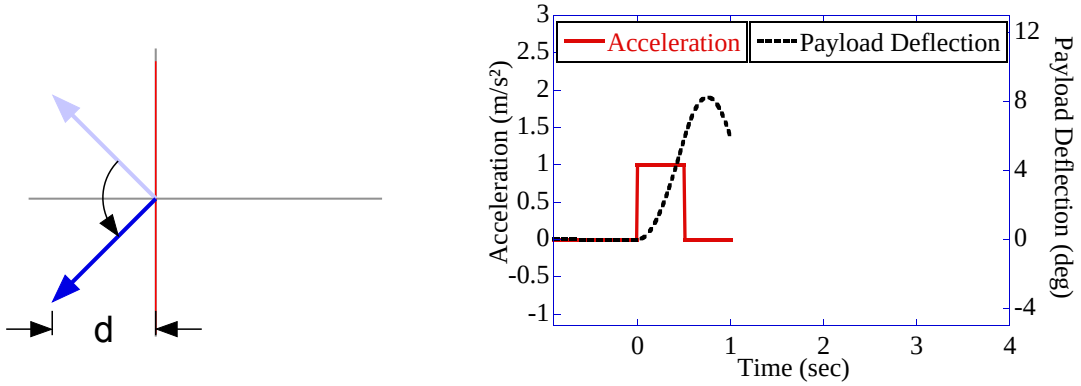

Figure 67: Deflection Vector Diagram for a General Shaper: Step 3

The third impulse is positive and thus shifts the baseline to the right. The vector itself is added to the current deflection vector in the horizontal direction. This is shown on the diagram on the left side of Figure 68. In the simulation results displayed on the right side of Figure 68, the third impulse shows up as a positive step in acceleration.

After the last impulse, the resultant deflection vector rotates around the origin with an angular velocity of ω. During certain phases of this rotation, the tip of the deflection vector crosses the baseline, as shown on the diagram on the left side of

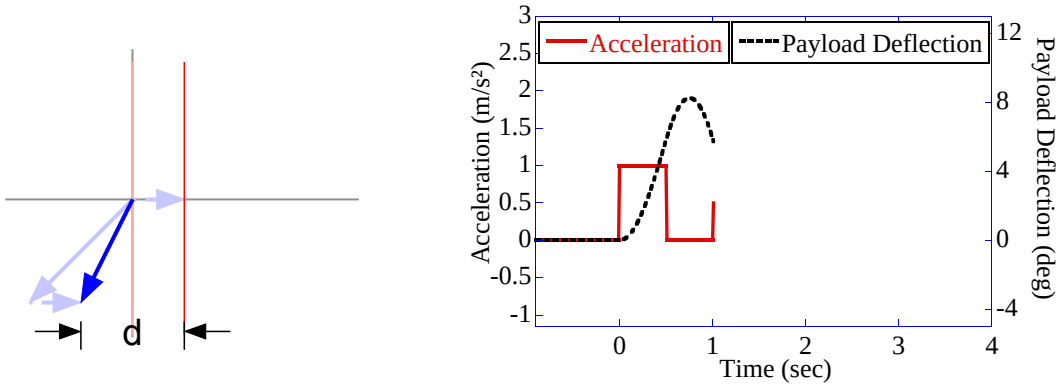

Figure 68: Deflection Vector Diagram for a General Shaper: Step 4

Figure 69. This indicates that the payload deflection becomes negative during that time. The graph on the right side of Figure 69 shows the corresponding simulation results.

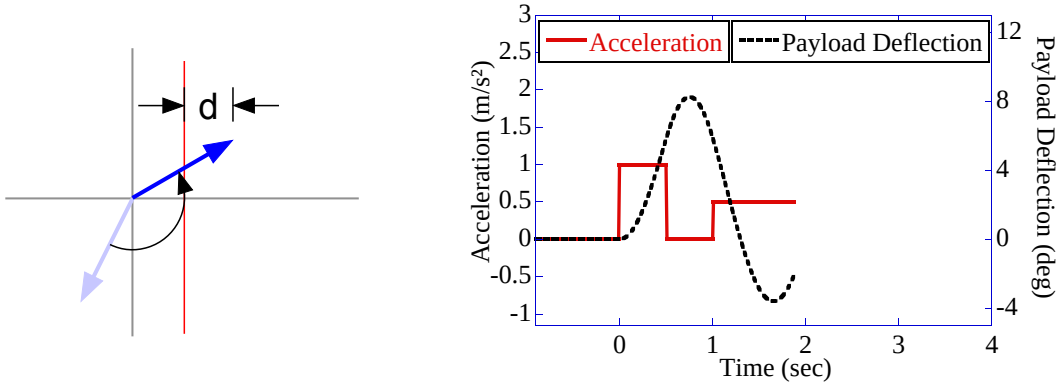

Figure 69: Deflection Vector Diagram for a General Shaper: Step 5

The curve of the payload oscillation does not change its shape after the third impulse anymore, which is shown in Figure 70. The maximum deflection caused by this acceleration command also occurs during this final phase. This can also be followed from the deflection vector diagram by determining the maximum distance between the tip of the deflection vector and the baseline during the command.

As a second example, the deflection vector diagram for a ZV shaper is derived. Figure 71 shows a series of deflection vector diagrams for the ZV shaper on the left

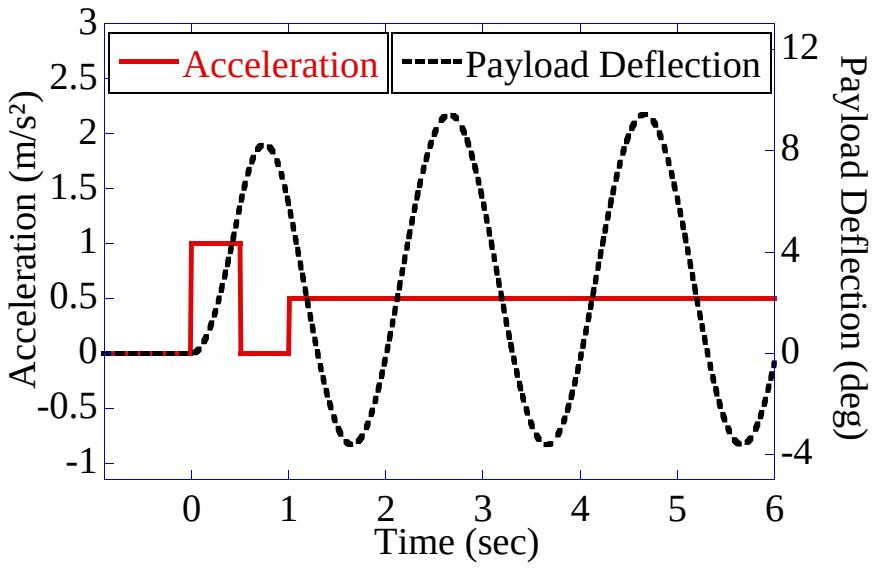

Figure 70: Complete System Response for a Shaped Step in Acceleration

side, and graphs with the corresponding simulation results on the right side. After the first impulse, the deflection increases, as shown in the first two diagrams and the simulation results. The deflection reaches its maximum right before the second impulse occurs, indicated on the third diagram. After the second impulse is added, shown as a light blue dashed arrow at the origin on the fourth diagram in Figure 71, the resultant vector is the zero vector and the baseline is shifted to the right, indicated by the second light blue dashed vector. This leads to a constant level of the deflection after the shaped command is issued. The simulation results on the right side of Figure 71 substantiate these results.

In order to translate the deflection determined through a deflection vector diagram into a payload swing angle, the deflection in units has to be multiplied by the term $\frac{M}{g}$, where M is the magnitude of the step baseline command in acceleration, and g is gravity. For an unshaped step, which can be represented by an impulse of magnitude 1 in a deflection vector diagram, this maximum deflection is 2 $units$. This corresponds to a maximum deflection angle of $0.2039rad$ (11.68°) if the magnitude of the acceleration command is $1m/s^2$. For the ZV shaper in Figure 71, the maximum

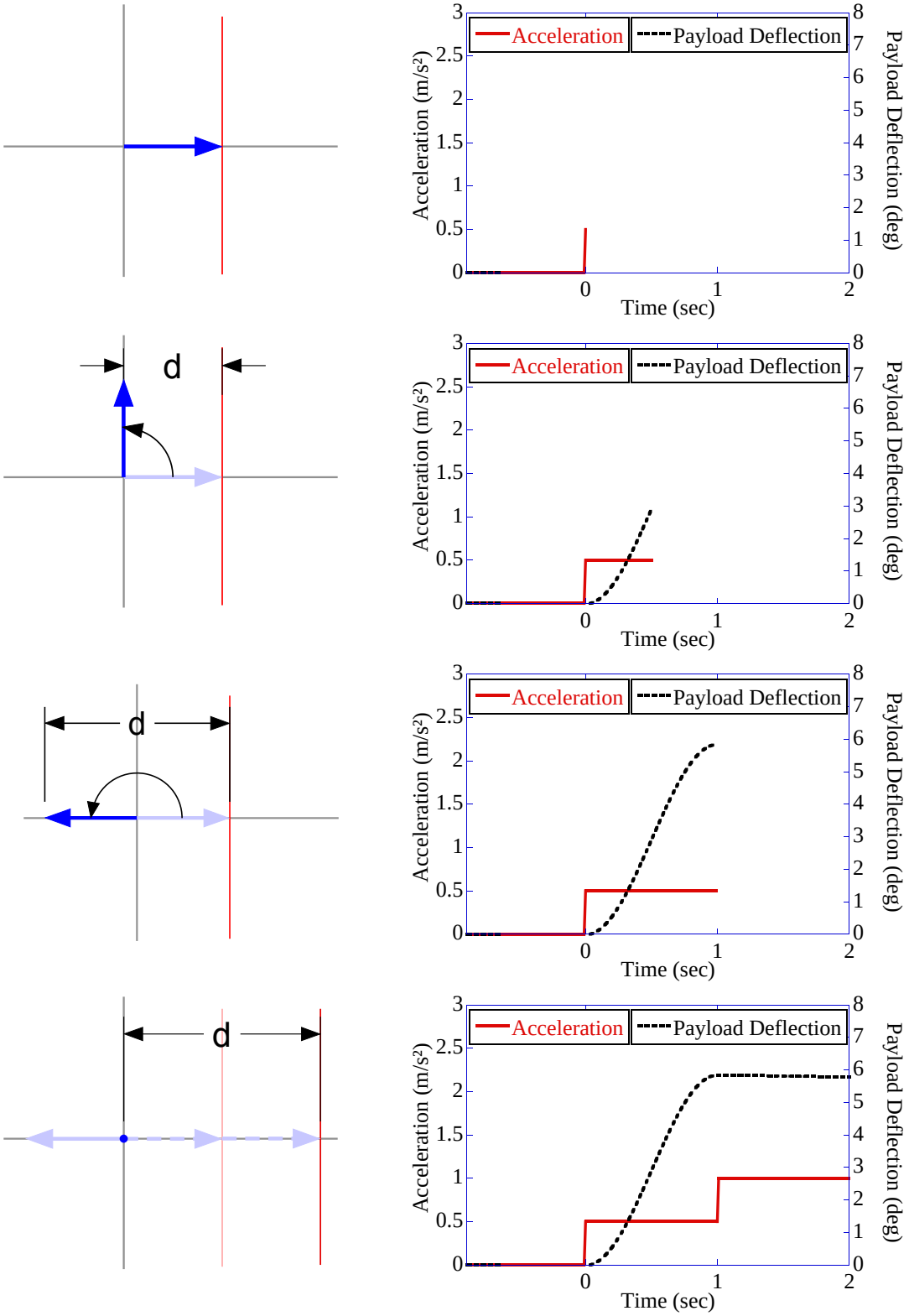

Figure 71: Deflection Vector Diagrams and Corresponding Payload Response for a ZV-Shaped Step in Acceleration

deflection obtained through the deflection vector diagram approach is 1 $unit$, which corresponds to a maximum deflection angle of $0.1019rad$ (5.84°) for an acceleration of $1m/s^2$. This complies with the simulation results on the right side of Figure 71. Mathematically, these results can be followed from (3.14) of Section 3.3.

6.2 Specified-Deflection-Negative-Amplitude Shapers

Chapter 5 showed that the UMZV shaper is the fastest shaper that limits the maximum payload deflection to half the amount of the unshaped command for a step in acceleration.

Figure 72 shows a series of simulation results for a crane that was accelerated by a UMZV-shaped step command. The payload suspension length was $1m$. The corresponding vector diagrams are shown on the left side. As can be seen on the right side of the graphs, the deflection ramps up after the first step in acceleration. The corresponding deflection vector diagram shows the first impulse occurring at $t = 0$ as a light blue arrow, as well as the current deflection vector, which is rotating around the origin of the diagram. In the second vector diagram, the current deflection vector is shown as a solid, light blue arrow, and the second impulse is shown as dashed, light blue arrow. The resultant deflection vector after the addition of those two vectors is displayed as a solid dark blue arrow. This vector rotates around the origin with an angular velocity of ω until the third impulse occurs, as indicated on the third diagram. After one negative and one positive impulse of magnitude 1, the baseline is coincident with the vertical axis of the diagram. The fourth vector diagram shows the current deflection vector as a solid, light blue arrows, and the third impulse as a dashed, light blue arrow. The resultant vector is the zero vector, indicated as a dark blue circle at the origin, and the baseline is shifted to the right. The corresponding simulation results prove the constant character of the payload deflection after the third impulse.

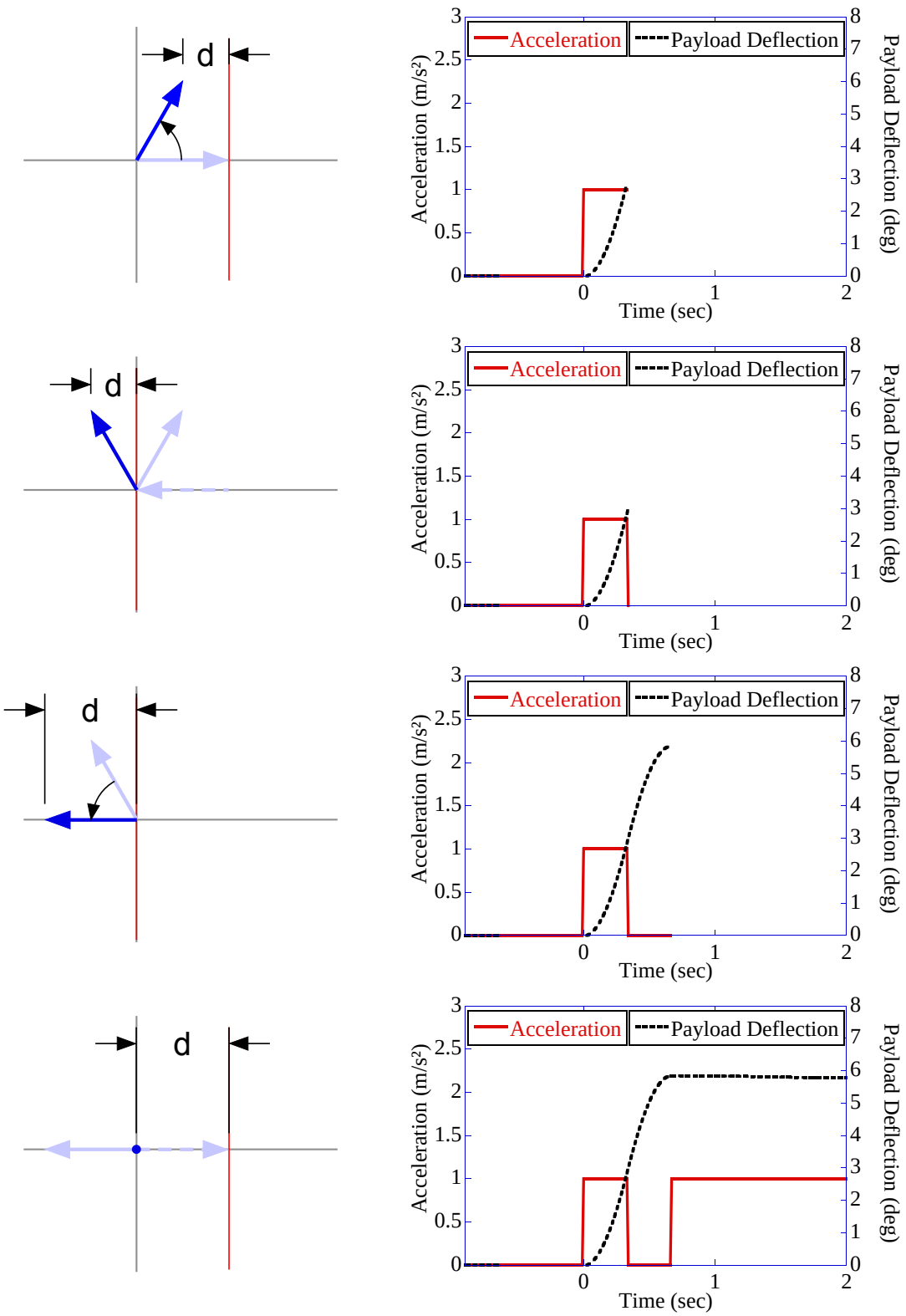

Figure 72: Deflection Vector Diagrams and Corresponding Payload Response for a UMZV-Shaped Step in Acceleration

The goal of this section is to adapt the UMZV shaper in a way so that the maximum payload deflection can be limited to values less than 50% of the unshaped case. Such a shaper cannot reach the original level of the maximum acceleration. This is due to the fact that a given acceleration always causes a certain payload deflection that cannot be undercut, as was explained in Section 5.2. If this payload deflection is higher than the tolerable level, then the acceleration has to be reduced.

One way to get such a deflection-limiting shaper is to reduce all impulses of the UMZV shaper by a certain percentage. This will cause the maximum acceleration of the shaped command, and thus the maximum resulting deflection, to decrease by the same percentage. Figure 73 shows a comparison of a regular UMZV-shaped step command, which reduces the maximum payload deflection to 50%, and a step command that was convolved with an amplitude-reduced UMZV shaper from a boom crane simulation. In this case, the impulse amplitudes and thus the maximum payload deflection were reduced by 20% compared to the regular UMZV shaper.

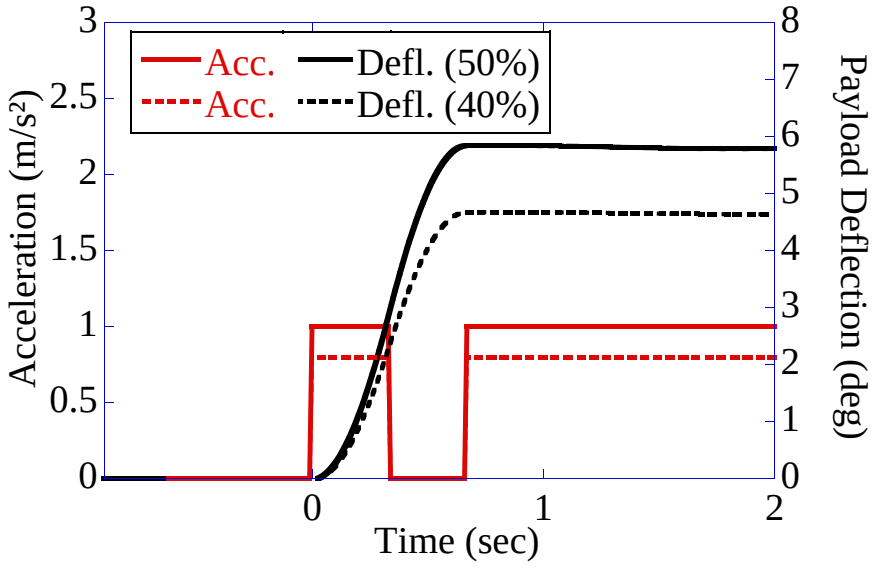

Figure 73: Payload Response for a UMZV-Shaped Step in Acceleration

The new, amplitude-reduced shaper is not a unity-magnitude shaper anymore because its amplitudes are less than one. However, it still has the same duration

as the UMZV shaper. In [28], a way to decrease the duration of deflection-limiting negative shapers was already proposed. This work was limited to step commands in position as baseline commands, but can easily be translated into the acceleration domain. In this adjusted approach, the first two impulses of the negative shaper are 1 and -1, like in the UMZV case. The third impulse is then reduced by the percentage that the maximum deflection should be reduced compared to the UMZV shaper. If the new shaper should limit the maximum deflection to 40% of a step command instead of the 50% of the UMZV shaper, then the third impulse has to be reduced by 20% to a value of 0.8. In order to get zero residual vibration, the impulse times for this shaper have to be adjusted. Figure 74 shows the structure of the new shaper [28]. Table 6 lists the respective impulse amplitudes and times.

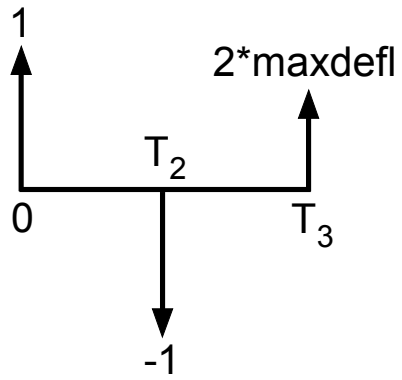

Figure 74: Specified-Deflection-Negative-Amplitude Shaper

Table 6: Impulse Times and Amplitudes for a Specified-Deflection-Negative-Amplitude Shaper

i	1	2	3
T_i	0	$\frac{1}{\omega}(2\arcsin(maxdefl))$	$\frac{1}{\omega}(\arccos(-maxdefl))$
A_i	1	-1	$2 * maxdefl$

The variable $maxdefl$ describes the maximum deflection for a shaped step command as a percentage of the maximum deflection of an unshaped step. The listed amplitudes and times are for an undamped system. Figure 75 shows simulation results comparing the 40% shaper from Figure 73 and the new, faster shaper for the

same percentage of the maximum deflection.

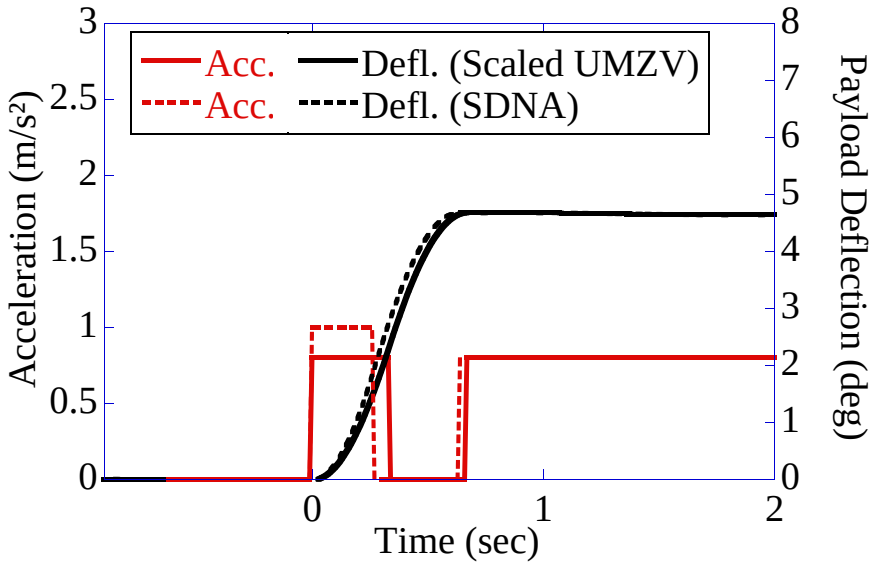

Figure 75: Payload Response for a Specified-Deflection-Negative-Amplitude-Shaped Step in Acceleration

The new shaper provides a faster rise time and limits the maximum deflection to exactly the same angle. The rise time could be decreased even further by allowing the first two impulses to have amplitudes with absolute values greater than 1. However, this should be avoided because it might cause actuator saturation and overcurrenting.

These new shapers, called Specified-Deflection-Negative-Amplitude (SDNA) shapers, were designed for maximum deflection of 40% and 25% of the unshaped case for step inputs in acceleration. These shapers were used to move the benchmark crane setup in a simulation. A worst-case bang-coast-bang command with a maximum acceleration of $1m/s^2$ was assumed for this case and the payload suspension length was $1m$. The boom was luffed at 45° and pointing out to the front of the crane. Figure 76 presents the results for the maximum possible payload for the two SDNA shapers, as well as for the UMZV-shaped, the unshaped, and the static case. Figure 77 shows a zoomed in view of the same plot. As can be seen, the SDNA shapers improved the stability of the crane compared to the UMZV shaper. The shaper durations for the

SDNA shapers are even shorter than the duration of the UMZV shaper. However, the acceleration of the crane after each shaped step is also reduced to achieve the deflection limit. Due to this fact, it takes longer for the crane to reach its maximum velocity. In the present case, the whole motion of the crane took about 5% more time for the 40%-SDNA shaper and about 19% more time for the 25%-SDNA shaper, compared to when the UMZV shaper was used.

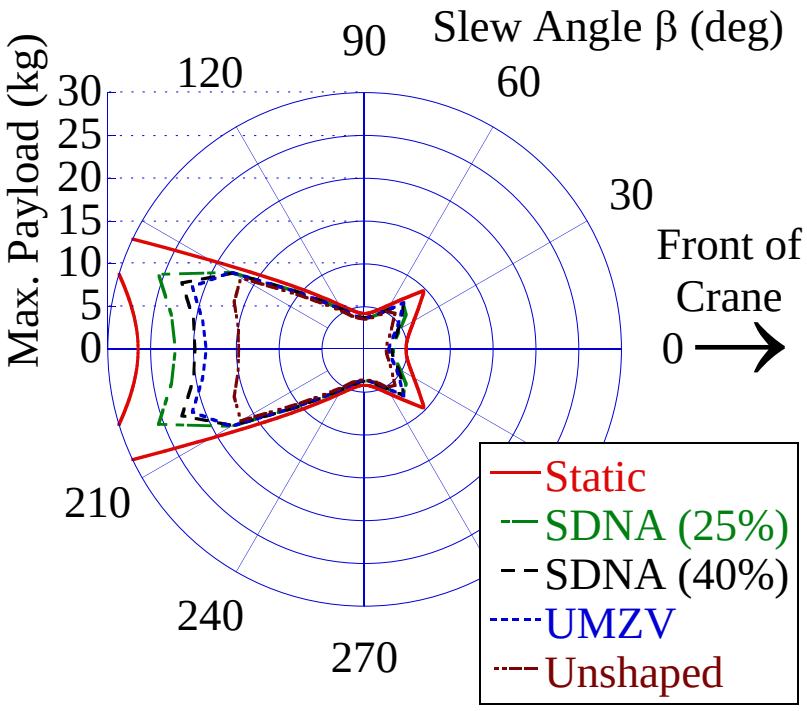

Figure 76: Effects of Different SDNA Shapers on Maximum Payload for a Straight-Line Maneuver

Figure 78 shows a comparison of the maximum payloads for the SDNA shapers to a ZV and ZVD shaper for the same straight-line motion as above. The curves are all very similar except for slew angles around 180°. The 40%-SDNA shaper reaches about the same payload values as the ZV shaper, but the motion of the crane takes 3% less time with the SDNA shaper. The 25%-SDNA shaper compares favorably with the ZVD shaper concerning the maximum payload, but shortens the motion by 7%.

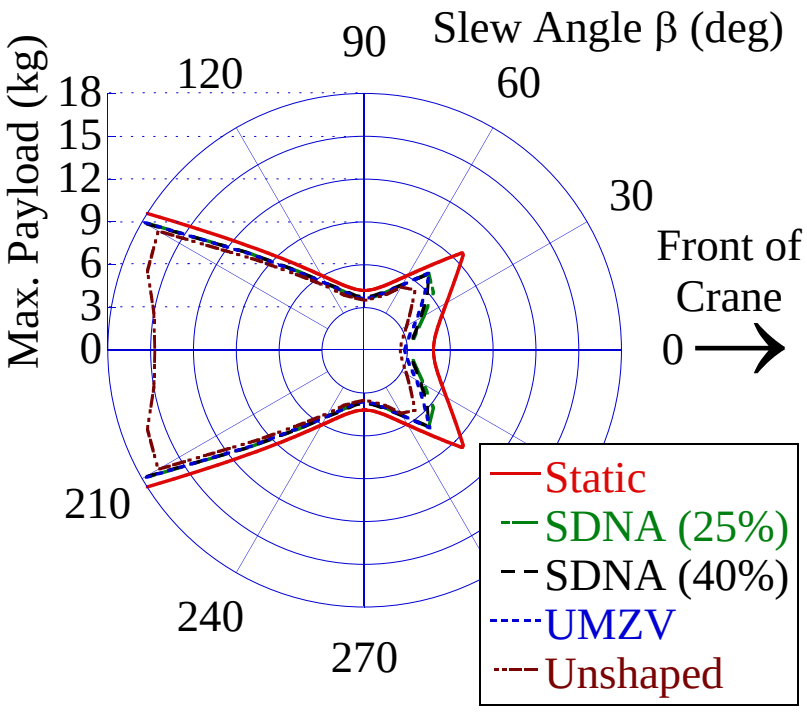

Figure 77: Effects of Different SDNA Shapers on Maximum Payload for a Straight-Line Maneuver, Zoomed View

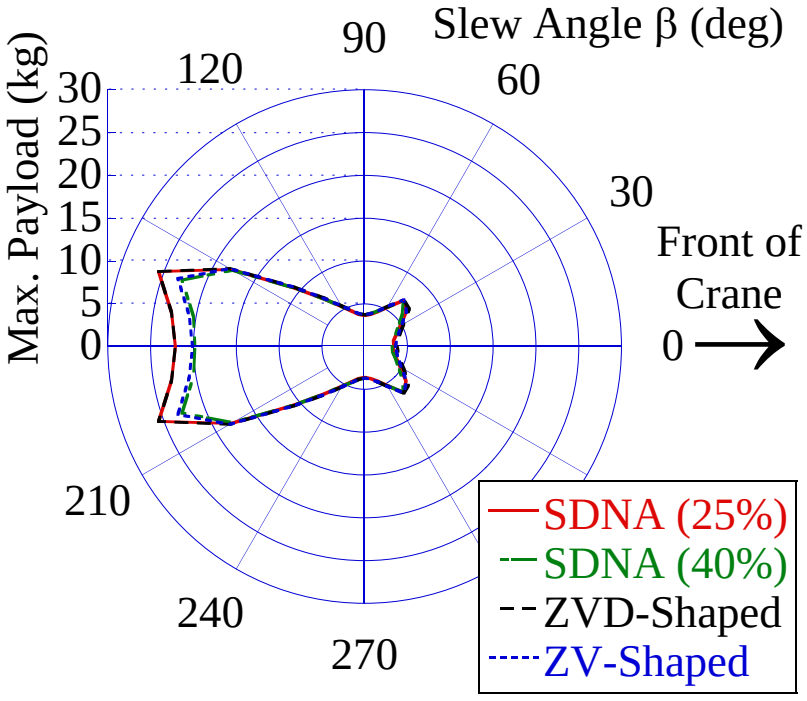

Figure 78: Comparison of the Maximum Payload for SDNA, ZV, and ZVD Shapers for a Straight-Line Maneuver

A possible drawback of the SDNA shapers, as for all negative input shapers, is high-mode excitation [37]. High-frequency oscillations can also have an impact on boom crane stability. It is imaginable that an SDNA shaper for example excites higher modes inherent in the suspension systems of the crane base. Thus, the input shaper could degrade the stability of the crane by inducing oscillations of the crane base. These oscillation could amount to a bouncing motion of the base and thus lead to a loss in stability. However, such detrimental effects could not be observed for the crane simulation used in this thesis.

6.3 Summary

This chapter introduced a graphical design tool called deflection vector diagrams that allows one to keep track of the transient deflection caused by an input shaper when convolved with a step in acceleration. In the second section, Specified-Deflection-Negative-Amplitude (SDNA) shapers were derived. These shapers limit the transient deflection to a certain percentage of the unshaped case while minimizing the rise time of the system.

CHAPTER VII

CONCLUSIONS AND FUTURE WORK

7.1 Conclusions

Allowing boom cranes to move their base while carrying a payload greatly enhances their workspace, and thus their productivity. However, the base motions can cause large amounts of payload swing and thus decrease the stability of the crane. After analyzing the influences of the boom crane configurations for the static case, this thesis presented a semi-dynamic stability analysis that provides insights into boom crane stability for simple driving maneuvers without the need of a complex dynamic simulation of the crane. It was shown for an example setup that this approach leads to a conservative estimation of the maximum payload that a mobile boom crane can carry.

The influences on the payload swing during cornering driving maneuvers are complex. This makes an estimation of crane stability during such maneuvers heavily depending on crane parameters. In this case, a dynamic simulation of the mobile crane like the one developed and presented in Chapter 4 of this thesis provides useful help.

Payload swing and payload deflection has a significant influence on boom crane stability. That is the reason why the control of such a crane should limit these effects. This thesis analyzed the impacts of different input shapers on the maximum payload deflection and the stability of the crane during straight-line driving maneuvers.

This thesis also presented a graphical way to analyze the deflection caused by input shapers designed for the acceleration domain. Additionally, specified-deflection shapers that minimize the system rise time were developed. The influence of these

shapers on crane stability was also analyzed for simple driving maneuvers and compared to the effects of traditional shapers. The comparison showed that the new shapers help to move the crane faster while providing a comparable level of stability.

7.2 Future Work

The insights gained in this thesis build a basis for future work in the area of mobile boom crane stability and open up new directions for further investigations.

One goal for future work is to investigate more complex driving maneuvers and their influence on boom crane stability. A first step in this direction was already taken in this thesis by analyzing the payload swing caused by simple cornering maneuvers. Here, the complex influences of the crane configuration and the structure of the driving maneuver provide numerous possibilities for future analysis.

Another goal in this area is to examine payload dynamics and their influence on crane stability. In the present thesis, only point mass payloads were taken into consideration. Another important area would be payloads exhibiting double pendulum effects or other complex characteristics [38, 33, 15].

Additionally, the model of the crane itself could be extended. For example, many cranes are equipped with counter weights on their rotation bases to improve their stability behavior. The effects and optimization of such a strategy could be investigated in more detail.

A possible way to eliminate dangerous payload oscillation is to use the hoisting motion of the payload to damp out the vibration. The effect of a vertical acceleration of the payload on the payload swing could be examined in more detail [11].

The investigation of input shaping as a method of reducing payload oscillation during a crane's movement is restricted to dynamic simulations of mobile boom cranes in this thesis. For the implementation of input shaping on real mobile cranes, actuator dynamics have to be investigated more closely. For example, nonlinearities like rate

limits and saturation on the crane's motors and drives can impede the effective use of an input shaper to move the crane's base.

Despite control techniques to improve boom crane stability, hardware strategies to improve crane stability are imaginable. A possible way to keep a mobile boom crane from tipping over could be the use of adjustable, training-wheel-like jacks. The implementation and usefulness of such safety equipment could be part of the future work on mobile boom crane stability.

APPENDIX A

MATLAB SOURCE CODES

Source Code A.1: Static and Semi-Dynamic Stability Analysis

```
% maxpayload.m
% Computing the maximum payload for a certain angle configuration of the boom crane
% (luff angle set)
% Author: Andreas Rauch
% ------------------------------------------------------------------------------
function mgraph = maxpayload(phi, theta, l)


%% ------------------------------------------------------------------------------
% Housekeeping
% ------------------------------------------------------------------------------

% Setting the constants
mratio = 8.0/24.9;  % mass ratio describes ratio mb/mc
g = 9.81;           % gravity in m/s^2
lc = 1.10;          % distance between axes in m
lb = 1.70;          % boom length in m
lbcom = 0.8;        % distance from boom attachment point to center of mass of boom
                    % in m
l;                  % cable length in m
phi;                % maximum swing angle in x-direction in radians
theta;              % maximum swing angle in y-direction in radians
la = 0.3;           % distance of tower mount forward of base center in m
la2 = 0.28;         % distance from rotation center to boom attachment point in
                    % forward direction in m
lcom = 0.12;        % center of mass offset from cart center in longitudinal
                    % direction in m
bcom = 0;           % center of mass offset from cart center in lateral direction
                    % in m
bc = 0.70;          % base width / distance between front/back wheels in m
r = 0.14;           % wheel radius in m
h = 0.14;           % height of boom attachment point above com of cart in m
```

```
dec = 1;            % max. deceleration of cart for inertia compensation in m/s^2
loadmax = 5;        % maximum payload in terms of mc
index = 0;          % index variable used to create an array for payload values
index2 = 0;         % index variable used to create an array for payload values

% Specify ranges of angles in degrees
betamin = 0;
betamax = 360;
betastep = 1;

% reserving memory for payload values
mgraph = zeros(((betamax-betamin)/betastep+1), 3*5);

%% ------------------------------------------------------------------------------
% Calculating maximum payload for stable behavior of the crane (using
% absolute swing angles)
% ------------------------------------------------------------------------------

% for loops going over the whole range of the angles
for alpha = 0:15:60
    index2 = index2+1;
    index = 0;
    for be = betamin+1:1:betamax+1
        % create temporary angles in radians
        alphatemp = double(alpha)*pi/180;
        betatemp = double(be-1)*pi/180;
        % increment index variable
        index = index+1;

        % if-statement to compensate for inertia forces in forward
        % direction during deceleration
        if (be >= 90 && be <= 270)

            % if condition to check that payload is not positioned between axes
            if (abs(la+(lb.*cos(alphatemp)+la2).*cos(betatemp))
                    +l.*sin(phi)-lc./2) > 0

                % if condition to check that payload is not positioned between
                % tires of one axis
                if (abs((lb.*cos(alphatemp)+la2).*sin(betatemp))+l.*sin(theta)
                -bc./2) > 0
```

```
74
75                  % if condition to detect the smallest value for maximum
76                  % possible payload
77                  if (((lc./2-lcom*sign(la+(lbcom.*cos(alphatemp)+la2)
78                  .*cos(betatemp)))-mratio.*(abs(la+(lbcom.*cos(alphatemp)
79                  +la2).*cos(betatemp))-lc./2))./(abs(la+
80                  (lb.*cos(alphatemp)+la2).*cos(betatemp))+l.*sin(phi)
81                  -lc./2) <= ((bc./2-bcom*sign((lbcom.*cos(alphatemp)+la2)
82                  .*sin(betatemp)))-mratio.*(abs((lbcom.*cos(alphatemp)
83                  +la2).*sin(betatemp))-bc./2))./(abs((lb.*cos(alphatemp)
84                  +la2).*sin(betatemp))+l.*sin(theta)-bc./2))
85
86                      mp = ((lc./2-lcom*sign(la+(lbcom.*cos(alphatemp)+la2)
87                      .*cos(betatemp)))-mratio.*(abs(la+(lbcom.*cos(alphatemp)
88                      +la2).*cos(betatemp))-lc./2))./(abs(la+(lb
89                      .*cos(alphatemp)+la2).*cos(betatemp))+l.*sin(phi)-lc./2);
90                  else
91                      mp = ((bc./2-bcom*sign((lbcom.*cos(alphatemp)+la2)
92                      .*sin(betatemp)))-mratio.*(abs((lbcom.*cos(alphatemp)
93                      +la2).*sin(betatemp))-bc./2))./(abs((lb.*cos(alphatemp)
94                      +la2).*sin(betatemp))+l.*sin(theta)-bc./2);
95                  end
96
97              else
98                  mp = ((lc./2-lcom*sign(la+(lbcom.*cos(alphatemp)+la2)
99                  .*cos(betatemp)))-mratio.*(abs(la+(lbcom.*cos(alphatemp)+la2)
100                 .*cos(betatemp))-lc./2))./(abs(la+(lb.*cos(alphatemp)+la2)
101                 .*cos(betatemp))+l.*sin(phi)-lc./2);
102             end
103
104         else
105
106             % if condition to check that payload is not positioned between
107             % tires of one axis
108             if (abs((lb.*cos(alphatemp)+la2).*sin(betatemp))+l.*sin(theta)
109             -bc./2) > 0
110
111                 mp = ((bc./2-bcom*sign((lbcom.*cos(alphatemp)+la2)
112                 .*sin(betatemp)))-mratio.*(abs((lbcom.*cos(alphatemp)+la2)
113                 .*sin(betatemp))-bc./2))./(abs((lb.*cos(alphatemp)+la2)
114                 .*sin(betatemp))+l.*sin(theta)-bc./2);
```

```
115                 else
116                     % if payload is positioned above the base, loadmax is set
117                     % as maximum possible payload
118                     mp = loadmax;
119                 end
120
121             end
122
123         else
124
125             % if condition to check that payload is not positioned between axes
126             if (abs(la+(lb.*cos(alphatemp)+la2).*cos(betatemp))+l.*sin(phi)
127             -lc./2) > 0
128
129                 % if condition to check that payload is not positioned between
130                 % tires of one axis
131                 if (abs((lb.*cos(alphatemp)+la2).*sin(betatemp))+l.*sin(theta)
132                 -bc./2) > 0
133
134                     % if condition to detect the smallest value for maximum
135                     % possible payload
136                     if (((lc./2-lcom*sign(la+(lbcom.*cos(alphatemp)+la2)
137                     .*cos(betatemp)))-mratio.*(abs(la+(lbcom.*cos(alphatemp)+la2)
138                     .*cos(betatemp))-lc./2)-(2*r+h+lbcom*sin(alphatemp))
139                     *mratio*dec/g-2*r*dec/g)./(abs(la+(lb.*cos(alphatemp)+la2)
140                     .*cos(betatemp))+l.*sin(phi)-lc./2) <= ((bc./2-bcom*sign((lbcom
141                     .*cos(alphatemp)+la2).*sin(betatemp)))-mratio.*(abs((lbcom
142                     .*cos(alphatemp)+la2).*sin(betatemp))-bc./2))./(abs((lb
143                     .*cos(alphatemp)+la2).*sin(betatemp))+l.*sin(theta)-bc./2))
144
145                         mp = ((lc./2-lcom*sign(la+(lbcom.*cos(alphatemp)+la2)
146                         .*cos(betatemp)))-mratio.*(abs(la+(lbcom.*cos(alphatemp)
147                         +la2).*cos(betatemp))-lc./2)-(2*r+h+lbcom*sin(alphatemp))
148                         *mratio*dec/g-2*r*dec/g)./(abs(la+(lb.*cos(alphatemp)+la2)
149                         .*cos(betatemp))+l.*sin(phi)-lc./2);
150                     else
151                         mp = ((bc./2-bcom*sign((lbcom.*cos(alphatemp)+la2)
152                         .*sin(betatemp)))-mratio.*(abs((lbcom.*cos(alphatemp)
153                         +la2).*sin(betatemp))-bc./2))./(abs((lb.*cos(alphatemp)
154                         +la2).*sin(betatemp))+l.*sin(theta)-bc./2);
155                     end
```

```
156
157                 else
158                     mp = ((lc./2-lcom*sign(la+(lbcom.*cos(alphatemp)+la2)
159                     .*cos(betatemp)))-mratio.*(abs(la+(lbcom.*cos(alphatemp)+la2)
160                     .*cos(betatemp))-lc./2)-(2*r+h+lbcom*sin(alphatemp))
161                     *mratio*dec/g-2*r*dec/g)./(abs(la+(lb.*cos(alphatemp)+la2)
162                     .*cos(betatemp))+l.*sin(phi)-lc./2);
163                 end
164
165             else
166
167                 % if condition to check that payload is not positioned between
168                 % tires of one axis
169                 if (abs((lb.*cos(alphatemp)+la2).*sin(betatemp))+l.*sin(theta)
170                  -bc./2) > 0
171                     mp = ((bc./2-bcom*sign((lbcom.*cos(alphatemp)+la2)
172                     .*sin(betatemp)))-mratio.*(abs((lbcom.*cos(alphatemp)+la2)
173                     .*sin(betatemp))-bc./2))./(abs((lb.*cos(alphatemp)+la2)
174                     .*sin(betatemp))+l.*sin(theta)-bc./2);
175                 else
176                     % if payload is positioned above the base, loadmax is set
177                     % as maximum possible payload
178                     mp = loadmax;
179                 end
180
181             end
182
183
184         end
185
186         % values for maximum possible payload are limited
187         if mp >= loadmax;
188             mp = loadmax;
189         end
190
191         % write in arrays
192         mgraph(index, 3+(index2-1)*3) = mp;
193         mgraph(index, 1+(index2-1)*3) = alphatemp*180/pi;
194         mgraph(index, 2+(index2-1)*3) = betatemp*180/pi;
195
196     end
```

```
197 end
198
199
200 %% ------------------------------------------------------------------------------
201 % Save mgraph in ASCII file
202 % ------------------------------------------------------------------------------
203
204 save -ascii maxpayload.txt mgraph
```

APPENDIX B

AUTOLEV SOURCE CODES

Source Code B.1: Simulation of a Mobile Boom Crane

```
% mobileboom.al
% Generates equations of motion for MATLAB simulations of a Mobile Boom Crane
% Created by Andreas Rauch based on an existing model developed by Joshua
% Vaughan and Jon Danielson

% Default settings
Autoz off                                % switching off intermediate variables

% Newtonians, bodies, frames, points, particles
Newtonian N                              % Newtonian reference system
Bodies C, B, D                           % bodies with mass and inertia for cart,
                                         % boom, cable
Frames Bbeta, Dalpha, Dbeta, Dphi        % intermediate frames for boom/payload
Frames A, E                              % intermediate frames for cart
Points BC, CC, FA                        % point for boom attachment, cart center
                                         % and front axle center point
Points w1, w2, w3, w4                    % wheel contact points
Points w1N, w2N, w3N, w4N                % wheel contact points on ground
Particle payload                         % payload as a point mass

% Variables, constants
Motionvariables' u1', u2', u3'           % motion variables for cart tipping/sag
Motionvariables' phi'', theta''           % motion variables for payload swing
Variables x'', y'', q1', q2', q3'        % variables for cart motion, tipping/sag
Variables u4', u5', q4', q5'             % variables for boom motion
Variables Lw1', Lw2', Lw3', Lw4'         % variables for wheel deflection
Variables psi'', gamma''                 % variables for cart rotation/steering
Variables v'', xfront'', yfront''        % cart velocity and front axle motion
Variables F1, F2, F3, F4                 % variables for wheel normal forces
Variables xtip', ytip', xtipacc, ytipacc % variables for boom tip motion
Constants la, la2, bc, r, h, g, lb       % constants for crane properties, gravity
Constants l, lc, damp, stiff             % constants for crane properties
```

```
33 Constants mb, mp, mc, lcom, bcom, lbcom      % constants for crane properties
34 Specified specx'', specy'', specgamma'       % variables to specify cart motion
35 Specified specv'                             % variables to specify cart motion
36 Specified specalpha'', specbeta''            % variables to specify boom motion
37
38 % Masses, inertias
39 Mass C = mc, B = mb, payload = mp, D = 0            % mass of cart, boom, payload,
40                                                    % cable
41 Inertia C, mc/12*bc^2, mc/12*lc^2, mc/12*(lc^2+bc^2)% inertia of cart
42 Inertia B, 0, IB = mb/12*lb^2, IB                   % inertia of boom
43 Inertia D, 0,0,0                                   % inertia of cable
44
45 % Auxiliary variables
46 q1' = u1                                      % forward/backward pitch angle / angular
47                                               % velocity
48 q2' = u2                                      % lateral tilt angle / angular velocity
49 q3' = u3                                      % cart sag / vertical velocity
50 q4' = u4                                      % luff angle / angular velocity
51 q5' = u5                                      % slew angle / angular velocity
52 u4' = specalpha''                             % specifying luff acceleration
53 u5' = specbeta''                              % specifying slew acceleration
54 v' = specv'                                   % linear acceleration of front axle
55 gamma' = specgamma'                           % angular velocity of steering
56 xfront' = v*cos(psi+gamma)                    % equation of motion for x coordinate of
57                                               % front axle center
58 yfront' = v*sin(psi+gamma)                    % equation of motion for y coordinate of
59                                               % front axle center
60 xfront'' = Dt(xfront')                        % acceleration of front axle center point
61                                               % in x-direction
62 yfront'' = Dt(yfront')                        % acceleration of front axle center point
63                                               % in-y direction
64 psi' = v/lc*sin(gamma)                        % equation of motion for angular velocity
65                                               % of cart about vertical axis
66 psi'' = Dt(psi')                             % angular acceleration of the cart about
67                                               % vertical axis
68
69 % Position vectors
70 P_NO_FA> = xfront*N1> +yfront*N2>             % position of front axle center point
71                                               % in N
72 P_AO_FA> = lc/2*A1>                           % position of front axle in relation to
73                                               % AO
```

```
74 P_AO_CC> = (2*r+q3)*C3>                          % from AO to cart center
75 P_CC_CO> = lcom*C1>+bcom*C2>                     % from cart center to cart center of mass
76 P_CC_w1> = -lc/2*C1> + bc/2*C2> - 2*r*C3>       % from cart center to wheel contact
77                                                  % point 1
78 P_CC_w2> = lc/2*C1> + bc/2*C2> - 2*r*C3>        % from cart center to wheel contact
79                                                  % point 2
80 P_CC_w3> = lc/2*C1> - bc/2*C2> - 2*r*C3>        % from cart center to wheel contact
81                                                  % point 3
82 P_CC_w4> = -lc/2*C1> - bc/2*C2> - 2*r*C3>       % from cart center to wheel contact
83                                                  % point 4
84 P_CC_BbetaO> = la*C1>                           % from cart center to tower rotation
85                                                  % center
86 P_BbetaO_BC> = la2*Bbeta1> + h*Bbeta3>          % from rotation center to boom attachment
87                                                  % point
88 P_BC_DO> = lb*B1>                               % from boom attachment point to boom end
89 P_BC_BO> = lbcom*B1>                            % from boom attachment point to boom
90                                                  % center of mass
91 P_DO_payload> = -l*D3>                          % from boom end to payload
92 P_NO_w1N> = xfront*N1>+yfront*N2>-lc*A1>+bc/2*A2>   % position of wheel 1 contact
93                                                      % point on ground in N
94 P_NO_w2N> = xfront*N1>+yfront*N2>+bc/2*A2>          % position of wheel 2 contact
95                                                      % point on ground in N
96 P_NO_w3N> = xfront*N1>+yfront*N2>-bc/2*A2>          % position of wheel 3 contact
97                                                      % point on ground in N
98 P_NO_w4N> = xfront*N1>+yfront*N2>-lc*A1>-bc/2*A2>   % position of wheel 4 contact
99                                                      % point on ground in N
100
101 % Angular velocities
102 W_A_N> = psi'*N3>                              % of intermediate frame A in N
103 W_E_N> = W_A_N> + u1*C2>                       % of intermediate frame E in N
104 W_C_N> = W_E_N> + u2*E1>                       % of cart in N
105 W_B_N> = W_C_N> + u5*Bbeta3> - u4*B2>          % of boom in N
106 W_D_N> = W_B_N>-phi'*Dphi2> + theta'*D1>       % of cable in N
107
108 % Rotation matrices
109 Simprot(N, A, 3, psi)                          % rotation of cart
110 Simprot(A, E, 2, q1)                           % forward/backward pitching of cart
111 Simprot(E, C, 1, q2)                           % lateral tilting of cart
112 Simprot(C,Bbeta,3,q5)                         % rotation of boom
113 Simprot(Bbeta,B,2,-q4)                        % luffing of boom
114 Simprot(B,Dalpha,2,q4)                        % intermediate frame in order to get
```

```
                                        % swing angles in a vertical reference
                                        % frame, not perpendicular to boom
Simprot(Dalpha,Dbeta,3,-q5)             % intermediate frame in order to get
                                        % swing angles in a reference frame
                                        % with the same direction as the cart
Simprot(Dbeta,Dphi,2,-phi)              % payload swing to the front/back
Simprot(Dphi,D,1,theta)                 % lateral payload swing

% Velocities
V_AO_N> = Dt(P_NO_AO>, N)               % velocity of AO in N
V_CO_N> = Dt(P_NO_CO>, N)               % velocity of cart center of mass in N
V_CC_N> = Dt(P_NO_CC>, N)               % velocity of cart center in N
V_DO_N> = Dt(P_NO_DO>,N)                % velocity of boom tip in N
V_payload_N> = Dt(P_NO_payload>,N)      % velocity of payload in N
V_BC_C> = 0>                            % velocity of boom attachment relative
                                        % to cart
V2pts(N, C, CO, BC)                     % velocity of BC in N
V2pts(N, B, BC, BO)                     % velocity of boom center in cart
V2pts(N, C, CO, w1)                     % velocity of wheel 1 contact point in N
V2pts(N, C, CO, w2)                     % velocity of wheel 2 contact point in N
V2pts(N, C, CO, w3)                     % velocity of wheel 3 contact point in N
V2pts(N, C, CO, w4)                     % velocity of wheel 4 contact point in N
V2pts(N, A, AO, w1N)                    % velocity of wheel 1 contact point on
                                        % ground in N
V2pts(N, A, AO, w2N)                    % velocity of wheel 2 contact point on
                                        % ground in N
V2pts(N, A, AO, w3N)                    % velocity of wheel 3 contact point on
                                        % ground in N
V2pts(N, A, AO, w4N)                    % velocity of wheel 4 contact point on
                                        % ground in N

% Accelerations
A_CO_N> = Dt(V_CO_N>, N)                % acceleration of cart center of mass
                                        % in N
A_CC_N> = Dt(V_CC_N>, N)                % acceleration of cart center in N
A2pts(N,B,BC,BO)                        % acceleration of boom center in N
A2pts(N,B,BO,DO)                        % acceleration of boom tip in N
A_payload_N> = Dt(V_payload_N>, N)      % acceleration of payload in N

% Angular accelerations
ALF_A_N> = Dt(W_A_N>, N)                % of intermediate frame A in N
```

```
156 ALF_E_N> = Dt(W_E_N>, N)                    % of intermediate frame E in N
157 ALF_C_N> = Dt(W_C_N>, N)                    % of cart in N
158 ALF_B_N> = Dt(W_B_N>, N)                    % of boom in N
159 ALF_D_N> =  Dt(W_D_N>, N)                  % of cable in N
160
161 % Forces
162 Gravity(-g*N3>)                            % gravity force
163 Lw1 = Dot(P_NO_w1>, N3>)                   % wheel 1 deflection
164 Lw2 = Dot(P_NO_w2>, N3>)                   % wheel 2 deflection
165 Lw3 = Dot(P_NO_w3>, N3>)                   % wheel 3 deflection
166 Lw4 = Dot(P_NO_w4>, N3>)                   % wheel 4 deflection
167 Lw1' = Dot(V_w1_N>, N3>)                   % wheel 1 deflection rate
168 Lw2' = Dot(V_w2_N>, N3>)                   % wheel 2 deflection rate
169 Lw3' = Dot(V_w3_N>, N3>)                   % wheel 3 deflection rate
170 Lw4' = Dot(V_w4_N>, N3>)                   % wheel 4 deflection rate
171 F1 = -stiff*Lw1-damp*Lw1'                 % normal force at wheel 1 (has to be
172                                            % changed in MATLAB to be compressive
173                                            % only)
174 F2 = -stiff*Lw2-damp*Lw2'                 % normal force at wheel 2 (has to be
175                                            % changed in MATLAB to be compressive
176                                            % only)
177 F3 = -stiff*Lw3-damp*Lw3'                 % normal force at wheel 3 (has to be
178                                            % changed in MATLAB to be compressive
179                                            % only)
180 F4 = -stiff*Lw4-damp*Lw4'                 % normal force at wheel 4 (has to be
181                                            % changed in MATLAB to be compressive
182                                            % only)
183 Force(w1N/w1, F1*N3>)                      % normal force at wheel 1
184 Force(w2N/w2, F2*N3>)                      % normal force at wheel 2
185 Force(w3N/w3, F3*N3>)                      % normal force at wheel 3
186 Force(w4N/w4, F4*N3>)                      % normal force at wheel 4
187
188 % Equations of motion
189 Zero = Fr() + FrStar()
190 Kane()
191
192 % Motion of cart and boom tip
193 x'' = Dot(A_CC_N>, N1>)                    % cart center motion in N1>/x-direction
194 y'' = Dot(A_CC_N>, N2>)                    % cart center motion in N2>/y-direction
195 xtip' = Dot(V_DO_N>, N1>)                  % boom tip motion in N1>/x-direction
196 ytip' = Dot(V_DO_N>, N2>)                  % boom tip motion in N2>/y-direction
```

```
xtipacc = Dot(A_DO_N>, N1>)                    % boom tip motion in N1>/x-direction
ytipacc = Dot(A_DO_N>, N2>)                    % boom tip motion in N2>/y-direction

%Generate MATLAB code for simulation
UnitSystem kg, meter, sec
Input la= 0.3 m, la2 = 0.28 m, bc = 0.70 m, r = 0.14 m, mc = 24.9 kg
Input tFinal = 20, mp = 2 kg, lc = 1.1 m, l = 1 m, stiff = 250000 N/m, lcom = 0.12 m
Input g = 9.81 m/sec^2, mb = 8.0 kg, lb = 1.7 m, h = 0.14, damp = 1000 N*sec/m
Input bcom = 0 m, lbcom = 0.8 m
Output T sec, xfront m, xfront' m/sec, xfront'' m/sec^2, x m, x' m/sec, x'' m/sec^2,
xtip m, xtip' m/sec, xtipacc m/sec^2, yfront m, yfront' m/sec, yfront'' m/sec^2, y m,
y' m/sec, y'' m/sec^2, ytip m, ytip' m/sec, ytipacc m/sec^2, phi degree,
theta degree, F1 N, F2 N, F3 N, F4 N, q1 deg, q2 deg, q3 m, Lw1 m, Lw2 m, Lw3 m,
Lw4 m, q4 deg, u4 deg/sec, u4' deg/sec^2, q5 deg, u5 deg/sec, u5' deg/sec^2
CODE Dynamics() mobileboom.m
```

REFERENCES

[1] Abdel-Rahman, E. and Nayfeh, A., "Pendulation reduction in boom cranes using cable length manipulation," *Nonlinear Dynamics*, vol. 27, no. 3, pp. 255–269, 2002.

[2] Abdel-Rahman, E., Nayfeh, A., and Masoud, Z., "Dynamics and control of cranes: A review," *Journal of Vibration and Control*, vol. 9, no. 7, pp. 863–908, 2003.

[3] Abo-Shanab, R. and Sepehri, N., "Tip-over responses of hydraulic mobile cranes," *Transactions of the Canadian Society for Mechanical Engineering*, vol. 30, pp. 391–412, 2006.

[4] Acarman, T. and Ozguner, U., "Rollover prevention for heavy trucks using frequency shaped sliding mode control," *Vehicle System Dynamics*, vol. 44, pp. 737–762, 2006.

[5] Arnold, E., Sawodny, O., Hilderbrandt, A., and Schneider, K., "Anti-sway system for boom cranes based on an optimal control approach," in *American Control Conference*, vol. 4, (Denver, CO), pp. 3166–71, 2003.

[6] Banerjee, A., Singhose, W., and Blackburn, D., "Orbit boosting of an electrodynamic tethered satellite with input-shaped current," in *Proceedings of the AAS/AIAA Astrodynamics Conference*, vol. 123, (South Lake Tahoe, CA, United States), pp. 1053–1060, 2005.

[7] Banerjee, A. K. and Singhose, W. E., "Command shaping in tracking control of a two-link flexible robot," *Journal of Guidance, Control, and Dynamics*, vol. 21, pp. 1012–1015, 1998.

[8] Bertoluzzo, M., Buja, G., Cuogo, L., Sulligoi, G., and Zagatti, E., "Anti-roll control for by-wire lift truck," in *EUROCON*, (Belgrade, Serbia & Montenegro), 2005.

[9] Bouton, N., Lenain, R., Thuilot, B., and Fauroux, J.-C., "A rollover indicator based on the prediction of the load transfer in presence of sliding: application to an all terrain vehicle," in *IEEE International Conference on Robotics and Automation*, (Rome, Italy), 2007.

[10] CDC, "http://www.cdc.gov/elcosh/docs/d0800/d000804/1.jpg," Accessed: 11:15am, July 12, 2008.

[11] Danielson, J., "Mobile boom cranes and advanced input shaping control," Master's thesis, Georgia Institute of Technology, 2008.

[12] Forest, C., Frakes, D., and Singhose, W., "Input-shaped control of gantry cranes: Simulation and curriculum development," in *Proceedings of the ASME Design Engineering Technical Conference*, vol. 6, (Sep 9-12 2001, Pittsburgh, PA, United States), pp. 1877–1884, 2001.

[13] Khalid, A., Huey, J., Singhose, W., Lawrence, J., and Frakes, D., "Human operator performance testing using an input-shaped bridge crane," *Journal of Dynamic Systems, Measurement and Control*, vol. 128, pp. 835–841, 2006.

[14] Kiliçaslan, S., Balkan, T., and Ider, S., "Tipping loads of mobile cranes with flexible booms," *Journal of Sound and Vibration*, vol. 223, no. 4, pp. 645–657, 1999.

[15] Kim, D. and Singhose, W., "Human operator learning on double-pendulum bridge cranes," in *Proceedings of the ASME International Mechanical Engineering Congress and Exposition*, vol. 9, (Seattle, WA, United States), pp. 1959–1965, 2007.

[16] Kogan, J., *Lifting and conveying machinery.* Ames, Iowa, USA: Iowa State University Press, 1985.

[17] Kojima, H. and Singhose, W., "Adaptive deflection-limiting control for slewing flexible space structures," *Journal of Guidance, Control, and Dynamics*, vol. 30, pp. 61–7, 2007.

[18] Lee, Y. and Yi, S.-J., "Rollover prevention for sport utility vehicle using fuzzy logic controller," in *ICMIT 2005: Control Systems and Robotics, Proc. of SPIE*, vol. 6042, 2005.

[19] Lewis, D., Parker, G., Driessen, B., and Robinett, R., "Command shaping control of an operator-in-the-loop boom crane," in *American Control Conference*, vol. 5, (Philadelphia, Pennsylvania), pp. 2643–7, 1998.

[20] Lim, T. H., Kim, Y. S., Choi, J. H., Lee, H. S., and Yang, S. Y., "Development of tipping-over rate computation system for hydraulic excavator having crane function," in *Proceedings: KORUS 2004, 8th Korea-Russia International Symposium on Science and Technology*, pp. 76–79, 2005.

[21] Love, L., Magee, D., and Book, W., "A comparison of joint control algorithms for teleoperated pick and place tasks using a flexible manipulator," in *Proceedings of IEEE International Conference on Systems, Man and Cybernetics*, vol. 2, (San Antonio, TX, USA), pp. 1257–62, 1994.

[22] Magee, D. P. and Book, W. J., "Eliminating multiple modes of vibration in a flexible manipulator," in *Proceedings of IEEE International Conference on Robotics and Automation*, vol. 2, (Atlanta, GA, USA), pp. 474–479, 1993.

[23] Magee, D. and Book, W., "Implementing modified command filtering to eliminate multiple modes of vibration," in *Proceedings of American Control Conference - ACC '93*, vol. 3, (San Francisco, CA, USA), pp. 2700–4, 1993.

[24] Malcher, D., Eskandarian, A., and Delaigue, P., "Dynamics models for vehicle roll motion in prerollover manoeuvres," *Proceedings of the Institution of Mechanical Engineers, Part K: Journal of Multi-body Dynamics*, vol. 221, pp. 291–301, 2007.

[25] Manitowo, "http://www.manitowoccranegroup.com/mcg_images/mcg_mcg/cn/news/21000812yansan-hr.jpg," Accessed: 11:00am, July 12, 2008.

[26] P+H, C. S. P., "http://www.crane-spare-parts.com/images/p+h-crane-spare-parts.jpg," Accessed: 10:30am, July 12, 2008.

[27] Robertson, M. J. and Singhose, W. E., "Deflection vector diagrams for a mass under pd control," in *Proceedings of the American Control Conference*, vol. 4, (Denver, CO, United States), pp. 2815–2820, 2003.

[28] Robertson, M. J. and Singhose, W. E., "Closed-form deflection-limiting commands," in *Proceedings of the American Control Conference*, vol. 3, (Portland, OR, United States), pp. 2104–2109, 2005.

[29] Robertson, M. J. and Singhose, W. E., "Robust analytic deflection-limiting commands," in *Proceedings of the American Control Conference*, vol. 2006, (Minneapolis, MN, United States), pp. 363–368, 2006.

[30] Robertson, M. J. and Singhose, W. E., "Specified-deflection command shapers for second-order position input systems," *Journal of Dynamic Systems, Measurement and Control*, vol. 129, pp. 856–859, 2007.

[31] Robertson, M. J., *Command generation for tethered satellite systems*. PhD thesis, Georgia Institue of Technology, 2005.

[32] Singer, N. and Seering, W., "Preshaping command inputs to reduce system vibration," *Journal of Dynamic Systems, Measurement and Control, Transactions ASME*, vol. 112, pp. 76–82, 1990.

[33] Singhose, W., Kim, D., and Kenison, M., "Input shaping control of double-pendulum bridge crane oscillations," *Journal of Dynamic Systems, Measurement and Control*, vol. 130, pp. 1–7, 2008.

[34] Singhose, W., Seering, W., and Singer, N., "Residual vibration reduction using vector diagrams to generate shaped inputs," *Journal of Mechanical Design*, vol. 116, pp. 654–659, 1994.

[35] Singhose, W. E., Porter, L. J., Tuttle, T. D., and Singer, N. C., "Vibration reduction using multi-hump input shapers," *Journal of Dynamic Systems, Measurement, and Control*, vol. 119, pp. 320–326, 1997.

[36] Singhose, W. E., Seering, W. P., and Singer, N. C., "Shaping inputs to reduce vibration: A vector diagram approach," in *Proceedings of the 1990 IEEE International Conference on Robotics and Automation*, (Cincinnati, OH, USA), pp. 922–927, 1990.

[37] Singhose, W., Seering, W., and Singer, N., "Time-optimal negative input shapers," *Journal of Dynamic Systems, Measurement and Control*, vol. 119, pp. 198–205, 1997.

[38] Singhose, W. and Kim, D., "Manipulation with tower cranes exhibiting double-pendulum oscillations," in *Proceedings of the IEEE International Conference on Robotics and Automation*, (Rome, Italy), pp. 4550–4555, 2007.

[39] Smith, O., "Posicast control of damped oscillatory systems," in *Proceedings of the Institute of Radio Engineers*, vol. 45, pp. 1249–1255, 1957.

[40] Sorensen, K. L., Singhose, W., and Dickerson, S., "A controller enabling precise positioning and sway reduction in bridge and gantry cranes," *Control Engineering Practice*, vol. 15, pp. 825–837, 2007.

[41] Towarek, Z., "Dynamic stability of a crane standing on soil during the rotation of the boom," *International Journal of Mechanical Sciences*, vol. 40, no. 6, pp. 557–574, 1998.

[42] Tullacalder, "http://www.tullacalder.com.au/images/gallery/crane.jpg," Accessed: 12:15pm, February 26, 2008.

[43] Tuttle, T. D. and Seering, W. P., "Creating time-optimal commands with practical constraints," *Journal of Guidance, Control, and Dynamics*, vol. 22, pp. 241–250, 1999.

[44] Vaughan, J., Singhose, W., Debenest, P., Fukushima, E., and Hirose, S., "Initial experiments on the control of a mobile tower crane," in *Proceedings of the ASME International Mechanical Engineering Congress and Exposition*, (Seattle, WA, United States), pp. 1861–1866, 2007.

[45] Vaughan, J., Yano, A., and Singhose, W., "Comparison of robust input shapers," *Journal of Sound and Vibration*, vol. 315, pp. 797–815, 2008.